eISSN 2450-8071
ISSN 0867-888X
Index 35726 X

INSTITUTE
OF FUNDAMENTAL
TECHNOLOGICAL
RESEARCH
POLISH
ACADEMY
OF SCIENCES

in cooperation with:

UNIVERSITÉ
DE LORRAINE

POZNAN
UNIVERSITY
OF TECHNOLOGY

ENGINEERING TRANSACTIONS

ROZPRAWY INŻYNIERSKIE – TRAITE d'INGENIERIE

QUARTERLY
VOLUME 74 ISSUE 1

WARSAW – METZ – POZNAN 2026

INSTITUTE
OF FUNDAMENTAL
TECHNOLOGICAL
RESEARCH
POLISH
ACADEMY
OF SCIENCES

UNIVERSITÉ
DE LORRAINE

POZNAN
UNIVERSITY
OF TECHNOLOGY

ENGINEERING TRANSACTIONS

ROZPRAWY INŻYNIERSKIE – TRAITE d'INGENIERIE

QUARTERLY
VOLUME 74
ISSUE 1

WARSAW – METZ – POZNAN 2026

ENGINEERING TRANSACTIONS

Founded 1952
Appears since 1953

Aims and Scope

ENGINEERING TRANSACTIONS promotes research and practise in engineering science and provides a forum for interdisciplinary publications combining **mechanics** with material science, mechatronics, biomechanics, and biotechnologies, environmental science, photonics, information technologies, and other engineering applications. The journal publishes original papers covering a broad area of research activities including experimental and hybrid techniques as well as analytical and numerical approaches. Engineering Transactions is a quarterly issued journal for researchers in academic and industrial communities.

Editorial Office
Institute of Fundamental Technological Research, Polish Academy of Sciences
Pawińskiego 5B, 02-106 Warsaw, Poland
e-mail: engtrans@ippt.pan.pl https://et.ippt.pan.pl/

Abstracted/indexed in: Web of Science (Clarivate) JCR Core Collection, EBSCO, Elsevier – Scopus, DOAJ, BazTech, Biblioteka Nauki, ICI Journal Master List.

Impact stats: Journal Impact Factor (IF) 2024: 1.0, SCImago Journal Rank (SJR) 2024: 0.210, CiteScore 2024 (Scopus): 1.4, SNIP 2024: 0.551.

Typesetting in LaTeX: Jezierska Katarzyna Publisher's sheets 11.5 Printed sheets 9.25

Engineering Transactions, **74**(1): 3–17, 2026, https://doi.org/10.24423/engtrans.2026.3488
Institute of Fundamental Technological Research Polish Academy of Sciences (IPPT PAN)
Université de Lorraine • Poznan University of Technology

Research Paper

Changes in the Damping Ratio and Energy Transfer Ratio Due to Damage in a Composite Beam

Małgorzata Jarosińska

Faculty of Civil and Environmental Engineering,
West Pomeranian University of Technology in Szczecin
Szczecin, Poland

e-mail: jarosinska@zut.edu.pl

This paper investigates changes in the modal parameters of a composite beam resulting from damage introduced to the bottom flange of a steel I-beam. Variations in the modal damping ratio and energy transfer ratio (ETR) are analysed. The results of experimental tests and numerical analyses are presented. The beam was modelled using the rigid finite elements (RFEs) method. The introduced damage caused small changes in the damping ratio. In contrast, the ETR was found to be more sensitive to damage than the damping ratio in the experimental results, exhibiting variations on the order of several tens of percent. In the numerical simulation results, changes in the ETR were smaller, reaching a few percent.

Keywords: steel-concrete composite beam, damage detection, energy transfer ratio (ETR).

1. Introduction

The use of composite structures is a solution increasingly chosen by engineers. The most common form of composite structure used in construction is the steel-concrete system. Steel-concrete composite structures use the compressive strength of concrete and the tensile strength of steel, resulting in an efficient and lightweight structure. Interaction between concrete and steel is made possible by a shear connector welded to the steel beam. Thus, with suitable connection between the concrete slab and the steel beam, slip between the two materials is eliminated. This increases stiffness and strength of such a composite element. In bridge structures, composite elements are readily used due to their favourable functional properties and economic considerations. In the literature, one can find papers in which researchers present solutions for innovative composite structures such as hybrid girders [1–3] or girders with corrugated steel webs [4, 5]. Often,

however, the most reasonable solution turns out to be the use of classic composite beams. Steel-concrete composite beams are used in bridges as well as in multi-storey buildings. Such beams may incorporate different types of connectors such as welded headed studs, perfobond connectors, angle and channel connectors, and many others [6].

It should be noted that in a dynamic industry and increased transport, ensuring the safety of bridge structures during day-to-day use plays a key role. Throughout their service life structures incur damage due to environmental and/or human factors. This is why it is important to use structural health monitoring (SHM) systems that allow the condition of the structure to be monitored in real time. The topic of SHM has been taken up by researchers for many years [7–10]. Changes in the dynamic response of a system can be a valuable tool used for detecting damage occurring in a structure.

The energy transfer ratio (ETR) was proposed by Liang and Lee [11]. It determines the ratio of modal energy transferred during a cycle to the total modal energy stored in the structure before that cycle. The energy transferred between vibration modes exists for non-proportionally damped systems, i.e., in systems where the proportional damping relationship given by Caughey and O'Kelly [12] is not satisfied:

$$\mathbf{C}\mathbf{M}^{-1}\mathbf{K} = \mathbf{K}\mathbf{M}^{-1}\mathbf{C}, \tag{1.1}$$

where $\mathbf{M}$, $\mathbf{C}$, $\mathbf{K}$ are the mass, damping, and stiffness matrices, respectively.

It should be noted that proportional damping is often used in practice because it is the simplest damping model, but it cannot be applied to many real-world structures. In fact, engineering structures belong to non-proportional systems. For such systems, the mode shapes are complex [13, 14]. Complex mode shapes are vectors that represent vibrations whose points do not pass through their equilibrium positions at the same time. This means that successive points reach their maximum excursions at different times – they have different phases. A complex mode shape is described by a real part and an imaginary part or, by introducing polar coordinates, by amplitude and phase. For such a system, there is a certain amount of energy transferred between the mode shapes and ETR $\neq 0$. Many previous works have confirmed that the energy transfer ratio is sensitive to damage. Studies conducted for steel-concrete bridge models with damage, such as bearing damage and girder damage, in which ETR was analysed, can be found in [15–17]. In addition, it should be mentioned here that the ETR can be determined globally (for the entire system under analysis) and locally (for individual regions of the system).

Previous studies carried out on damage diagnostics in composite beams have shown that changes in ETR as a result of damage are greater than changes in other modal parameters, such as natural frequency or damping ratio. In [18], the

authors presented the results of numerical analyses for a beam with composite damage at one of its ends. In [19], also based on numerical studies, a composite beam with different types of damage was investigated: (1) damage to the composite but in a different location than before, (2) damage to the concrete slab, and (3) simultaneous damage to the composite and the concrete slab. In a subsequent paper [20], the analysis of the composite damage of a beam was presented both in terms of numerical and experimental tests.

The work presented here is a continuation of the analyses of the sensitivity of ETR to damage in a steel-concrete composite beam. Earlier studies were carried out for other beams and a different type of damage. The choice of the present damage type was dictated by the desire to see how the parameters characterising damping behave as a result of damage to the steel part of the composite beam. Results are presented both for numerical analyses and experimental tests. The analysed beam had previously been tested for changes in natural frequencies and curvature of the mode shape [21]. In this study, the focus is on assessing the sensitivity of the damping ratio and the ETR to damage to the I-beam of the beam. The paper presents the results of the analyses for a globally determined ETR, that is, for the whole beam. As a multi-material system, the composite beam is not proportionally damped. This is due to the fact that steel, concrete and connectors have different damping properties. For such systems, there is an energy transfer between the vibration modes. The parameter that describes this phenomenon is defined as the ETR and is analysed in this paper.

2. Theoretical basis of the ETR

The homogeneous equation of motion for an n-DOF is as follows:

$$\mathbf{M}\ddot{\mathbf{X}} + \mathbf{C}\dot{\mathbf{X}} + \mathbf{K}\mathbf{X} = \mathbf{0}, \tag{2.1}$$

where $\mathbf{M}$, $\mathbf{C}$, $\mathbf{K}$ are the mass, damping, and stiffness matrices $(n \times n)$, and $\ddot{\mathbf{X}}$, $\dot{\mathbf{X}}$, $\mathbf{X}$ are the acceleration, velocity, and displacement vectors $(n \times 1)$, respectively.

Equation (2.1) can also be written in a modified form:

$$\ddot{\mathbf{Y}} + \overline{\mathbf{C}}\dot{\mathbf{Y}} + \overline{\mathbf{K}}\mathbf{Y} = \mathbf{0}, \tag{2.2}$$

where $\mathbf{Y} = \mathbf{M}^{0.5}\mathbf{X}$. The matrices $\overline{\mathbf{C}}$ and $\overline{\mathbf{K}}$ are the damping and stiffness matrices, respectively, defined as $\overline{\mathbf{C}} = \mathbf{M}^{-0.5}\mathbf{C}\mathbf{M}^{-0.5}$ and $\overline{\mathbf{K}} = \mathbf{M}^{-0.5}\mathbf{K}\mathbf{M}^{-0.5}$. For the modified stiffness matrix $\overline{\mathbf{K}}$ there is an eigenvector $\overline{\mathbf{Q}}$. For a system described by Eq. (2.2), it is possible to determine a set of parameters for the i-th mode, such as natural frequencies ω_i, damping ratios ξ_i, and mode shapes $\overline{\mathbf{P}}_i$. When the system is proportionally damped, the relationship $\overline{\mathbf{Q}}_i = \overline{\mathbf{P}}_i$ holds. For non-proportionally damped systems, $\overline{\mathbf{Q}}_i \neq \overline{\mathbf{P}}_i$ and the following relationship exists [11]:

$$\xi_i + j\zeta_i = \frac{1}{2\omega_i} \frac{\overline{\mathbf{Q}}_i^{\mathrm{T}} \overline{\mathbf{C}\mathbf{P}}_i}{\overline{\mathbf{Q}}_i^{\mathrm{T}} \overline{\mathbf{P}}_i}, \tag{2.3}$$

where $j = \sqrt{-1}$. The real part of the right-hand side of Eq. (2.3) is the traditional damping ratio ξ_i, while the complex part of the right-hand side of Eq. (2.3) is the energy transfer ratio ζ_i.

For proportionally damped systems, the vector $\overline{\mathbf{P}}_i$ is real and $\overline{\mathbf{P}}_i = \overline{\mathbf{Q}}_i$, and therefore $\zeta_i = 0$ which indicates the absence of energy transfer between vibration mode shapes. For non-proportionally damped systems, the vector $\overline{\mathbf{P}}_i$ is complex and $\zeta_i \neq 0$, which means that there is energy transfer between the vibration modes.

As can be seen from Eq. (2.3), in order to determine the ETR, it is necessary to know the damping matrix of the system under analysis. If a model of the system under study is available during experimental testing, the damping matrix built for the computational model can be used. As reported in [16], it is also possible to determine the ETR from experimental data alone. In the present analyses, the ETR will be determined using the damping matrix specified for the computational beam model described later in this paper.

More detailed information on the ETR can be found in [11, 15, 16].

3. Experimental studies

The composite beam that was tested consisted of an IPE 160 steel I-beam (S235JRG2 steel) with a span of 3200 mm, a reinforced concrete slab 600 mm wide and 60 mm thick (C30/37 concrete), and perfobond shear connectors (Fig. 1).

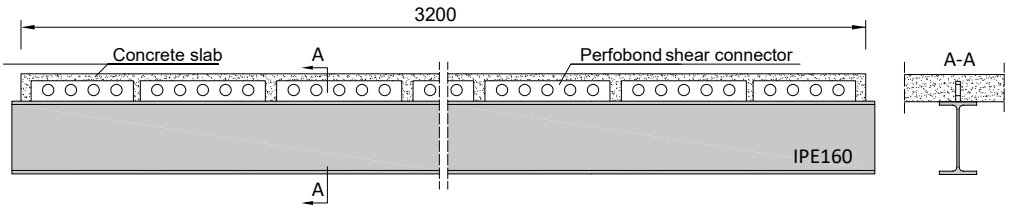

FIG. 1. Tested composite beam.

The analyses were carried out for a free-free beam. In this way, the influence of boundary conditions on the results was eliminated. In order to minimize the influence of support flexibility on the measurement results, the beam was suspended by means of flexible steel cables from a steel frame.

Fifty-two measuring points were located on the beam – 39 points on the upper surface of the concrete slab (visible in Fig. 2a) and 13 measuring points

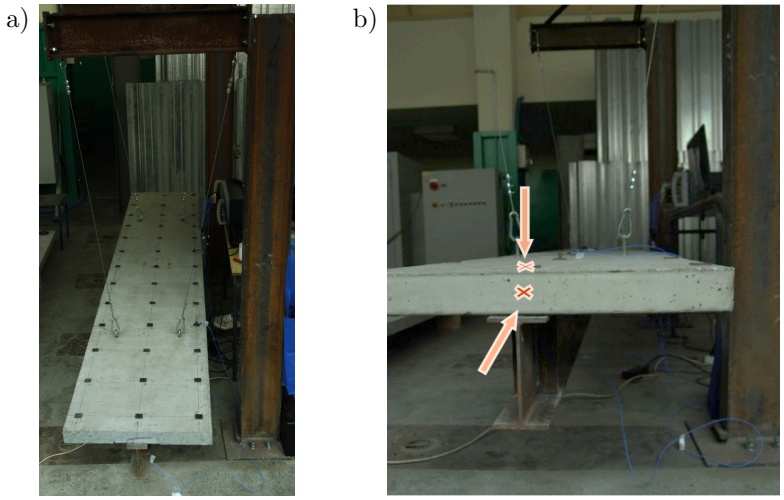

FIG. 2. View of the tested beam (a) and excitation points (b).

on the lower surface of the steel I-beam. An impulse test was carried out using a modal hammer. Accelerations were measured as system responses using piezoelectric acceleration sensors. The LMS SCADAS III signal analyser and LMS Test software (Lab 13A, 2015) were used for the tests. The beam was tested twice – with a force pulse applied to one end of the beam, once along the beam axis and once perpendicular to the surface of the concrete slabs (Fig. 2b). It should be clarified that forcing the beam with a force pulse along the beam axis was intended to determine the fundamental frequency of axial vibration, which was later used to identify the beam model parameters in subsequent stages of the study.

It should be mentioned that, although the beam was surveyed at 52 measurement points, only the measurement points located along the midplane of the beam – the measurement points located on the steel I-beam and the points on the concrete slab directly above the I-beam – were considered for further analysis. Data from points at the edges of the concrete slab were therefore not used. This approach was adopted to enable the construction of a single-plane model of the beam. The measurement points included in the analyses (along with a description of the sensor numbering used) are shown in the Fig. 3.

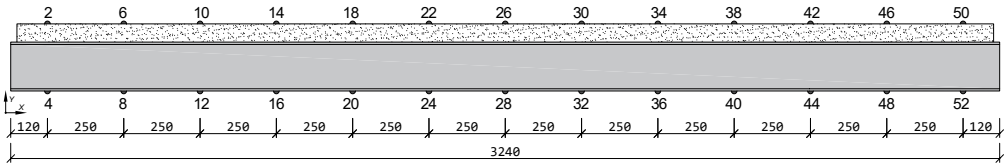

FIG. 3. View of the analysed beam plane with sensor numbering.

Table 1 lists the natural frequencies and the corresponding values of the damping ratios for the first five flexural mode shapes. The initial axial vibration frequency was $f_{1,a,\mathrm{exp}} = 579.66\,\mathrm{Hz}$.

Table 1. Natural frequencies and corresponding damping ratios.

$f_{i,\mathrm{exp}}$ [Hz] →	75.06	178.90	287.98	389.31	489.70
$\xi_{i,\mathrm{exp}}$ [%] →	0.127	0.173	0.284	0.500	0.753

More detailed information on the tested beam is available in [21].

4. Mathematical model of a composite beam

The rigid finite element method (RFEM) [22] was used to model the composite beam. This method has previously been used to model steel-concrete beams with good results [23]. While discrete modelling of structures using RFEM is less well known than the conventional FEM, it provides results that are in good agreement with FEM [24]. The main advantage of RFEM is the significantly smaller number of degrees of freedom of the system compared to the FEM method, which enables easier and faster calculations. The core idea of RFEM is to divide the system into rigid bodies, called rigid finite elements (RFEs), which are connected by spring-damping elements (SDEs). A single-plane model was constructed for the beam (Fig. 4). The steel and concrete parts were modelled separately. In the steel section, the RFEs were connected by not a single, but by three SDEs – located at the axis of the top flange, web and bottom flange. This approach made it possible to introduce damage to the bottom flange of the beam into the model. The use of RFEM in composite beams can also be found in [24, 25].

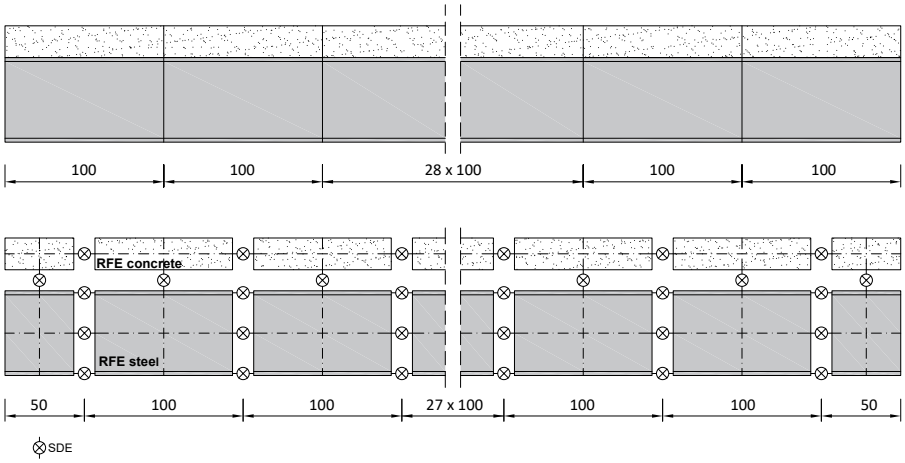

Fig. 4. RFE model of the composite beam.

For the description of the model, the parameters for the steel I-section and the concrete slab were adopted according to Table 2, where E_s is the Young modulus of steel, $\upsilon_{s/c}$ is the Poisson ratio for steel/concrete slab, G_s is the shear modulus of steel (Kirchhoff modulus for steel), $\rho_{s/c}$ is the density of steel/concrete, $A_{s,f}/A_{s,w}$ is the cross-sectional area of the beam flange/web, and h_c is the thickness of the reinforced concrete slab.

Table 2. Beam model parameters.

Steel I-beam						Concrete slab		
E_s [N/m^2]	υ_s	G_s [N/m^2]	ρ_s [kg/m^3]	$A_{s,f}$ [m^2]	$A_{s,w}$ [m^2]	υ_c	ρ_c [kg/m^3]	h_c [cm]
$210 \cdot 10^9$	0.3	$80.77 \cdot 10^9$	7850	$6.07 \cdot 10^{-4}$	$7.95 \cdot 10^{-4}$	0.2	2458.8	6.03

The three missing parameters describing the stiffness properties of the beam: the Young modulus that considers the reinforcement E_c, and the stiffness of the connection in both directions (X and Y) K_X and K_Y were determined based on parametric identification. The identification criteria included the best fit of the first five flexural natural frequencies and the overall fit of the first axial natural frequency obtained from experimental and numerical analyses. Table 3 contains identified beam stiffness parameters and flexural vibration frequency values of the beam determined for the model.

Table 3. Identified beam stiffness parameters and beam flexural vibration frequencies.

E_c [GPa]	K_X [N/m]	K_Y [N/m]	$f_{1,\text{num}}$ [Hz]	$f_{2,\text{num}}$ [Hz]	$f_{3,\text{num}}$ [Hz]	$f_{4,\text{num}}$ [Hz]	$f_{5,\text{num}}$ [Hz]
28.7	$8.10 \cdot 10^8$	$2.78 \cdot 10^8$	75.79	177.63	287.99	391.49	487.97

More detailed information on the model and the identification of stiffness properties is available in [21].

In order to determine the damping properties of the beam, the material loss factor μ was used. The loss factor is a characteristic of the material from which a component is made. For multi-material structures, it is a function of the damping of the individual constituent materials from which the structure is made. For the composite beam under consideration, three loss factors had to be considered – for the steel, the concrete, and the connection. All three components affect the damping properties of the beam.

For the Kelvin–Voight damping model, the relationship between the damping coefficients and stiffness coefficients for the k-th spring-damping element (SDE) is expressed as follows [26]:

$$c^k = \frac{\eta}{\omega} k^{(k)}. \tag{4.1}$$

For the beam tests, the loss factor for steel was assumed to have a constant value of $\eta_s = 4 \cdot 10^{-4}$. In [27], it can be found that the loss factor for steel is $\eta_s = (2 \div 6) \cdot 10^{-4}$. As the concrete slab is reinforced, its loss factor is also influenced by the reinforcement used. Therefore, the loss factors for the concrete slab and the connection were determined by parametric identification. It consisted of fitting frequency response functions (FRFs) obtained from numerical model to those from the experimental studies. The analyses included the first three resonances of the flexural mode shapes and one axial mode for four selected measurement points. The choice of measurement points adopted for identification was dictated by their locations on the beam.

Based on this identification, the values of the loss factors were obtained: $\eta_c = 70 \cdot 10^{-4}$ for the concrete slab, and $\eta_{\text{conn}} = 418 \cdot 10^{-4}$ for the connection. Figure 5 and Fig. 6 show the FRFs obtained during the experimental tests and those from the model after identification.

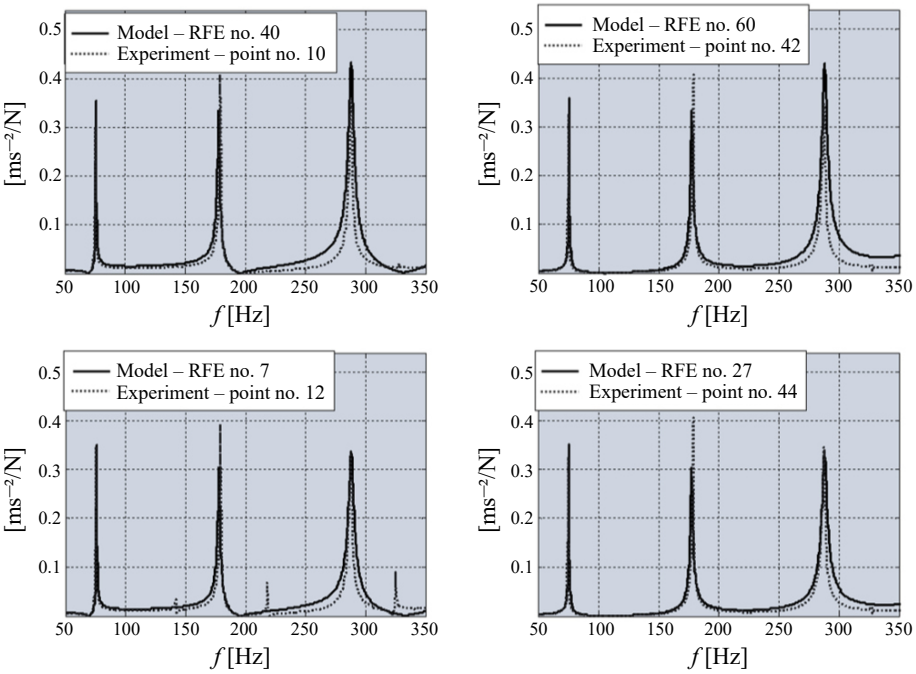

FIG. 5. FRF obtained from experimental tests and from the model with excitation in the Y-axis direction.

In order to check the compatibility of the model with the experimental results, the modal assurance criterion (MAC) values were determined for the first five determined modes of flexural vibration. As the MAC values for the fourth and fifth modes of vibration were below 0.8, these modes of vibration were not taken into account in further analyses.

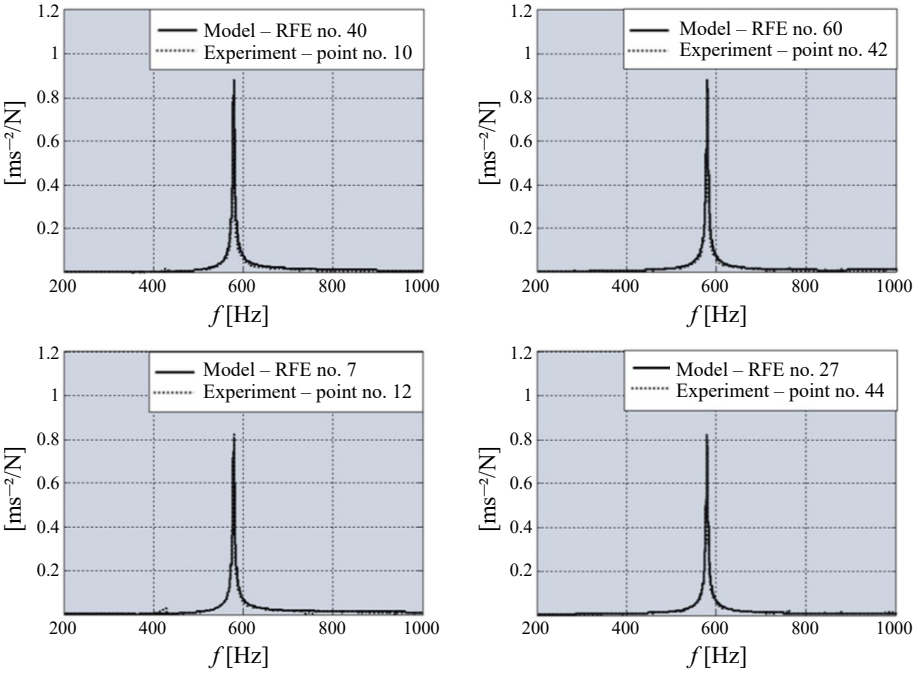

FIG. 6. FRF obtained from experimental tests and from the model with excitation in the X-axis direction.

5. BEAM DAMAGE SIMULATION

Damage was introduced to the I-section steel beam by incising the bottom flange over its full width (Fig. 7).

FIG. 7. Damage to the bottom flange.

The damage was located at two points – indicated in Fig. 8 by symbols A and B. In the first stage, a flange incision was introduced at point 1 (damage D1). In the next stage, a flange incision was introduced at point 2 (damage D2).

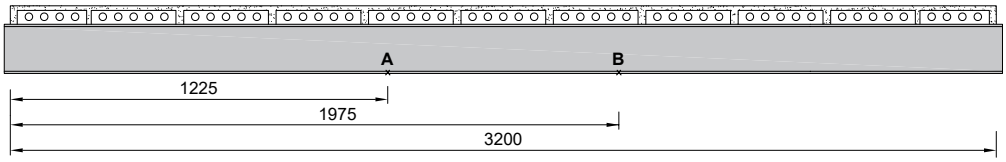

FIG. 8. Locations of damage.

The numerical simulation of the damage consisted of changing the elastic properties (the beam flange cross-sectional area $A_{s,f} = 0$ and moment of inertia of the flange about the Z-axis of the cross-section $I_{z,s,f} = 0$) of the corresponding SDEs modelling the bottom flange. These properties were set: a) for damage D1 at location 1, and b) for damage D2 at locations 1 and 2, respectively.

6. RESEARCH RESULTS

Changes in modal parameters as a result of damage were determined using the index Δ_i:

$$\Delta_i = \left| \frac{x_{i,d} - x_{i,u}}{x_{i,u}} \right|, \tag{6.1}$$

where $x_{i,d}$ and $x_{i,u}$ denote the modal parameter in the damaged and undamaged states, respectively.

6.1. Damping ratio

The values of the damping ratio and their changes due to the introduced damages D1 and D2, presented separately for experimental test results and the numerical model, are presented in Table 4. The condition of the beam without damage is denoted as D0. Changes in the damping ratio also illustrated graphically in Fig. 9.

TABLE 4. Damping ratios before and after damage.

	Beam state									
	Experimental test					Numerical model				
	D0	D1		D2		D0	D1		D2	
i	$\xi_{i,\text{exp}}$ [%]	$\xi_{i,\text{exp}}$ [%]	Δ_i [%]	$\xi_{i,\text{exp}}$ [%]	Δ_i [%]	$\xi_{i,\text{num}}$ [%]	$\xi_{i,\text{num}}$ [%]	Δ_i [%]	$\xi_{i,\text{num}}$ [%]	Δ_i [%]
1_{flex}	0.127	0.137	8.0	0.137	7.6	0.236	0.237	0.7	0.238	1.0
2_{flex}	0.173	0.186	7.9	0.265	53.5	0.473	0.467	1.1	0.462	2.2
3_{flex}	0.284	0.309	8.7	0.296	4.0	0.683	0.681	0.3	0.679	0.6

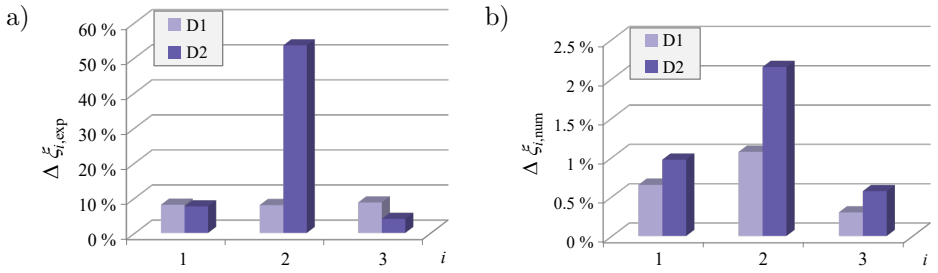

FIG. 9. Changes in damping ratio before and after damage:
a) experimental test, b) numerical model.

As presented, small changes in the modal damping ratio were observed as a result of the numerical damage simulation. The largest changes in the numerical analyses were only 2.2 %. Higher sensitivity was obtained during the experiment, with changes of a few percent, except for one value reaching 53.5 %. It can also be observed that the modal damping ratios determined from the numerical model were higher than those obtained during experimental tests. The maximum changes in damping ratio appeared to coincide for both the experiment and numerical analyses, occurring for the second mode shape at damage D2.

6.2. ETR

The ETR was determined from Eq. (2.3). A prerequisite for the determination of this ratio according to Eq. (2.3) is knowledge of the damping matrix $\overline{\mathbf{C}}$. It should be noted that the $\overline{\mathbf{C}}$ matrix determined for the numerical model was also used to determine the ETR from experimental tests. The values of the ETR and their changes due to the introduced damages D1 and D2 are shown in Table 5. The condition of the beam without damage is denoted as D0. Changes in the ETR are also graphically illustrated in Fig. 10.

TABLE 5. Changes in ETR index before and after damage.

	Beam state									
	Experimental test					Numerical model				
	D0	D1		D2		D0	D1		D2	
i	$\zeta_{i,\mathrm{exp}}$ [‰]	$\zeta_{i,\mathrm{exp}}$ [‰]	Δ_i [%]	$\zeta_{i,\mathrm{exp}}$ [‰]	Δ_i [%]	$\zeta_{i,\mathrm{num}}$ [‰]	$\zeta_{i,\mathrm{num}}$ [‰]	Δ_i [%]	$\zeta_{i,\mathrm{num}}$ [‰]	Δ_i [%]
1_{flex}	5.420	2.980	45.0	3.610	33.4	0.050	0.048	4.3	0.046	8.2
2_{flex}	1.712	0.587	65.7	1.011	40.9	0.108	0.106	2.3	0.103	5.0
3_{flex}	1.584	0.696	56.1	0.529	66.6	0.138	0.138	0.3	0.138	0.5

As shown, large changes in the ETR as a result of the damage introduced were observed in the experimental tests – with all changes in the range of tens

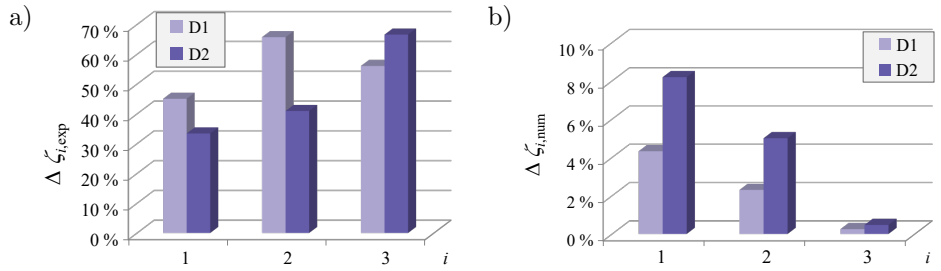

Fig. 10. Changes in ETR before and after damage: a) experimental test, b) numerical model.

of percent. These are significantly larger values than those obtained for the damping ratio. Analysing the results of numerical tests – a few percent changes in ETR were obtained, which still turned out to be larger than those obtained for the damping ratio (except for for the third mode shape, where these changes were at a similar level).

7. Conclusions

This paper aimed to assess the sensitivity of modal parameters characterising damping in non-proportionally damped systems. Damage was introduced to the bottom flange of a steel I-beam in a steel-concrete composite beam. The results obtained from experimental tests and from the numerical model were analysed. The sensitivity of the damage introduced was assessed for two damping parameters – the damping ratio and the ETR. As a result of the experimental tests and numerical analyses for the composite beam, a little sensitivity of the damping ratio to damage introduced into the beam was observed. The damping ratio is therefore not a good indicator of damage for the beam under analysis. Regarding the ETR – it was observed that the ETR was more sensitive to introduced damage than the damping ratio. Additionally, the ETR was more responsive to changes in the composite beam than the damping ratio. This suggests that perhaps the ETR could be used as a damage detection tool. It should be mentioned that, although this paper analysed one type of damage in a single composite beam, the method based on variations in ETR due to damage can be applied to different structures using different numerical modelling techniques. Studies by other researchers, in which ETR changes were analysed, were performed on composite bridge models [15–17], showing that the method can be applied to a variety of structures. To estimate the energy transfer for a vibration mode, it is necessary to know the frequency, mode shape, and damping matrix. Consequently, various numerical modelling techniques can be used to build the computational model. The determination of the ETR for non-proportionally damped systems is based on changes in the complex mode shape

of vibration. In order to avoid errors in phase determination, the method requires a great deal of care when taking measurements. The presence of uncontrolled measurement noise can affect the results obtained. Nevertheless, the continuous development of technology provides new opportunities. New technologies are also being introduced into SHM for engineering structures, allowing more precise measurements. Perhaps, the ETR could be used as a potential tool for damage detection.

Fundings

The project has been financed by the National Science Centre.

Conflict of interest

The author declares that she has no known competing financial interests or personal relationships that could have appeared to influence the work reported in this paper.

Author's contribution

The author reviewed and approved the final manuscript.

Acknowledgments

The manuscript was prepared as a conference paper for the 31st Conference on Vibrations in Physical and Technical Systems, October 16–18, 2024, Poznań, Poland.

References

1. Choo J.F., Choi Y.C., Choi W.C., Yoo S.W., Behavioral characteristics of hybrid girders according to type of steel–concrete connection, *Archives of Civil and Mechanical Engineering*, **19**(1): 47–62, 2019, https://doi.org/10.1016/j.acme.2018.08.008.
2. Haque M.N., Maki T., Experimental study on time-dependent deformation of hybrid steel–PRC girder with headed stud shear connections under sustained loading, *Structures*, **22**: 327–340, 2019, https://doi.org/10.1016/j.istruc.2019.09.004.
3. Kim S.E., Nguyen H.T., Evaluation of the connection efficiency of hybrid steel-concrete girder using finite element approach, *International Journal of Mechanical Sciences*, **61**(1): 8–23, 2012, https://doi.org/10.1016/j.ijmecsci.2012.04.008.
4. Ghanim G., Baldawi W.S., Ali A.A., A review of composite steel plate girders with corrugated webs, *Engineering and Technology Journal*, **39**(12): 1927–1938, 2021, https://doi.org/10.30684/etj.v39i12.2193.

5. Chen Y., Dong J., Xu T., Composite box girder with corrugated steel webs and trusses – A new type of bridge structure, *Engineering Structures*, **166**: 354–362, 2018, https://doi.org/10.1016/j.engstruct.2018.03.047.

6. Pardeshi R.T., Patil Y.D., Review of various shear connectors in composite structures, *Advanced Steel Construction*, **17**(4): 394–402, 2021, https://doi.org/10.18057/IJASC.2021.17.4.8.

7. Sohn H., Farrar C.R., Hemez F.M., Czarnecki J.J., Shunk D.D., Stinemates D.W., Nadler B.R., *A review of structural health monitoring literature*, Los Alamos National Laboratory Report, LA-13976-MS, pp. 1996–2001, 2003.

8. Montalvão D., Maia N.M.M., Ribeiro A.M.R., A review of vibration-based structural health monitoring with special emphasis on composite materials, *Shock and Vibration Digest*, **38**(4): 295–324, 2006, https://doi.org/10.1177/0583102406065898.

9. Das S., Saha P., Patro S.K., Vibration-based damage detection techniques used for health monitoring of structures: A review, *Journal of Civil Structural Health Monitoring*, **6**(3): 477–507, 2016, https://doi.org/10.1007/s13349-016-0168-5.

10. Yang Y., Zhang Y., Tan X., Review on vibration-based structural health monitoring techniques and technical codes, *Symmetry*, **13**(11): 1–18, 2021, https://doi.org/10.3390/sym13111998.

11. Liang Z., Lee G.C., *Damping of structures: Part 1 – Theory of complex damping*, National Center for Earthquake Engineering Research, Technical Report NCEER-91-0004, State University of New York at Buffalo, 1991.

12. Caughey T.K., O'Kelly M.E.J., Classical normal modes in damped linear dynamic systems, *Journal of Applied Mechanics*, **32**(3): 583–588, 1965, https://doi.org/10.1115/1.3627262.

13. Ewins D.J., *Modal Testing: Theory, Practice, and Application*, 2nd ed., Research Studies Press, England, 2000.

14. Wenzel H., Pichler D., *Ambient Vibration Monitoring*, John Wiley & Sons, England, 2005.

15. Zong Z.H., Wang T.L., Structural damage identification by using energy transfer ratio, [in:] *Conference Proceedings, 21st IMAC Conference and Exposition (IMAC XXI), A Conference and Exposition on Structural Dynamics*, Kissimmee, Florida, 2003.

16. Wang T.L., Zong Z., *Improvement of evaluation method for existing highway bridges*, Technical Report FL/DOT/RMC/6672-818, Florida Department of Transportation, USA, 2002.

17. Lee G.C., Liang Z., Development of a bridge monitoring system, [in:] *Proceedings of the 2nd International Workshop on Structural Health Monitoring*, pp. 349–358, Stanford University, California, 1999.

18. Wróblewski T., Jarosińska M., Berczyński S., Application of ETR for diagnosis of damage in steel-concrete composite beams, *Journal of Theoretical and Applied Mechanics*, **49**(1): 51–70, 2011.

19. Wróblewski T., Jarosińska M., Berczyński S., Damage location in steel-concrete composite beams using energy transfer ratio (ETR), *Journal of Theoretical and Applied Mechanics*, **51**(1): 91–103, 2013.

20. Wróblewski T., Jarosińska M., Abramowicz M., Berczyński S., Experimental validation of the use of energy transfer ratio (ETR) for damage diagnosis of steel-concrete composite beams, *Journal of Theoretical and Applied Mechanics,* **55**(1): 241–252, 2017, https://doi.org/10.15632/jtam-pl.55.1.241.

21. Jarosińska M., Wróblewski T., Identification of damage to a steel I-beam based on changes in frequency and curvature of the mode shape in a steel-concrete composite beam, *Archives of Civil Engineering*, **71**(2): 575–590, https://doi.org/10.24425/ace.2025.154138.

22. Kruszewski J., Gawroński W., Wittbrodt E., Najbar F., Grabowski S., *The Rigid Finite Element Method* [in Polish: *Metoda Sztywnych Elementów Skończonych*], Arkady, Warszawa, 1975.

23. Berczyński S., Wróblewski T., Experimental verification of natural vibration models of steel-concrete composite beams, *Journal of Vibration and Control*, **16**(14): 2057–2081, 2010, https://doi.org/10.1177/1077546309350552.

24. Abramowicz M., Pełka-Sawenko A., Comparison of the finite element method and rigid finite element method during dynamic calculations of steel–concrete composite beams based on experimental results, *Materials*, **17**(24): 6081, 2024, https://doi.org/10.3390/ma17246081.

25. Abramowicz M., Berczyński S., Wróblewski T., Modelling and parameter identification of steel–concrete composite beams in 3D rigid finite element method, *Archives of Civil and Mechanical Engineering*, **20**: 103, 2020, https://doi.org/10.1007/s43452-020-00100-7.

26. Kruszewski J., Sawiak S., Wittbrodt E., *Computer-aided Design CAD/CAM, The Rigid Finite Element Method in Dynamics of Structures* [in Polish: *Wspomaganie Komputerowe CAD/CAM, Metoda Sztywnych Elementów Skończonych w Dynamice Konstrukcji*], Wydawnictwa Naukowo-Techniczne, Warszawa, 1999.

27. Rao S.S., *Mechanical Vibrations*, 5th ed., Prentice Hall, 2011.

Received December 18, 2024; revised May 31, 2025; accepted June 5, 2025; version of record March 9, 2026; published issue March 30, 2026.

Engineering Transactions, **74**(1): 19–38, 2026, https://doi.org/10.24423/engtrans.2025.3561
Institute of Fundamental Technological Research Polish Academy of Sciences (IPPT PAN)
Université de Lorraine • Poznan University of Technology

Research Paper

Evaluation of the Characteristics and Application of SBS Composite-Modified Bitumen Materials in Low-Temperature Environments

Wenxiao REN[1),2)], Ping LI[1)*]

[1)] *School of Civil Engineering, Lanzhou University of Technology*
Lanzhou, China

[2)] *School of Civil Engineering, Northwest Minzu University*
Lanzhou, China

[*]Corresponding Author: lzlgliping@126.com

To improve the resistance of bitumen pavements to low-temperature cracking, this study proposes a composite-modified bitumen based on styrene-butadiene-styrene (SBS) copolymer and crumb rubber. This modified bitumen is also tested for its performance in a low-temperature environment. The test results indicate that, after aging and freeze-thaw cycles (FTCs), the creep rates (CRs) of both SBS-modified bitumen and the SBS/crumb rubber composite-modified bitumen decreased. However, the CR of the SBS/crumb rubber composite-modified bitumen was constantly lower than that of the SBS-modified bitumen. For example, at $-12\,^{\circ}\mathrm{C}$, the CRs of the aged SBS-modified bitumen and SBS/crumb rubber composite-modified bitumen were 0.44 and 0.37, respectively. When the bitumen mixtures underwent FTCs and aging, their fracture energy densities (FEDs) drastically decreased. Nevertheless, the FEDs of the SBS/crumb rubber composite-modified bitumen mixtures were higher than those of the SBS-modified bitumen mixtures. These results indicate that the composite-modified bitumen with SBS/crumb rubber has good rheological properties and freeze-thaw resistance, thereby effectively ensuring the low-temperature performance of bitumen pavements.

Keywords: SBS, modified bitumen, rheological properties, low-temperature properties, freeze–thaw cycles (FTCs), crumb rubber.

1. Introduction

As the most common pavement surfacing material, bitumen pavement (AP), compared with other pavements, has the advantages of a smooth surface, comfortable driving, and easy maintenance and repair. However, in low-temperature (LT) environments, the bitumen binding material is prone to cracking, which seriously affects the performance and life of AP [1, 2]. The LT cracking problem of AP can be improved by enhancing the rheological properties of bitumen. One

typical bitumen modification that can successfully increase the ductility and viscoelasticity of bitumen while lowering its temperature sensitivity is styrene butadiene styrene copolymer (SBS copolymer) [3, 4].

In the 1840s, researchers first attempted to mix natural rubber into base bitumen to prepare modified bitumen. Later, synthetic rubber and natural rubber were used to modify base bitumen. However, it was not until the 1930s that the preparation process of rubber-modified bitumen was more effectively improved. In the 1960s, rubber powder obtained from waste tires began to be added to base bitumen in some countries to prepare rubberized bitumen and apply it to road construction. However, due to the poor compatibility between rubber powder and bitumen, many undispersed rubber particles remain, resulting in disadvantages such as high viscosity, poor flowability, and poor dispersibility of bitumen. Liu *et al.* [5] proposed a method of using carbon nanotubes (CNTs) mixed with SBS-modified bitumen to address the issue of early damage to bitumen pavements. Their study analyzed the effects of different CNT concentrations on the high-temperature (HT) and LT performance, as well as the aging behavior of SBS-A, through a series of experiments. The results showed that the optimal concentration of CNTs was 1 %, and the changes in modified bitumen during aging were analyzed by infrared spectroscopy. Ting *et al.* [6] proposed a composite modified asphalt (MA) based on SBS and methylene diphenyl diisocyanate (MDI) to address the problem of poor stability of SBS-MA. MDI, according to the experimental findings, acted as a phase compatibilizer between bitumen and SBS, improving the composite-modified phase stability of bitumen while decreasing its chemical softness and polarizability. Duarte Mendonça *et al.* [7] addressed the problem of how to improve the elasticity of bitumen by proposing a lignin-based MA. According to the testing results, the addition of 3 % pine lignin and 9 % eucalyptus lignin produced bitumen with the best mechanical qualities, indicating that lignin is an excellent alternative to synthetic elastomeric polymers.

To address the issue of how to enhance the HT and LT properties as well as the water stability of bitumen, Li *et al.* [8] presented an MA based on bamboo fiber. According to the experimental findings, bamboo fiber MA blends performed better in terms of HT, LT, and water stability compared with SBS-MA. With a fiber length of 7.25 mm and a content of 0.22 %, the optimum performance of the bitumen was obtained. Amini *et al.* [9] proposed a composite MA based on titanium dioxide, aluminum trioxide, and multiwalled CNTs to improve rutting and fatigue resistance of bitumen. The experimental results indicated that this MA had higher viscosity, better aging resistance, and a fatigue life that was 1.7 times longer than that of ordinary bitumen. Chen *et al.* [10] proposed to improve the performance of SBS-modified bitumen by grinding molybdenum disulfide (MoS_2) with polyphosphoric acid (PPA) in cyclic oil and mechanically

activating the mixture to produce PPA-modified MoS_2 (OMS-PPA), which was then mixed with SBS-modified bitumen. The results showed that, compared with SA, the permeation temperature coefficient of SA-OMS decreased by 3.7 %, and that of 1-SA-OMS-PPA decreased even more, i.e., by 7.1 %. After short-term aging, the generation of carboxyl groups and the rate of hardness were significantly reduced.

In summary, the current research on MA has been quite effective, and many different types of MA have been developed. However, most of the research on MAs primarily focused on their mechanical properties, while their their freeze-thaw cycles (FTC) resistance was relatively neglected. In view of the latter issue, in order to improve the FTC resistance of bitumen and minimize the manufacturing cost of modified bitumen, the FTC performance of composite modified bitumen based on SBS and rubber powder is analyzed. Moreover, to evaluate the performance of the composite MA, the study also innovatively analyzes the rheological and LT properties of the MA from both macro- and fine-scale perspectives.

2. Methods and materials

Gram-refined bitumen was selected as the matrix bitumen (MaA) for the experiment. The SBS modifier used was 4303 star type. The rubber powder modifier consisted of 40-mesh (380 μm) rubber powder particles. The optimal dosages of the SBS modifier and rubber powder modifier were determined through experiments on three major indicators of bitumen: dynamic shear, bending, and rheology in the early stage. The dosages of the SBS modifier and rubber powder modifier were 3 % and 20 % of the mass of the matrix bitumen, respectively. SBS-MA was prepared by blending SBS modifier into MaA. SBS composite crumb rubber (CCR) MA was prepared by blending the SBS modifier and the crumb rubber modifier into MaA. The coarse and fine aggregates used in the preparation of the bitumen mixtures (AMs) were basalt, comprising 97 % of the total. The mineral powder was limestone – 3 % of the total and having a fineness of less than 0.075 mm. The optimum oil/gravel ratios for the preparation of AMs with SBS-modified bitumen and CCR bitumen were 5 % and 6 %, respectively. The so-called oil-stone ratio refers to the mass ratio of asphalt (oil content) to aggregate (stone content) in asphalt mixtures. It is an important parameter in the design of asphalt mixtures, which has a significant impact on their performance.

In preparing the AM specimens, the mixture was first pressed into 300 mm × 300 mm × 50 mm rutted specimens using the wheel milling method. Then, the rutted specimen was cut into 250 mm × 30 mm × 35 mm beams. Moreover, a 4 mm × 2 mm notch was cut at the midpoint of the beamlet for subsequent tests.

2.1. Experimental design

Long-term aging (LTA) test of bitumen: 50 g of SBS bitumen and CCR bitumen were each put into a sample tray, and then short-term aging was carried out using a rotating film oven, with the heating time of 5 h and temperature of 163 °C, with a rotating speed of 5.5 rad/min. Then, the aged bitumen was poured into a sample tray to achieve a thickness of 3.2 mm. Next, it was placed into a pressure aging vessel (PAV) for 20 h for LTA simulation. The PAV temperature was set at 100 °C and the pressure to 2.1 MPa [11]. When the aging was completed, the bitumen samples were removed and placed in a stainless steel cylinder with heating and stirring to remove air bubbles inside the bitumen.

LTA test of the mixture: first, the AM was baked in an oven for 4 h at 135 °C after being evenly spread at a thickness of 21 kg/m^2 in an enameled tray. Then, the mixture was pressed into rutting specimens using the wheel milling method and cut into small beams. Subsequently, the obtained trabecular specimens were placed in a HT and LT alternating box heated under forced ventilation for 120 h at a heating temperature of 85 °C [12]. After heating, the door of the box was opened, and the specimens were removed after cooling to room temperature.

Bitumen FTC test: first, 50 g of SBS bitumen and CCR bitumen were weighed and evenly spread in a stainless steel cylinder (diameter: 122 mm) to a thickness of 3.2 mm. Then, the stainless steel cylinder was filled with water and an 8 % salt solution until the bitumen was fully submerged. Next, the stainless steel cylinder was sealed using cling film and placed in a HT and LT alternating chamber for freeze-thaw cycling. The freezing temperature was set at −20 °C for 2 h, and the thawing temperature at 60 °C for 4 h. The number of FTCs was 5, 10, 15, and 20.

FTC test: the specimens were first placed in water or salt solution (8 %). Then, the specimens were evacuated using a vacuum extractor to a vacuum level of 97.3 kPa, and the specimens were immersed under vacuum conditions for 15 min. After this, atmospheric pressure was restored and the immersion was continued for an additional 1 h. Then, the specimens were taken out and placed in a specimen box, which was filled with water or the 8 % salt solution until the specimens were fully submerged. Next, they were placed in a HT and LT alternating chamber for FTC [13]. The freezing temperature and time were −20 °C for 8 h. The melting temperature and time were 60 °C for 16 h. The number of FTCs was 5, 10, 15 and 20.

2.2. Experimental design of rheological and physico-chemical properties

Bending creep strength test: the test equipment was a bending beam rheometer, and the test indices were stiffness modulus and creep rate (CR). The test temperatures were −24 °C, −18 °C, and −12 °C.

Infrared spectroscopic tests: infrared tests were performed on different specimens using a Fourier transform infrared (FTIR) spectrometer. The number of scans and spectral acquisition intervals were 32 cm^{-1} and 650 cm^{-1} to 4000 cm^{-1}, respectively, and the resolution was 4 cm^{-1}.

Contact angle measurement test: first, the bitumen was heated until it was molten, and then it was put on a slide. After that, the slide was heated on a hot plate and left to flow naturally. The heating temperature was 120 °C. After cooling, the bitumen was placed in a sealed container and set aside. Next, the basalt aggregate was cut into cubes with a side length of 1 cm and polished to a smooth surface. The polished basalt specimens were then placed in an oven for drying at 45 °C for 6 h [14]. After the basalt specimens cooled to room temperature, they were removed and placed in a sealed container for backup. Then, the contact angle of the specimens was measured by dropping a liquid drop onto the specimen surface to be tested using the probe of a contact angle measuring instrument.

Atomic force microscopy (AFM) test: for the test, the scanning mode of the AFM was PeakForce QNM, the scanning frequency was 0.977 Hz, the scanning range was 20 μm × 20 μm, and the probe used was Bruker RTESPA-150.

2.3. LT *cracking property test*

Constrained specimen temperature stress (CSTS) test: first, epoxy resin adhesive was utilized to bond the ends of the AM beamlet specimen to the ends of the test system. After the epoxy resin adhesive solidified, the specimen was kept at 5 °C for 6 h. Then, the specimen was cooled at a rate of 10 °C/h and the temperature-stress curve was measured until the specimen fracture.

Three-point bending test (TPBT): the specimen was placed flat in the bending test fixture to form a simply-supported beam, and a dynamic hydraulic servo universal testing machine was utilized to apply the load. The loading speed was 1 mm/min, the test temperature was −12 °C, and the acquisition frequency was 10 Hz. It should be mentioned that the specimen was first coated with matte white paint throughout the collecting procedure in order to prevent specimen reflection. Moreover, a roller was used to make black spots on the surface of the specimen as markers to ensure accurate data acquisition.

2.4. Anti-rutting test

Rutting plate specimens were prepared using the bitumen mixture and rutting tests were conducted using the SYD-0719C-2 fully automatic rutting tester. Constant wheel pressure and uniform wheel speed were maintained during the experimental loading process. The rutting plate specimen together with the test mold were placed on the testing device, with the test wheel placed at the center

of the specimen. The travel direction of the test wheel was consistent with the rolling direction, and the test duration was 1 h. The test was stopped when the rutting deformation reached 25 mm.

3. Results

3.1. LT rheological characterization of composite MA

To evaluate the rheological properties of CCR bitumen, flexural creep strength tests were conducted on virgin, aged, and FTC-treated MA. The specimens were analyzed using infrared spectroscopy. The basic properties of CCR bitumen are shown in Table 1.

Table 1. Basic properties of CCR bitumen.

Item	Unit	Value
Needle penetration	dmm	52.5
Softening point	°C	228
Ductility	cm	85.7

As can be seen in Table 1, the penetration, softening point, and ductility of the CCR bitumen are 52.5 dmm, 228 °C, and 85.7 cm, respectively. Figure 1 displays the stiffness modulus of the MA at various temperatures.

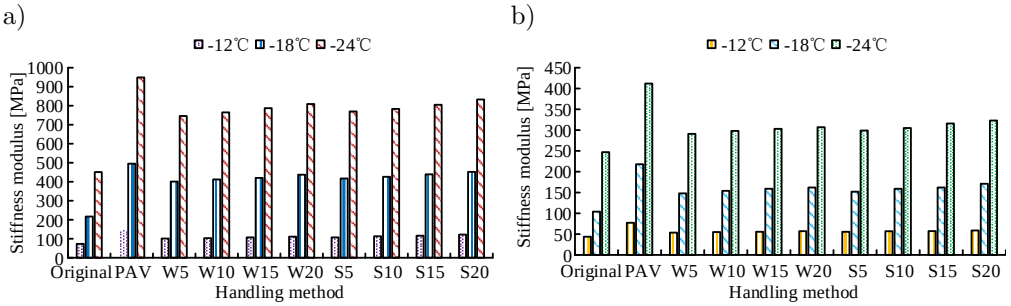

Fig. 1. Stiffness modulus of MA at different temperatures and treatments: a) stiffness modulus of SBS-MA, b) stiffness modulus of CCR-modified asphalt. Note: Wx and Sx represent x FTCs in water and salt solution, respectively.

In Fig. 1a, compared to the virgin SBS bitumen, the stiffness modulus of SBS bitumen after LTA and water/salt FTCs increased significantly and was inversely proportional to the temperature. Among the samples, the PAV-aged SBS bitumen had the largest stiffness modulus, with values of 145 MPa, 495 MPa, and 949 MPa at −12 °C, −18 °C, and −24 °C, respectively. In Fig. 1b, the stiffness modulus of CCR bitumen, after both aging and FTC, increased compared to the original CCR bitumen. Furthermore, as the temperature decreased, the modulus

rose. Among the samples, the PAV-aged CCR bitumen at −24 °C showed the largest stiffness modulus of 412 MPa. Under identical conditions, the stiffness modulus of the CCR bitumen was lower than that of the SBS bitumen. The aforementioned findings suggest that the CCR bitumen has superior LT rheological characteristics compared with the SBS bitumen. Figure 2 depicts the CR of the MA at various temperatures.

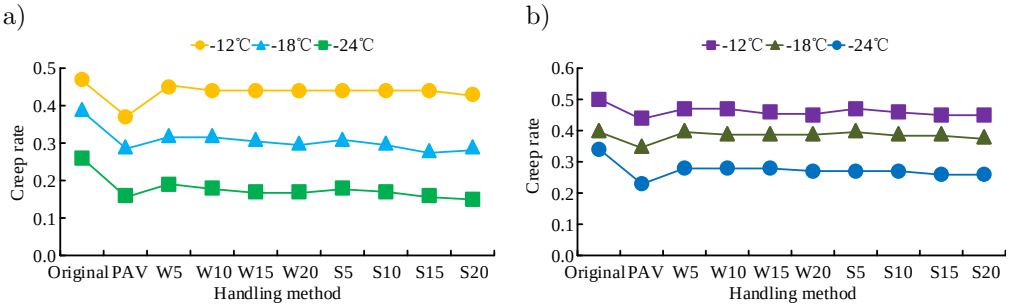

Fig. 2. CR of MA at different temperatures:
a) CR of SBS-MA, b) CR of CCR-MA.

In Fig. 2, the CR of MA, after aging and FTC, decreased compared with the original MA. The most significant reduction in the CR of the aged bitumen was at least 10.9 %. In addition, the CR of the MA decreased as temperature decreased. However, by comparing Fig. 2a and Fig. 2b, it can be observed that the change in the CR of CCR bitumen is relatively small compared to that of SBS bitumen. For example, after the aging treatment, the CR of SBS bitumen and CCR bitumen at −12 °C was 0.37 and 0.44, respectively. These results show that the CCR bitumen has better strain relaxation ability compared with the SBS bitumen. The CR/stiffness modulus ratios of MA at different temperatures are displayed in Table 2.

In Table 2, the CR/stiffness modulus ratios of both SBS bitumen and CCR bitumen decreased significantly after aging and FTC. Taking the PAV-aged bitumen at −12 °C as an example, the CR/stiffness modulus ratios for SBS and CCR bitumen were 257.4 and 571.6, representing reduction of 60.2 % and 49.5 %, respectively. Meanwhile, with the decrease in temperature and the increase in the FTCs, the CR/stiffness modulus ratios of both SBS bitumen and CCR bitumen decreased. In addition, under the same conditions, the CR/stiffness modulus ratio of CCR bitumen was always higher than that of SBS bitumen. For example, at −18 °C, the CR/stiffness modulus ratios of SBS bitumen and CCR bitumen after aging were 58.6 and 160.6, respectively. These results demonstrate that CCR bitumen exhibits excellent LT deformation capability compared with SBS bitumen. Figure 3 displays the infrared spectra of various MA samples before and after aging.

Table 2. CR/stiffness modulus ratio (10^5/MPa) of SBS- and CCR-MAs at different temperatures.

Bitumen type	Processing method	−12 °C	−18 °C	−24 °C
SBS-MA	Original	647.3	179.7	57.6
	PAV	257.4	58.6	16.9
	W5	441.5	79.8	25.5
	W10	429.2	77.7	23.5
	W15	411.4	73.8	21.6
	W20	393.1	68.6	21.0
	S5	414.2	74.3	23.4
	S10	389.6	70.4	21.7
	S15	379.5	63.8	19.9
	S20	355.1	64.2	18.0
CCR-MA	Original	1134.9	384.6	133.6
	PAV	571.6	160.6	55.8
	W5	884.3	270.3	96.2
	W10	849.2	253.2	94.0
	W15	818.5	245.3	92.4
	W20	786.2	240.7	87.9
	S5	846.9	263.2	90.3
	S10	810.4	245.3	88.5
	S15	792.3	240.7	82.3
	S20	761.7	222.2	80.5

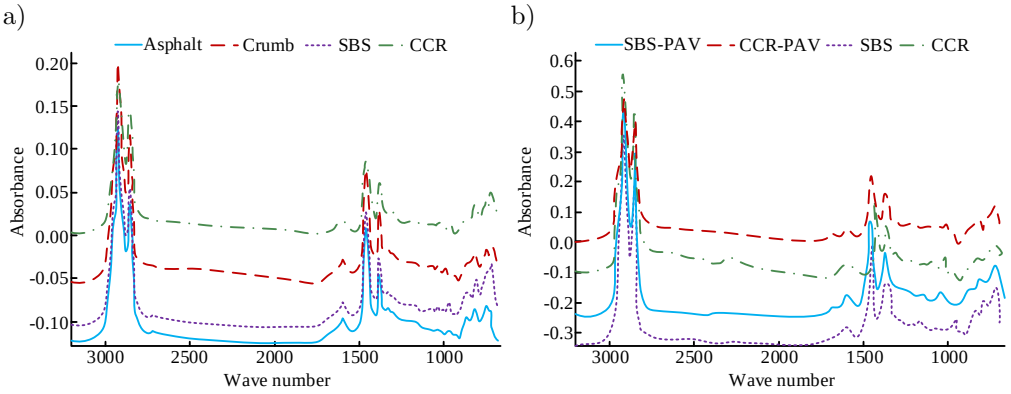

Fig. 3. Infrared spectrum before and after aging of different modified bitumen: a) infrared spectra of asphalt samples, b) infrared spectra of asphalt before and after aging.

In Fig. 3a, the absorption peaks of MaA, crumb rubber MA, SBS bitumen, and CCR bitumen are basically located at the same position, i.e., at wave num-

bers of 2918.2 cm^{-1} and 2849.5 cm^{-1} in the functional group region. All these absorption peaks are generated by the stretching vibration of methylene and its derivatives. Comprehensive analysis suggests that bitumen mainly contains alkanes, cycloalkanes, and aromatic compounds. In Fig. 3b, after aging, the absorbance of both SBS bitumen and CCR bitumen decreased compared with the original samples, with the reduction in the SBS bitumen absorbance being more significant. Among them, the aging SBS bitumen disappeared at a wave number of 966.5, while the aging CCR bitumen's wave peaks did not change significantly. It can be concluded that the polybutadiene and polystyrene of SBS bitumen are decomposed during aging, while there is no significant change in the CCR bitumen. These results indicate that the CCR bitumen has better anti-aging properties than the SBS bitumen. Figure 4 displays the infrared spectra of SBS and CCR bitumen prior to and following FTCs.

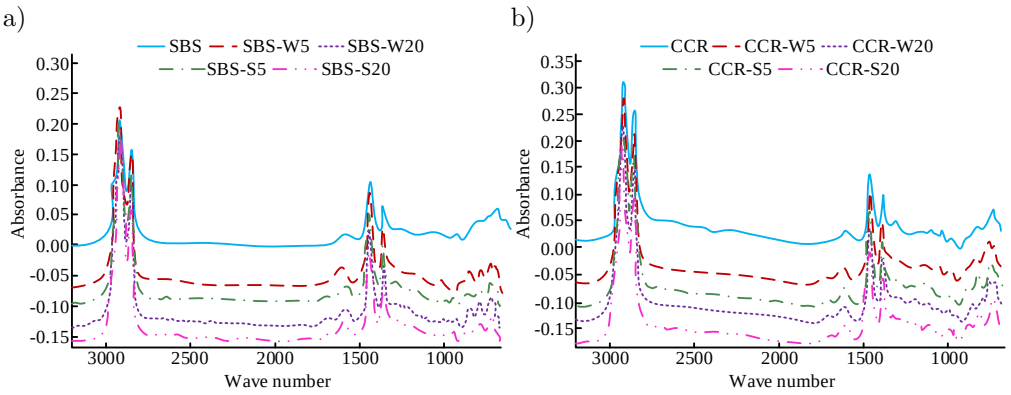

FIG. 4. Infrared spectra of bitumen before and after cyclic FTCs: a) SBS asphalt, b) CCR asphalt.

In Fig. 4a, the absorption peaks of the SBS bitumen at wave numbers of 1599.7 and 1694.6 changed significantly after FTC. This indicates that the aromatic hydrocarbon components of the SBS bitumen changed after FTC. Moreover, both cycloalkanes and unsaturated chains are oxidized, resulting in water-induced aging of the bitumen. In Fig. 4b, the infrared spectral changes of the CCR bitumen after FTC are basically the same as those of SBS bitumen, but the magnitude of change is smaller. This indicates that, compared with the SBS bitumen, the CCR bitumen has better freeze-thaw (FT) resistance. The functional group indices before and after FTC are shown in Fig. 5.

In Fig. 5a, the hydroxyl index of both SBS bitumen and CCR bitumen increased significantly after FTCs. Among them, the hydroxyl index of SBS bitumen is basically above 0.013, while that of CCR bitumen is in the range of 0.010 to 0.012. It can be concluded that the hydroxyl functional group changes

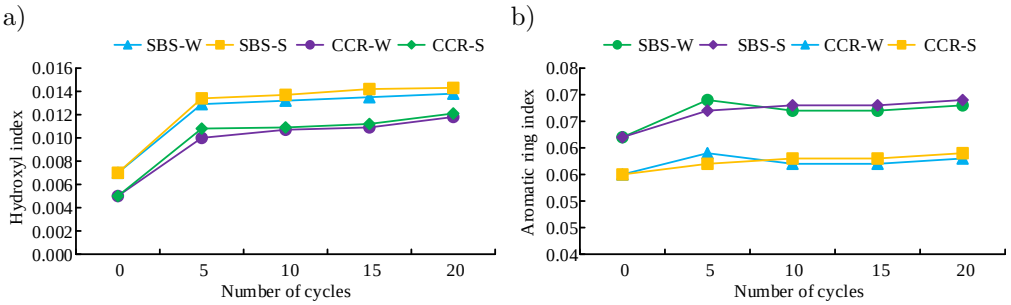

Fig. 5. Functional group indices before and after cyclic FTCs:
a) hydroxyl index, b) aromatic ring index.

of CCR bitumen after FTCs are small. In Fig. 5b, the cycloaromatic index of both SBS bitumen and CCR bitumen also increased significantly after FTCs. Among them, the cycloaromatic indices of two SBS bitumen samples are above 0.065, while those of CCR bitumen are around 0.060. This reveals that FTC have less effect on the cycloaromatic functional groups of the CCR bitumen. In order to investigate the mechanism of changes in the rheological properties of composite-modified bitumen, the microstructure was analyzed using fluorescence microscopy, and the results are shown in Fig. 6.

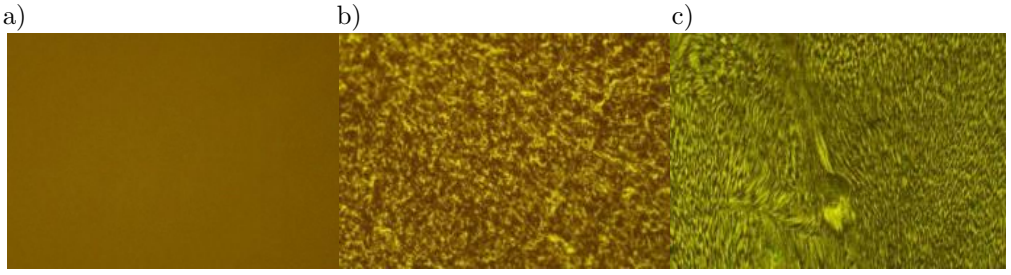

Fig. 6. Fluorescence microscope test results of modified bitumen:
a) matrix asphalt, b) SBS asphalt, c) CCR asphalt.

As shown in Fig. 6, the matrix bitumen appears as a homogeneous phase. SBS has a dense network structure, while SBS particles absorb light oil and expand, rapidly increasing in volume and gradually expanding and splitting, forming a visible network structure that envelops the bitumen in a grid-like structure. However, due to the poor stability of this structure, the modification effect of SBS bitumen is relatively moderate. In the CCR bitumen, rubber powder and SBS are dispersed in the bitumen, and SBS particles serve as anchor points interwoven with the flocculated rubber powder. Together, they form a relatively stable spatial structure, dispersed in the bitumen through coupling, which improves the rheological properties of the bitumen.

3.2. Adhesion characterization of composite MA

To investigate the adhesion properties of MA, the study was conducted to test the contact angle and atomic force to understand the adhesion and the Derjaguin–Muller–Toporov (DMT) modulus of the bitumen. Figure 7 displays the test results of the bitumen contact angle.

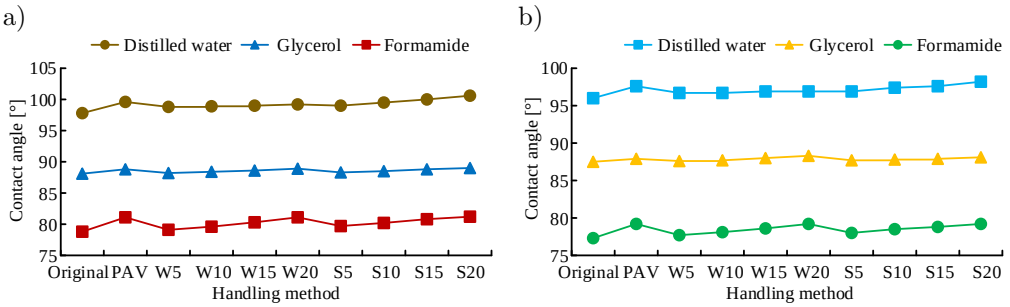

FIG. 7. Test results of the bitumen contact angle:
a) contact angle of SBS asphalt, b) contact angle of CCR asphalt.

In Fig. 7a, the contact angle of SBS bitumen after both aging and FTC is higher than that of the original sample. In the case of distilled water, for example, the contact angles with the original and aged samples are 97.8° and 99.6°, respectively. In Fig. 7b, the contact angles of CCR bitumen are all higher than those of the original samples. Similarly, in the case of distilled water, the contact angles with the original and aged samples are 96.0° and 97.6°, respectively. By comparing SBS-MA and CCR-MA, it is possible to determine that, under identical circumstances, the SBS bitumen has a wider contact angle than the CCR bitumen. With distilled water and ten FTC cycles as an example, the contact angles of SBS and CCR bitumen are 98.9° and 96.7°, respectively. According to the contact angle, the work of adhesion of bitumen can be calculated. Figure 8 presents the findings.

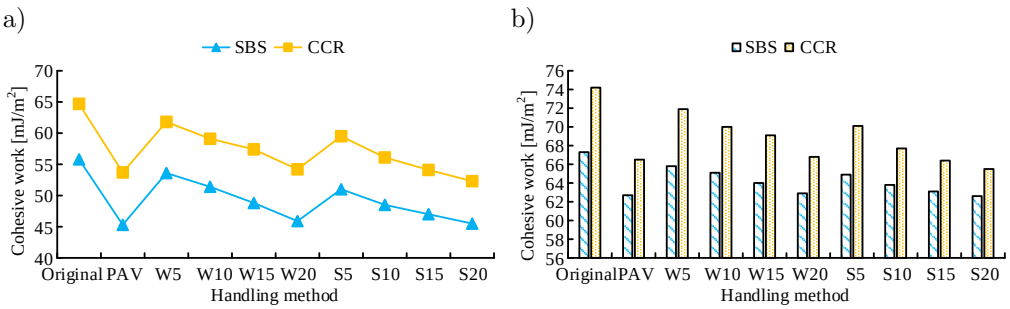

FIG. 8. Cohesion work of bitumen: a) asphalt, b) asphalt and aggregate.

In Fig. 8a, the work of cohesion for the CCR bitumen is higher than that of the SBS bitumen under the same conditions. For example, the cohesive polymerization function of SBS bitumen and CCR bitumen after five FTCs is 53.6 mJ/m^2 and 61.8 mJ/m^2, respectively. In Fig. 8b, the cohesive polymerization function between CCR bitumen and aggregate is higher than that of SBS bitumen under the same conditions. Taking the aged bitumen as an example, the work of adhesion between SBS bitumen and aggregate and between CCR bitumen and aggregate is 62.7 mJ/m^2 and 66.5 mJ/m^2, respectively. The microscopic adhesion and the DMT modulus of the bitumen are shown in Fig. 9.

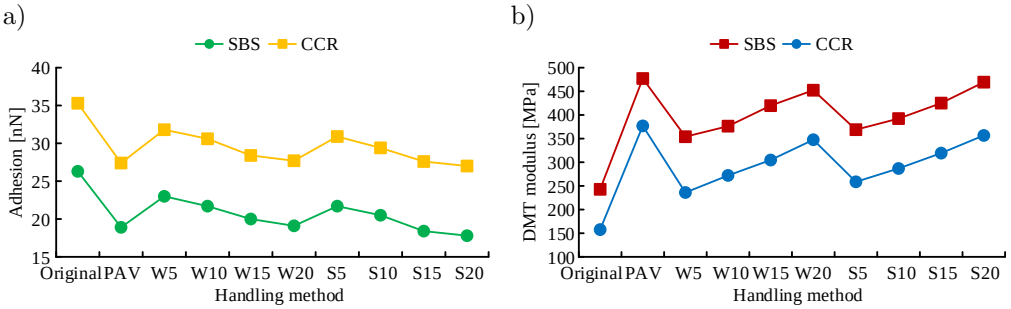

Fig. 9. Microscopic adhesion force (a) and DMT modulus (b) of bitumen.

In Fig. 9a, the adhesion force of bitumen is significantly reduced after treatment by either aging or FTC. In addition, the adhesion force of the CCR bitumen is greater under the same conditions. For example, the adhesion forces of SBS bitumen and CCR bitumen after aging are 18.9 nN and 27.4 nN, respectively. In Fig. 9b, the DMT modulus of the bitumen is significantly reduced after treatment by aging or FTC. Moreover, the DMT modulus of the CCR bitumen is smaller under the same conditions. For example, after five FTCs, the DMT moduli of SBS bitumen and CCR bitumen are 354.0 MPa and 236.0 MPa, respectively. These results indicate that the CCR bitumen has better cracking, aging and FT resistance. In order to investigate the mechanism of changes in CCR bitumen performance, the phase structure of the modified bitumen was analyzed using scanning electron microscopy, and the results are shown in Fig. 10.

As shown in Fig. 10, the surface of the matrix bitumen is smooth and free of impurities, with a linear morphology that is close to a homogeneous structure. In the SBS-modified bitumen, the SBS modifier is in a dispersed phase; however, due to the difficulty of forming a stable structural system between the SBS particles and the bitumen, the modification effect is relatively average. In the CCR-modified bitumen, the particle distribution of the modifier is denser, and a thicker gel-like substance is formed at the interface, which indicates that the rubber powder and SBS undergo sufficient vulcanization and swelling reactions

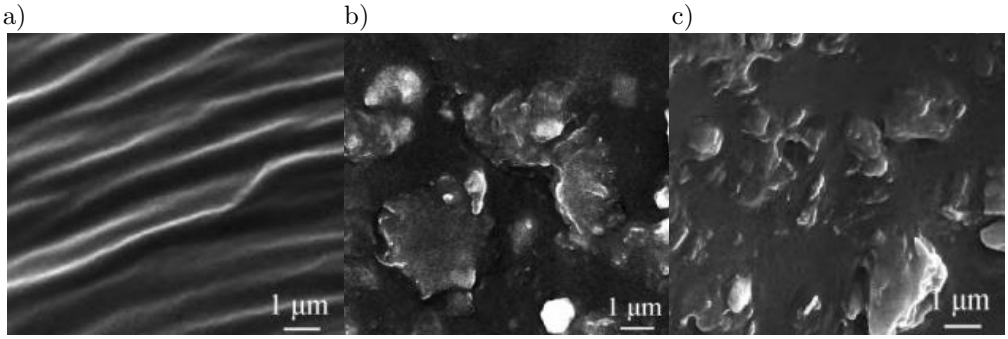

FIG. 10. Scanning electron microscope images:
a) matrix asphalt, b) SBS-MA, c) CCR-MA.

in the bitumen. This enhances the tensile deformation resistance and elastic recovery ability of the bitumen under external force.

3.3. LT cracking characterization of composite MA *mixes*

The study used both TPBTs and CSTS tests to evaluate the LT cracking properties of MA mixes. The results of the restrained specimen temperature stress test are shown in Fig. 11.

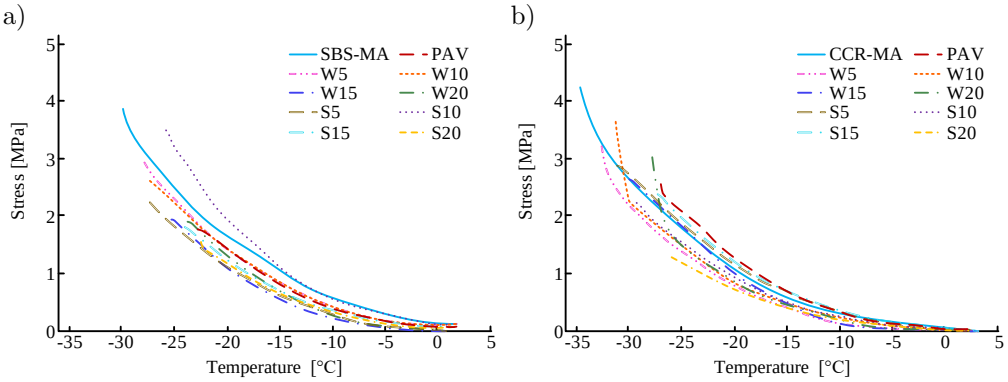

FIG. 11. Results of the temperature stress test on restrained specimens for:
a) SBS-MA, b) CCR-MA.

In Fig. 11a, the freeze-off temperatures of AMs after aging and FTC are significantly higher compared with those of the original SBS-AMs. The FT temperatures of SBS-MA mixture (SBS-MA), SBS-MA-PAV, and SBS-MA-W5 are −30 °C, −22.5 °C, and −27.7 °C, respectively. In Fig. 11b, the freeze-off temperatures of CCR-AMs are also significantly increased after aging and FTC. The FT temperatures of CCR-MA mixture (CCR-MA), CCR-MA-PAV and CCR-MA-W5 are −34.3 °C, −27.1 °C, and −32.5 °C, respectively, which are lower than

those of SBS-AMs. The aforementioned findings suggest that the CCR bitumen better resists LT cracking. Figure 12 displays the TPBT results of the beams.

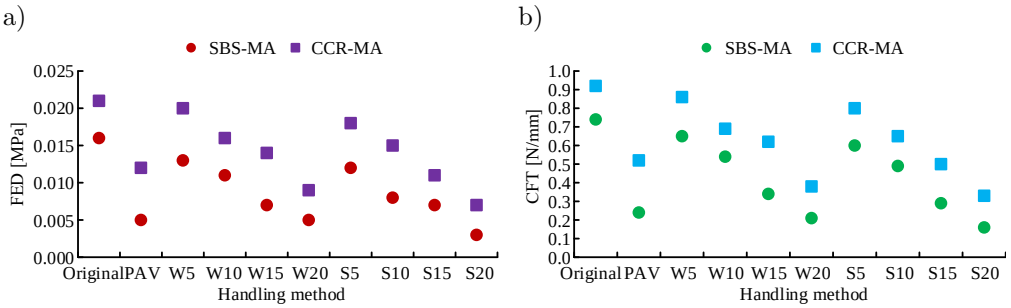

Fig. 12. TPBT results of small beams: a) FED, b) critical fracture toughness (CFT).

In Fig. 12a, the FEDs of AMs are significantly reduced after both aging and FTC. However, the FED of CCR-AMs is higher than that of SBS-AMs. For example, the FEDs of SBS-MA-PAV and CCR-PAV are 0.005 MPa and 0.012 MPa, respectively. In Fig. 12b, the CFT of AMs is significantly reduced after both aging and FTC. However, the CFT of CCR-AMs is higher under the same conditions. For example, the CFTs of SBS-MA-PAV and CCR-PAV are 0.24 N/mm and 0.52 N/mm, respectively. These results indicate that CCR bitumen has better toughness and cracking resistance. The study statistically analyzes the FED and CFT in order to understand the sensitivity of these parameters to each of the influencing factors. The sensitivities of the influencing factors are shown in Table 3.

Table 3. Sensitivity of influencing factors.

Influence factor	Index	Coefficient of variation [%]
Preburning	Fracture energy density	0.42
	Critical fracture toughness	0.39
FTC	Fracture energy density	0.37
	Critical fracture toughness	0.36
FT type	Fracture energy density	0.09
	Critical fracture toughness	0.07
Types of bitumen	Fracture energy density	0.27
	Critical fracture toughness	0.22

In Table 3, both FED and CFT are most sensitive to aging, with coefficients of variation (COVs) of 0.42 and 0.39, respectively. The next most sensitive factor is the number of FT cycles, with COVs of 0.37 and 0.36, respectively. In addition,

both FED and CFT are least sensitive to FT type, with COVs of 0.09 and 0.07, respectively. The results of the rutting test are shown in Fig. 13.

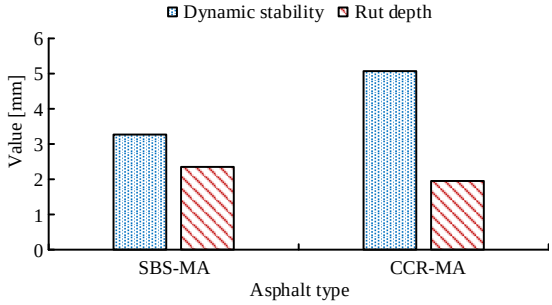

FIG. 13. Track test results.

As shown in Fig. 13, compared to SBS-MA, CCR-MA has greater dynamic stability and smaller rut depth. The dynamic stability of SBS-MA and CCR-MA is 3.27 times/mm and 5.07 times/mm, respectively, and the rut depths are 2.35 mm and 1.94 mm, respectively. These results indicate that the rubber-powder composite SBS can effectively improve the deformation resistance of bitumen materials. In terms of economic benefits, although SBS-modified bitumen has good road performance, its high cost limits its large-scale application. CCR composite-modified bitumen can reduce the amount of SBS modifier while maintaining bitumen performance by adding rubber powder, thus lowering production costs.

4. Discussion

A composite MA-CCR bitumen based on crumb rubber and an SBS modifier was created, and its rheological characteristics and LT cracking capabilities were examined in order to extend the life of AP and lower the likelihood of its cracking under LT conditions. The experimental results indicated that both SBS bitumen and CCR bitumen exhibited a significant increase in the stiffness modulus after aging and FTC. Furthermore, as the temperature dropped, the stiffness modulus rose. However, compared to SBS bitumen, the stiffness modulus of CCR bitumen under the same conditions was smaller.

Taking the aged bitumen as an example, the stiffness modulus of SBS bitumen and CCR bitumen at −24 °C was 949 MPa and 412 MPa, respectively. Furthermore, the change in the CR of CCR bitumen was negligible in comparison to that of SBS bitumen. Using aged bitumen as an example, the CR values at −12 °C were 0.37 and 0.44 for SBS and CCR bitumen, respectively. This suggests that the CCR bitumen has a higher capability for strain relaxation compared to the SBS bitumen.

Compared to the MA based on nano ZnO and SBS proposed by Li *et al.* [15], the MA with CCR exhibited better FTC resistance and creep performance. Specifically, the creep performance of the MA based on nano ZnO and SBS was improved by about 5 % compared to that of the SBS MA, whereas the creep performance of CCR-MA improved by about 19 % compared with the SBS bitumen. This improvement was due to the mixing and solubilization between the SBS modifier, crumb rubber modifier, and bitumen, which resulted in a physical cross-linking structure [16, 17].

An investigation of the infrared spectra of various bitumen was carried out in order to better understand the mechanism underlying the changes in MA properties. The outcomes indicated that SBS bitumen and CCR bitumen mainly contained alkanes, cycloalkanes and aromatic compounds. After aging, the absorbance of both SBS bitumen and CCR bitumen decreased compared with the original samples, with the decrease in SBS bitumen absorbance being more pronounced. Specifically, the wave peak of aged SBS bitumen disappeared at a wave number of 966.5, while the wave peak of aged CCR bitumen did not change significantly. It can be concluded that the polybutadiene and polystyrene in aged SBS bitumen were decomposed. This led to an increase in the content of hydroxyl, aromatic ring, and sulfinyl groups, which weakened its LT performance, while there was no significant change in CCR bitumen. After FTC, the aromatic hydrocarbon fractions of both SBS and CCR bitumen changed. Moreover, both the cycloalkanes and unsaturated chains were oxidized, which caused water aging of the bitumen; the degree of water aging of CCR bitumen was smaller [18].

In addition, fluorescence microscopy results showed that, compared to the SBS-modified bitumen, in the CCR-modified bitumen, SBS particles serve as anchor points interwoven with flocculated rubber powder, and the two form a relatively stable spatial structure dispersed in bitumen through coupling, thereby improving the rheological properties of the bitumen. At the same time, scanning electron microscopy revealed that in the CCR-modified bitumen, the particle distribution of modifier was denser, and a thicker gel-like material was formed at the interface. This indicates that the rubber powder and SBS undergo sufficient vulcanization and swelling reactions in bitumen, enhancing the tensile deformation resistance and elastic recovery ability of the bitumen under external forces.

To investigate the adhesion properties of the MA and the LT characteristics of its mixtures, the study conducted contact angle and atomic force tests, as well as CSTS tests and TPBTs. The findings showed that the cohesion function of the MA was reduced after both aging and FTC; however, under the same conditions, the cohesion function of CCR bitumen was higher than that of SSB bitumen. For example, the cohesive polymerization function of SSB bitumen and CCR bitumen after five water FTCs was 53.6 $\mathrm{mJ/m^2}$ and 61.8 $\mathrm{mJ/m^2}$, respectively.

Meanwhile, the DMT modulus of bitumen was significantly reduced after aging or FTC treatment. Moreover, the DMT modulus of CCR bitumen was smaller under the same conditions. Taking five water FTCs as an example, the DMT modulus of SBS bitumen and CCR bitumen was 354.0 MPa and 236.0 MPa, respectively. This is because aging and FTC would convert viscous components of bitumen into elastic components, leading to reduction of its deformation ability. SBS and crumb rubber in CCR bitumen reduce the effects of temperature, water, salts, and other factors on the viscous component, so the CCR bitumen exhibits better deformation capacity [19, 20].

Through comparison with Yang *et al.* [21], it can be observed that after FTC, there was a noticeable increase in surface cracking in bitumen cold-recycled mixtures, along with an increase in the width and number of main cracks. In addition, this observation is supported by the progressive decrease in the fatigue life (number of cycles) at the full-field maximum horizontal strain and the notable increase in the average volume of air voids and intermediate voids. Similarly, the results of Wang *et al.* [22] also demonstrated that after FTC, the mechanical properties of AMs were greatly reduced and key particles in the AM structure were significantly displaced.

The FED and CFT of the AMs decreased significantly after aging and FTC, while the freeze-fracture temperature increased significantly. This was due to the fact that aging increased the polar components in the bitumen, making it more prone to fracture. Meanwhile, freezing pressure generated by freezing and thawing increased the porosity of AMs, allowing liquids to enter the pore interior. Additionally, upon thawing, positive pressure occurred, which consequently caused the AM's strength to decrease. In terms of LT cracking, CCR-AMs outperformed SBS-AMs. This is attributed to CCR-AMs' superior ability to release stress in the form of deformation, and the higher energy required for crack propagation.

5. Conclusion

This study proposed a composite MA based on SBS and crumb rubber to improve the frost resistance of APs, and evaluated the MA's performance. The results showed that after LTA and water/salt FTCs, the CR of the MA decreased. Among these, the CR of aged bitumen was reduced most significantly, by at least 10.9 %. In addition, the CR of the MA decreased with decreasing temperature. However, compared with the SBS bitumen, the change in the CR of the CCR bitumen was relatively small. Taking the bitumen after the aging treatment as an example, the CR of SBS bitumen and CCR bitumen at −12 °C was 0.37 and 0.44, respectively.

In addition, the freeze-off temperatures of AMs after aging and FTC increased significantly, but the freeze-off temperature of CCR-AMs was always higher than that of SBS-AMs. For example, the freeze-off temperatures of SBS-MA-W5 and CCR-MA-W5 were $-27.7\,^{\circ}\mathrm{C}$ and $-32.5\,^{\circ}\mathrm{C}$, respectively. These results indicate that CCR bitumen has good rheological properties and excellent LT cracking resistance.

CCR composite-modified bitumen can be applied in highway pavement construction to improve road durability and service life due to its excellent HT stability and LT crack resistance. At the same time, the composite-modified bitumen can also be used for waterproof and anti-corrosion coatings on breakwaters and piers to resist seawater erosion.

The current study only analyzed the performance of CCR bitumen with a single SBS and rubber powder content, which limits the comprehensiveness of the research results. Future research will expand to CCR bitumen with different doping levels, systematically analyzing the effects of different proportions of rubber powder and SBS on bitumen performance to determine the optimal mixing ratio. This will help optimize the mechanical properties and durability of bitumen while reducing costs and providing a scientific basis for the widespread application of bitumen pavements.

Fundings

The research was supported by National Natural Science Foundation of China, 'Decaying prediction of aging performance of hot recycled asphalt and mixture under exposure situation in Northwest, China' (no. 52268070), and Research project of Gansu Provincial Department of Transportation, 'Evaluation and application of aging resistance of thermal reclaimed bitumen pavement in Gansu Province' (no. 2023-02).

Conflicting interest

The authors declare that they have no known competing financial interests or personal relationships that could have appeared to influence the work reported in this paper.

Authors' contributions

All authors contributed equally to this work, reviewed, and approved the final manuscript.

References

1. Kumar Y., Kumar P., Ravindranath S.S., Evaluating the intermediate temperature properties of SB modified asphalt binders: Influence of SB copolymer structure,

International Journal of Pavement Research and Technology, **17**(4): 1014–1031, 2024, https://doi.org/10.1007/s42947-023-00283-1.

2. Wei Z., Zhao Z., Hui C., Junjie X., Huaxin X., Dongyu N., High temperature rheological properties of surface pretreated PVA fiber modified asphalt [in Chinese], *Journal of Shenzhen University Science and Engineering*, **39**(4): 409–416, 2022, https://doi.org/10.3724/sp.j.1249.2022.04409.

3. Rahman M.N., Sarkar M.T.A., Elseifi M.A., Mayeux C., Cooper S.B., Free K., Short-term field performance and cost-effectiveness of crumb-rubber modified asphalt emulsion in chip seal applications, *Transportation Research Record*, **2675**(9): 1049–1062, 2021, https://doi.org/10.1177/03611981211005469.

4. Elmoghazy Y., Abuelgasim E.M.O., Osman S.A., Afaneh Y.R.H., Eissa O.M.A., Safaei B., Effective mechanical properties evaluation of unidirectional and bidirectional composites using virtual domain approach at microscale, *Archives of Advanced Engineering Science*, **1**(1): 27–37, 2023, https://doi.org/10.47852/bonviewAAES32021723.

5. Liu B., Li X., Li S., Pavement performance analysis of carbon nanotube/SBS composite modified asphalt, *Carbon Letters*, **34**(1): 343–350, 2024, https://doi.org/10.1007/s42823-023-00605-0.

6. Ting J.H., Khare E., DeBellis A., Orr B., Jourdan J.S., Martín-Martínez F.J., Jin K., Malonson B.L., Buehler M.J., Role of methylene diphenyl diisocyanate (MDI) additives on SBS-modified asphalt with improved thermal stability and mechanical performance, *Energy & Fuels*, **35**(21): 17629–17641, 2021, https://doi.org/10.1021/acs.energyfuels.1c02794.

7. Duarte Mendonça A.M.G., Melo Neto O. de M., Rodrigues J.K.G., Batista de Lima R.K., Silva I.M., Marques A.T., Characterisation of modified asphalt mixtures with lignin of *pinus* and *eucalyptus* woods, *Australian Journal of Civil Engineering*, **21**(2): 253–264, 2023, https://doi.org/10.1080/14488353.2022.2089376.

8. Li H., Sun J., Wang S., Zhang M., Hu Y., Sheng Y., Bamboo fiber modified asphalt mixture proportion design and road performances based on response surface method, *Journal of Wuhan University of Technology-Materials Science Edition*, **38**(1): 156–170, 2023, https://doi.org/10.1007/s11595-023-2678-8.

9. Amini N., Hayati P., Latifi H., Evaluation of rutting and fatigue behavior of modified asphalt binders with nanocomposite phase change materials, *International Journal of Pavement Research and Technology*, **16**(3): 678–692, 2023, https://doi.org/10.1007/s42947-022-00156-z.

10. Chen S., Wang Y., He X., Su Y., Pan Y., Cao Y., Wang W., Yang C., Jiang B., Zhang S., Viscous flow activation energy and short-term aging resistance of SBS-modified asphalt enhanced by PPA oil-grinding activated MoS_2, *Fluid Dynamics and Materials Processing*, **21**(2): 387–404, 2025, https://doi.org/10.32604/fdmp.2024.055697.

11. Li C., Ma F., Fu Z., Dai J., Wen Y., Wang Y., Rheological behavior of polyphosphoric acid-vulcanized liquid rubber compound modified asphalt binder, *Iranian Journal of Science and Technology, Transactions of Civil Engineering*, **46**(5): 3931–3945, 2022, https://doi.org/10.1007/s40996-022-00831-y.

12. Song W., Study on the high and low temperature performance of nano alumina modified asphalt mixture, *International Journal of Microstructure and Materials Properties*, **16**(4): 229–238, 2022, https://doi.org/10.1504/IJMMP.2023.128421.

13. Enieb M., Cengizhan A., Karahancer S., Eltwati A., Evaluation of physical-rheological properties of nano titanium dioxide modified asphalt binder and rutting resistance of modified mixture, *International Journal of Pavement Research and Technology*, **16**(2): 285–303, 2022, https://doi.org/10.1007/s42947-021-00131-0.

14. Habbouche J., Piratheepan M., Hajj E.Y., Bista S., Sebaaly P.E., Full-scale pavement testing of a high polymer-modified asphalt concrete mixture, *Journal of Testing and Evaluation*, **50**(2): 865–888, 2022, https://doi.org/10.1520/JTE20210283.

15. Li X., Shen J., Dai Z., Ling T., Li X., Comprehensive performances of hybrid-modified asphalt mixtures with nano-ZnO and styrene-butadiene-styrene (SBS) modifiers, *The Baltic Journal of Road and Bridge Engineering*, **17**(3): 170–186, 2022, https://doi.org/10.7250/bjrbe.2022-17.574.

16. Hao H., Chen Z., Cong P., Han Z., Rheological, chemical and short-term aging properties of waste polyurethane particles modified asphalt binder with or without SBS, *Construction and Building Materials*, **357**: 129363, 2022, https://doi.org/10.1016/j.conbuildmat.2022.129363.

17. Zeng J., Zhao J., Mechanism and performance investigation of SBS/sulfur composite modified asphalt, *Petroleum Chemistry*, **62**(7): 732–739, 2022, https://doi.org/10.1134/S0965544122050140.

18. Otto C.G., Awarri A.W., Comparative cost-effectiveness of modified asphalt concrete submerged in moisture as related to fatigue performance, *IOSR Journal of Mechanical and Civil Engineering*, **18**(2): 49–54, 2021.

19. Tiza M., Duweni C., Mogbo O., Terlumun S., Asawa J., Characterization of reclaimed asphalt pavement and optimization in polymer modified asphalt blends: A review, *Civil Engineering Beyond Limits*, **2**(2): 27–34, 2021, https://doi.org/10.36937/cebel.2021.002.004.

20. Cong P., Guo X., Mei L., Zhang Y., Influences of aging on the properties of SBS-modified asphalt binder with anti-aging agents, *Iranian Journal of Science and Technology, Transactions of Civil Engineering*, **46**(2): 1571–1588, 2021, https://doi.org/10.1007/s40996-021-00650-7.

21. Yang Y., Yue L., Yang Y., Chen Y.Y., Multi-scale decay mechanism of emulsified asphalt cold recycled mixture under freeze-thaw, *The Baltic Journal of Road and Bridge Engineering*, **18**(3): 50–69, 2023, https://doi.org/10.7250/bjrbe.2023-18.608.

22. Wang N., Zhang H., Xiong H., Microstructure and mechanical behavior of asphalt mixture based on freeze-thaw cycle, *Multidiscipline Modeling in Materials and Structures*, **17**(4): 760–774, 2021, https://doi.org/10.1108/MMMS-10-2020-0262.

Received April 27, 2025; revised July 7, 2025; accepted July 11, 2025; available online December 18, 2025; version of record March 17, 2026; published issue March 30, 2026.

Engineering Transactions, **74**(1): 39–50, 2026, https://doi.org/10.24423/engtrans.2026.3531
Institute of Fundamental Technological Research Polish Academy of Sciences (IPPT PAN)
Université de Lorraine • Poznan University of Technology

Research Paper

Self-Supporting Arch Halls – Design Methods

Ryszard Walentyński[1)], Robert Cybulski[2)], Henryk Myrcik[1)*]

[1)] *Faculty of Civil Engineering, Silesian University of Technology*
Gliwice, Poland

[2)] *MERAENG Sp. z o.o. sp.k.*
Siemianowice Śląskie, Poland

*Corresponding Author: Henryk.Myrcik@polsl.pl

Self-supporting arch halls are increasingly used in the construction of buildings with a significant impact on public safety. Unfortunately, no specific design methodology has yet been established. Even more concerning is the growing emergence of new design challenges, including local structural modifications and unconventional loading conditions. This study reviews methods applied in engineering practice as well as those proposed in research studies. A comparative analysis of results obtained using various methods is presented for selected structures subjected to loads according to applicable standards.

Keywords: UBM, K-span, thin-walled panels, arch structures.

1. Introduction

Self-supporting arch halls made of doubly corrugated thin-walled steel profiles are becoming increasingly popular in the Polish and European markets. An analysis of recent projects completed by system providers, as presented in [1], indicates that the most commonly constructed buildings in our region are sports halls and agricultural structures, including warehouses, livestock buildings, and shelters. Examples of projects completed in 2024 by the World Technology Group [2] using the ultimate building machine (UBM), as described in [3], are presented in Fig. 1 and Fig. 2. Both agricultural and sports facilities often require local structural modifications to meet their functional requirements. In sports halls, skylights (Fig. 3) and ventilation openings are commonly introduced. In agricultural buildings, suspended conveyors, screw carriers, or other equipment are frequently installed. The impact of such local modifications on global structural behavior is typically not considered during the design process. A probable

Fig. 1. Arch hall in Białystok, Poland.

Fig. 2. Arch hall in Łomża, Poland.

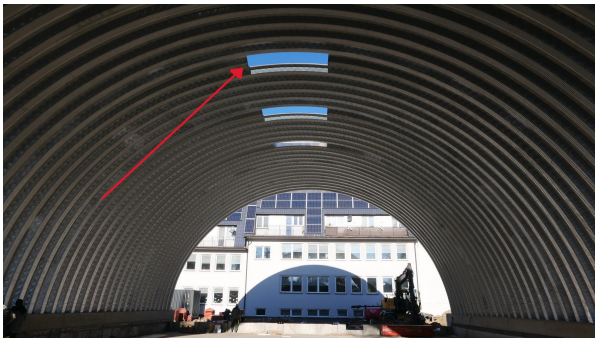

Fig. 3. Skylights in sports halls.

reason for omitting the influence of these modifications on structural behavior is the lack of a dedicated design methodology, as previously discussed in various studies, such as [4–6].

2. Purpose and scope of work

The aim of this study is to present and compare selected design methods for this type of structure, currently used by engineers or proposed by researchers. A literature review and an analysis of structural design approaches in this field appear necessary, considering the number of structures currently being built, the consequences of structural failures, and the noticeable variation in design

approaches observed by the authors. Systematizing knowledge of the fundamental behavior of self-supporting arch halls will provide a foundation for further research on the impact of local modifications on overall structural performance.

3. Review of design methods

The selected design methods are presented further. Both methods used in engineering practice (simplified methods) and those proposed in scientific research (advanced methods) are described. Based on the authors' own research and the conclusions of many researchers (e.g., [7]), it should be emphasized that such structures require the use of second-order theory because they exhibit strong nonlinearity.

3.1. Simplified methods

Based on an analysis of projects involving single-shell structures, it has been determined that two primary methods are predominantly used. These methods are classified as simplified due to their lower level of complexity compared to the approaches recommended by researchers specializing in this type of structure. Simplified methods include:

- method no. 1: based on a 1D linear analysis of a single isolated profile and an evaluation of its capacity utilisation factor according to the provisions of the Eurocode standards [8–10]. The cross-section of the profile is analyzed without transverse corrugations and is most often classified as Class 4. The buckling length coefficient is assumed in accordance with Annex D of the standard [11];
- method no. 2: commonly used in everyday design practice is based on a geometrically nonlinear 1D analysis performed for a single profile, with transverse corrugations omitted, similarly to the first method. The shape of the arch is deformed by introducing imperfections defined in Annex D of [11]. Following [14], the utilisation factor for capacity assessment is determined at the cross-sectional level, without considering the global buckling factor of the arch.

3.2. Advanced methods

Methods proposed by numerous researchers are classified as advanced because they exhibit a higher level of complexity compared to those used in everyday engineering practice. Advanced methods include:

- method no. 3: a design approach proposed in [7], based on 1D models with variable stiffness, which is the result of local buckling of the compressed

cross-sectional webs. The necessity of considering additional bending moments arising from the shift in the center of gravity was also highlighted;

– method no. 4: based on the finite element analysis of shells and takes into account the influence of deformations on the distribution of internal forces. This approach has been proposed by many researchers, including [18, 19];
– method no. 5: described in the monograph [20], based on a 1D model represented by a single profile, characterized by variable axial and bending stiffness depending on the bend radius and stress level. The stiffness values are determined using proposed formulas that account for normal forces, bending moments, and the failure force acting at the centroid of the cross-section. Determining these stiffness values requires laboratory-scale tests or numerical analyses of small-scale shell models. This method has been validated against shell models and laboratory tests, demonstrating a high degree of result convergence.

4. Discussion

The use of method no. 1 raises doubts for the following reasons. In [12], it was shown that ignoring transverse corrugations can lead to a significant overestimation of the load-bearing capacity of the element. The buckling length coefficients given in [10] most frequently do not correspond to the cases considered, especially in relation to UBM technology, which is becoming increasingly popular due to the possibility of introducing a variable bending radius of the arch. Furthermore, in [7], it was observed that the buckling length coefficient should be determined while considering the variable stiffness of the arch. When designing in accordance with this approach, the additional stresses in the structure resulting from changes in its geometry under load are not considered [13].

In relation to the assumptions of method no. 2, based on the results shown in [15], self-conducted measurements of actual imperfections were conducted on structures with shapes corresponding to those defined in [11]. The measurements were carried out after the arches were installed, before additional loads and under wind-free conditions, using a Leica 3D Disto laser rangefinder [16]. The results indicate significantly greater deformations in the real structures than those assumed in the standard [10]. The in-plane measurements of the arch are illustrated in Fig. 4 and Fig. 5, while the out-of-plane ones are illustrated in Fig. 6. The results are presented as follows: line (1) represents the theoretical arch shape; line (2) represents the curve derived from imperfections according to [11] and static calculations under self-weight; and line (3) represents the curve obtained from actual measurements. The measurement results are provided for sections 1 to 5, which are located at 30-degree intervals. The displacements are measured relative to line 1 (red line – the theoretical shape without imperfec-

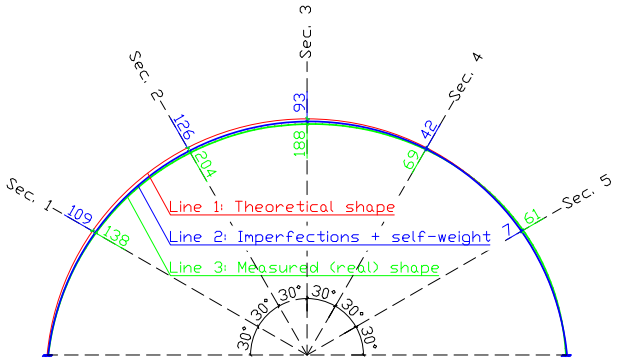

FIG. 4. Measurements of the shape of the first roof covering, with a span of 19 m.

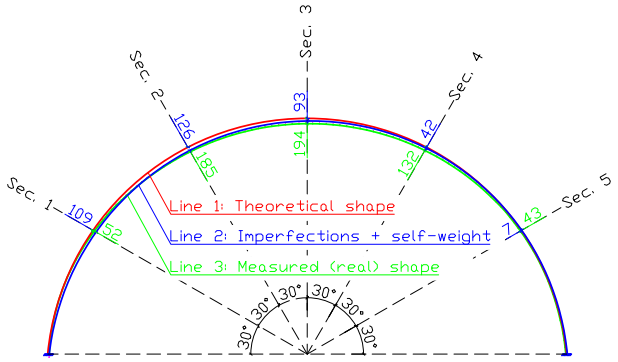

FIG. 5. Measurements of the shape of the second roof covering, with a span of 19 m.

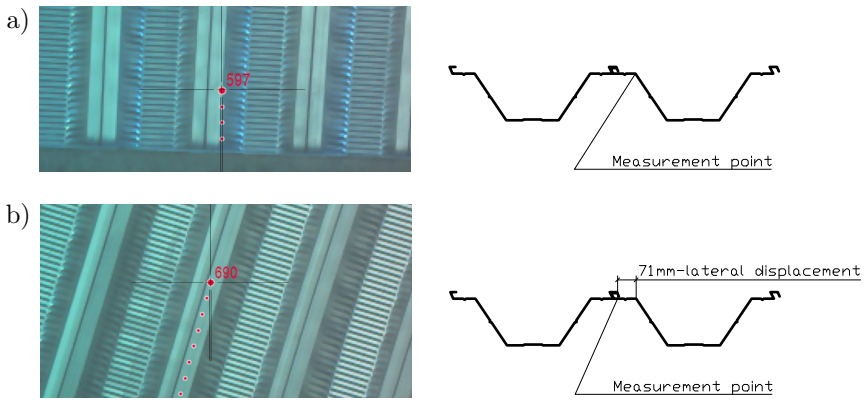

FIG. 6. Lateral displacements – measurement in the support zone (a) and ridge zone (b).

tions). Furthermore, the measurements revealed a tendency for profiles with larger spans ($L > 18$ m) to undergo lateral (out-of-plane) displacements in the ridge zone (the top zone – the highest part of the structure), as shown in Fig. 6.

The red points shown in Fig. 6 indicate the locations of successive measurements taken in the vertical plane. The red numbers in Fig. 6 correspond to the measurement point identifiers. As shown in Fig. 6, the maximum measured out-of-plane displacement of the panel is 71 mm. These findings highlight potential discrepancies between assumed and actual structural behavior, indicating that the imperfections prescribed in [11] may underestimate the real deformations that occur in self-supporting arch halls. Table 1 presents the measured imperfection values of the halls illustrated in Fig. 4, Fig. 5, and Fig. 6.

Table 1. Measurement of the shape of an arch-hall with a span of 19 m.

Analyzed structure	Location along the panel	Displacement in-plane [mm]		Displacement out-of-plane [mm]	
		Case 1*	Case 2**	Case 1*	Case 2**
Structure no. 1 according (acc.) to Fig. 4	Sec. 1 acc. to Fig. 4	109	138	0	27
	Sec. 2 acc. to Fig. 4	126	204	0	51
	Sec. 3 acc. to Fig. 4	93	188	0	71
	Sec. 4 acc. to Fig. 4	42	69	0	45
	Sec. 5 acc. to Fig. 4	7	−61	0	20
Structure no. 2 acc. to Fig. 5	Sec. 1 acc. to Fig. 5	109	52	0	15
	Sec. 2 acc. to Fig. 5	126	185	0	29
	Sec. 3 acc. to Fig. 5	93	194	0	42
	Sec. 4 acc. to Fig. 5	42	132	0	32
	Sec. 5 acc. to Fig. 5	7	43	0	19

*Case 1 refers to the comparison between the ideal shape (line 1 acc. to Fig. 4 and Fig. 5) and the deformed shape obtained from calculations after introducing imperfections and applying self-weight (line 2 acc. to Fig. 4 and Fig. 5).
**Case 2 refers to the comparison between the ideal shape (line 1 acc. to Fig. 4 and Fig. 5) and the actual shape obtained from measurements (line 3 acc. to Fig. 4 and Fig. 5).

With respect to advanced methods, method no. 3 does not provide a definition of the geometric characteristics for elements with transverse corrugations. As demonstrated in [17], these characteristics differ from those of elements with flat walls and additionally depend on the introduced bending radius. Method no. 4 may soon become the industry standard, given technological advancements and the increasing computational power of standard computers. However, the authors emphasize that further refinement is needed, particularly in defining the geometry of doubly corrugated profiles. Currently, panel geometry is most often defined based on 3D scans. This approach complicates comparative analyses, which structural designers frequently conduct during the design phase to select the most optimal solution. Moreover, it requires access to the analyzed profiles, which are not commonly available in most design offices.

Based on the authors' literature study, method no. 5 presented in [20], appears to be the most optimal approach given the current state of knowledge. Further study of this method is recommended for designers working with such structures.

5. Comparison of selected methods

Comparing the results obtained using conventional (simplified) methods with those of the suggested (advanced) methods is not a common practice, especially when the analyzed structure is subjected to loads defined by design standards. In [20], it was stated that engineering methods overestimated load capacity by 25 % and underestimated the deflection by more than three times. However, these results were obtained for a single case of symmetric load rather than for a combination of primarily asymmetric loads. The following section presents the results of the authors' own analyses. The first analysis concerns a structure with constant bending radius, the geometry of which is shown in Fig. 7, subjected to the loads illustrated in Fig. 8. Finishing materials assumed as $0.3\,\mathrm{kN/m^2}$. Wind loads were applied in accordance with standard [21] for the following assumptions: localization Poland, 1st wind zone, and 4th terrain category. Snow loads followed standard [22] for the following assumptions: localization Poland, and 2nd snow zone. The analyzed model is a 1D bar model with pinned supports and a cross-section of the UBM240 system, as shown in Fig. 9.

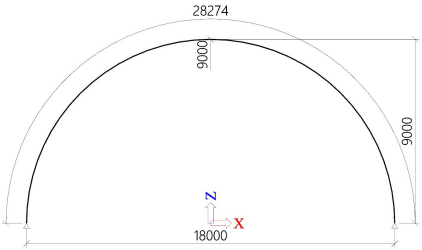

Fig. 7. Analyzed structure.

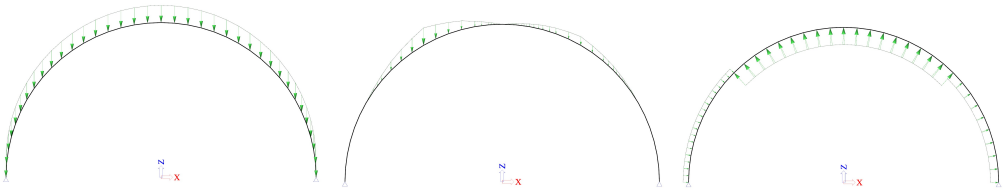

Load case 1:
Self-weigh and finishing material load

Load case 2:
Snow load

Load case 2:
Wind load

Fig. 8. Analyzed load cases.

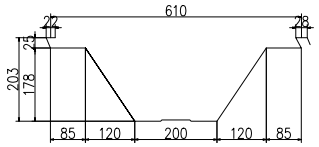

FIG. 9. Analyzed cross-section: UBM240 $t = 1.40$ mm, S320GD+Z.

Calculations were performed for load combinations according to standard [8], using the simplified methods (no. 1 and no. 2) described above, as well as method no. 5. Figure 10 illustrates the use of the arches' capacity. Table 2 provides a summary of the results.

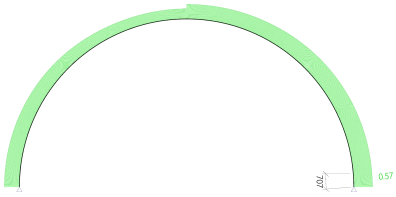

Method no.1
(simplified)

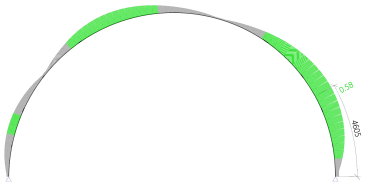

Method no. 2
(simplified)

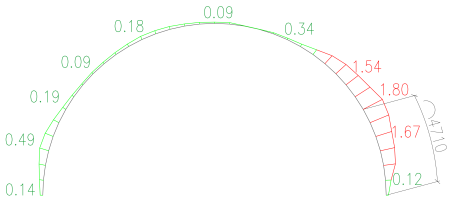

Method no. 5
(advanced)

FIG. 10. Results obtained – utilization of capacity for the load combination.

TABLE 2. Obtained results.

Design method	Obtained results					
	Displacement U_x		Displacement U_z		Utilization of capacity UC	
	Value [mm]	Section* [m/m]	Value [mm]	Section* [m/m]	Value [%]	Section* [m/m]
Method no. 1 (simplified)	81.4	6.67/28.27	48.8	17.32/28.27	57.0	0.71/28.27
Method no. 2 (simplified)	86.2	6.77/28.27	50.6	17.41/28.27	58.0	4.61/28.27
Method no. 5 (advanced)	560.8	5.93/28.27	304.7	16.93/28.27	180.0	4.71/28.27

*Section measured from the right support.

Due to the increasing popularity of self-supporting roofs with a variable bending radius, a second analysis was performed for a structure with the geometry shown in Fig. 11. An analogous approach to that in the first case was adopted. Figure 12 illustrates the loading method, while Fig. 13 presents the utilization of the arches' capacity. Table 3 provides a summary of the results.

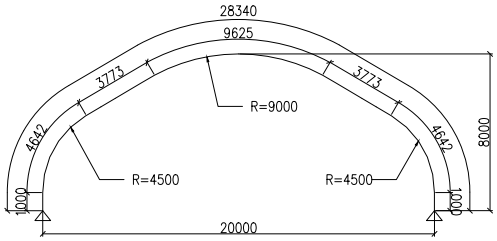

Fig. 11. Analyzed structure.

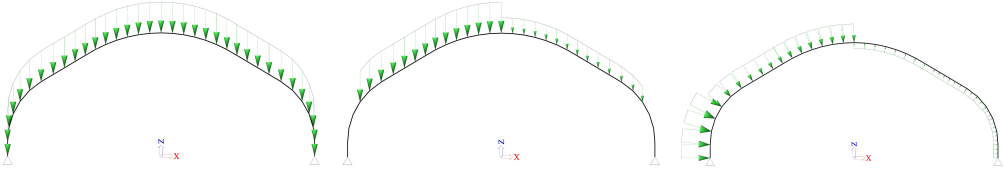

Load case 1:
Self-weigh and finishing material load

Load case 2:
Snow load

Load case 2:
Wind load

Fig. 12. Analyzed load cases.

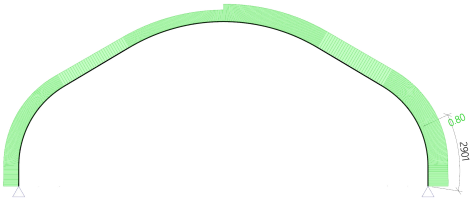

Method no.1
(simplified)

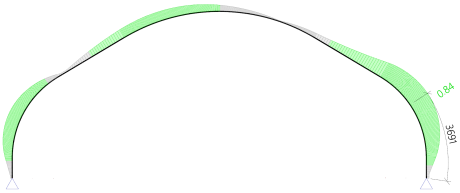

Method no. 2
(simplified)

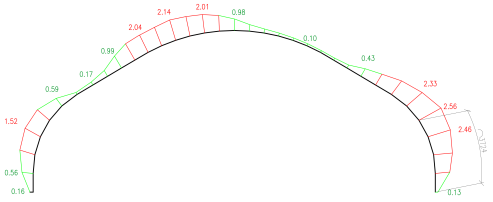

Method no. 5
(advanced)

Fig. 13. Results obtained – utilization of capacity for the load combination.

Table 3. Obtained results.

Design method	Obtained results					
	Displacement U_x		Displacement U_z		Utilization of capacity UC	
	Value [mm]	Section* [m/m]	Value [mm]	Section* [m/m]	Value [%]	Section* [m/m]
Method no. 1 (simplified)	73.6	5.30/28.34	64.6	16.77/28.34	80.0	2.90/28.34
Method no. 2 (simplified)	79.4	5.45/28.34	68.5	16.82/28.34	84.0	3.69/28.34
Method no. 5 (advanced)	710.1	3.97/28.34	589.7	15.19/28.34	256.0	3.72/28.34

*Section measured from the right support.

6. Summary

Designing self-supporting arch halls made of doubly corrugated thin-walled steel profiles based on inadequately adjusted methods can lead to a significant overestimation of load-bearing capacity and an underestimation of deflections. The discrepancy in the results essentially excludes the possibility of using simplified methods given the current state of knowledge. More research, focused on considering local modifications, real imperfections, and tendencies toward lateral displacements, seems necessary to be conducted.

Fundings

This research did not receive any specific grant from funding agencies in the public, commercial, or not-for-profit sectors.

Conflict of interest

The authors declare that there are no known competing financial interests or personal relationships that could influence the work reported in this document.

Authors' contributions

Ryszard Walentyński conceptualized the study and supervised the study. Robert Cybulski contributed to data interpretation and supervised the study. Henryk Myrcik performed the analysis and wrote the original draft. All authors reviewed and approved the final manuscript.

Acknowledgments

The article was prepared in relation to the presentation at the XXX LSCE Conference.

References

1. Myrcik H., Halls and arched structures for quick assembly – An overview of popular system solutions [in Polish: Hale i przekrycia łukowe szybkiego montażu – Przegląd popularnych rozwiązań systemowych], *Przegląd Budowlany*, **94**(9–10): 24–27, 2023, http://doi.org/10.5604/01.3001.0053.9357.
2. World Technology Group, https://wtgsa.eu/.
3. Walentyński R., Cybulski R., Myrcik H., Introduction to the Investigation of reproduction of the real geometry of UBM panels, *Bulletin of the Polish Academy of Sciences Technical Sciences*, **73**(1): e152214, 2025, http://doi.org/10.24425/bpasts.2024.152214.
4. Walentyński R., Cybulski R., Kozieł K., Numerical models of ABM K-span steel arch panels, *Architecture Civil Engineering Environment (ACEE)*, **4**: 105–114, 2011, https://www.researchgate.net/publication/235256959_Numerical_models_of_ABM_K-Span_steel_arch_panels.
5. Piekarczuk R., Więch P., Kuczyński K., Walentyński R., Experimental and computational approaches to the evaluation of double corrugated arch structures. A review of the latest advancements, *Archives of Civil Engineering*, **67**(2): 7–35, 2021, http://doi.org/10.24425/ace.2021.137152.
6. Seguin D., *Structural behaviour of thin-walled doubly-corrugated K-span structures with pinned and fixed base support conditions*, Ph.D. Thesis, Royal Military College of Canada, 2022.
7. Biegus A., Static and strength analysis of arched corrugated panels [in Polish: Analiza statyczno-wytrzymałościowa łukowych blach fałdowych], *Konstrukcje Stalowe*, **7**(65): 24–28, 2003, https://yadda.icm.edu.pl/baztech/element/bwmeta1.element.baztech-article-BTB2-0033-0088.
8. European Committee for Standardisation, EN 1990: Eurocode 0: Basis of structural design, 2002.
9. European Committee for Standardisation, EN 1993-1-1: Eurocode 3: Design of steel structures – Part 1–1: General rules and rules for buildings, 2005.
10. European Committee for Standardisation, EN 1993-1-3: Eurocode 3: Design of steel structures – Part 1–3: General rules – Supplementary rules for cold-formed members and sheeting, 2006.
11. European Committee for Standardisation, EN 1993-3-2: Eurocode 3: Design of steel structures – Part 3–2: Towers, masts, and chimneys – Chimneys, 2006.
12. Cybulski R., *Analysis of local stability of doubly corrugated thin-walled structures*, Ph.D. Thesis, Silesian University of Technology, 2015.
13. Biegus A., *Ultimate Load-Bearing Capacity of Steel Bar Structures* [in Polish: *Nośność Graniczna Stalowych Konstrukcji Prętowych*], PWN, Warszawa–Wrocław, 1997.
14. Stachura Z., Giżejowski M., Eurocode procedures for the stability verification of the load-bearing capacity of the plane steel frames [in Polish: Eurokodowe procedury stateczno-ściowego sprawdzania nośności stalowych ram płaskich], [in:] *Konstrukcje Betonowe i Metalowe,* Wydawnictwa Uczelniane Uniwersytetu Technologiczno-Przyrodniczego w Bydgoszczy, pp. 267–275, 2015.

15. Suchodoła M., The influence of geometric imperfections on the load-bearing capacity of steel arch panels [in Polish: Wpływ imperfekcji geometrycznych na nośność stalowych blach łukowych], *Zeszyty Naukowe Politechniki Śląskiej Seria: BUDOWNICTWO*, **1695**: 299–360, 2005.

16. Leica Geosystems, Leica 3D Disto, https://shop.leica-geosystems.com/sites/default/files/2020-05/847903_Leica_3D_Disto_UM_V.6-1-0_en.pdf?srsltid=AfmBOopeuEZK4R2_mfgKYgoTE2dG4XdJLAlm7ZHLbNdqmOhSo2mXJ3mE (access: 23.06.2025).

17. Walentyński R., Cybulski R., Kozieł K., Local buckling and post-buckling investigation of cold-formed self-supported elements, [in:] *20th International Conference on Computer Methods in Mechanics*, pp. 23–37, 2013.

18. Anghel V., Sorohan S., Constantin N., Stoica I., On the analysis of a cold formed steel profile arch structure, *Acta Electrotehnica*, **57**(1–2): 99–104, 2016.

19. Cybulski R., Walentyński R., Cybulska M., Local buckling of cold formed elements used in arched building with geometrical imperfections, *Journal of Constructional Steel Research*, **96**: 1–13, 2014, http://doi.org/10.1016/j.jcsr.2014.01.004.

20. Piekarczuk A., *Experimental and Computational Methods for the Evaluation of Arched Roofs Made of Double-Corrugated Panels* [in Polish: *Doświadczalne i Obliczeniowe Metody Oceny Łukowych Przekryć z Blach Podwójnie Giętych*], Instytut Techniki Budowlanej, 2018.

21. European Committee for Standardisation, EN 1991-1-3: Eurocode 1: Actions on structures – Part 1–3: General actions – Snow loads, 2003.

22. European Committee for Standardisation, EN 1991-1-4: Eurocode 1: Actions on structures – Part 1–4: General actions – Wind actions, 2005.

Received February 27, 2025; revised June 23, 2025; accepted August 1, 2025; available online January 14, 2026; version of record March 10, 2026; published issue March 30, 2026.

Engineering Transactions, **74**(1): 51–67, 2026, https://doi.org/10.24423/engtrans.2026.3584
Institute of Fundamental Technological Research Polish Academy of Sciences (IPPT PAN)
Université de Lorraine • Poznan University of Technology

Research Paper

Graphical Method for Synthesizing a Four-Bar Linkage with Specified Coupler Angular Reversal Positions

Jacek Buśkiewicz

Poznan University of Technology
Poznań, Poland

e-mail: jacek.buskiewicz@put.poznan.pl

Graphical methods remain an important tool in the theory of mechanisms due to their ability to visually convey fundamental kinematic principles. They are particularly useful in the early design stages and in educational contexts, where intuitive understanding is essential. Among the applications of graphical synthesis methods, mechanisms that require a link to momentarily stop at specific angular positions – commonly referred to as angular reversal positions – are of particular interest. While various analytical and numerical methods exist for designing such mechanisms, they typically focus on dwell positions of rotational or translational links and rely on optimization techniques, often at the cost of geometric transparency. This paper presents a graphical synthesis method for a four-bar linkage designed to achieve two prescribed positions at which the coupler reverses its direction of rotation. This specific problem has not been previously addressed in the literature. It arises in mechanisms used for emptying containers, where the coupler carries the container and must instantaneously pause at two distinct angular positions to ensure stable discharge. Unlike many graphical methods, which may involve ambiguity due to trial-and-error selection of geometric parameters, the proposed technique ensures a unique and geometrically consistent solution while also allowing the Grashof conditions to be satisfied. This contrasts with many numerical methods, where constraint verification is often deferred until the final stages. The construction proposed here is both practically relevant and introduces a novel graphical approach, broadening the scope of synthesis methods to encompass mechanisms exhibiting link dwells in planar motion and reaffirming the relevance of graphical approaches.

Keywords: mechanism synthesis, graphical methods, angular reversal, dwell mechanism, instantaneous center of rotation.

1. Introduction

The design of a new machine is typically preceded by an analysis aimed at the optimal realization of its intended utility functions. Mechanism synthesis offers the necessary tools for this process: selecting a suitable structural scheme

and determining the link dimensions to achieve the desired motion, subject to structural, geometric, kinematic, and dynamic constraints. When a designer selects a mechanism type for a given task and seeks optimal dimensions, the problem becomes one of dimensional synthesis. Early synthesis methods were developed graphically. Despite their inherent limitations, they retain both scientific and didactic value – especially in fostering the geometric intuition that is crucial to engineering practice. Although numerical methods prevail in modern research, graphical methods continue to offer insight into the underlying steps of the problem-solving process, making them foundational in engineering education and design practice.

Historically, many pioneering engineering achievements were the result of gradual evolution and refinement of earlier concepts. Graphical methods have long played a central role in technical problem-solving. In the 17th century, René Descartes introduced analytical geometry, and Galileo Galilei studied motion, laying the groundwork for later graphical representations. Newton's *Principia Mathematica* employed geometric reasoning to show that the trajectory of a body under an inverse-square central force is a conic section [1, 2]. Gaspard Monge developed descriptive geometry [3], which became essential for mechanism analysis. Other notable graphical contributions include Culmann's method for structural analysis [4], the Cremona method for trusses [5], and Mohr's circle for the visualization of stress and strain [6].

The early 20th century is often regarded as the golden age of graphical methods. During this period, graphical methods for the analysis and synthesis of mechanisms were intensively developed [7–10, 12]. Designing a mechanism to meet specific motion and functional requirements is inherently more complex than performing a mechanism analysis. In the field of mechanism synthesis and analysis, graphical methods were widely used until they were gradually supplanted by numerical approaches. The complexity and diversity of geometric transformations applied in mechanism design are well illustrated by the graphical techniques used in the synthesis of four-bar linkages for path generation with four or five prescribed precision points. With regard to geometric approaches, Burmester [9] and Caccarelli and Koetsier [17] introduced fundamental graphical techniques for the synthesis of linkages in the late 19th century. Other methods were subsequently developed to address motion generation problems. One widely adopted approach is Freudenstein's method, particularly for solving the three-position motion generation problem [15]. Additionally, the Roberts–Chebyshev theorem demonstrates that three distinct four-bar linkages can be constructed geometrically to produce the same coupler curve [7]. A comprehensive overview of graphical synthesis methods can be found in [11, 13–16]. Artobolevsky [11] applied his general theory of mechanism structure to advance graphical methods for the kinematic and kinetostatic analysis of mechanisms.

He also developed general methodologies for mechanism synthesis. Contemporary researchers continue to apply graphical methods to the synthesis of mechanisms with significant engineering applications [14, 16]. Lakshminarayana and Rao [18] performed a geometric synthesis of an RSSR crank-rocker mechanism designed for a prescribed oscillation angle and quick-return ratio. Furthermore, the study presented in [19] introduces a geometric synthesis method for function generation in a steering control mechanism with four discrete positions. This steering linkage forms a critical component of the steering systems used in most modern land vehicles.

The enduring inclusion of graphical methods in modern textbooks reflects their unique ability to visually communicate kinematic concepts. Dwell mechanisms – mechanisms that maintain a stationary position at specified points for a finite period of time – are particularly important in industrial applications. Numerous analytical and numerical synthesis methods have been developed for such mechanisms [20–37], primarily focusing on the dwell of links that move in purely translational or rotational motion. In most cases, these synthesis methods guide the coupler through several prescribed positions without imposing additional kinematic constraints. The graphical synthesis of a six-bar dwell linkage mechanism is presented in [38]. Although the core of this approach consists of geometric constructions, analytical equations were derived to optimize the solution.

This study considers the synthesis of a four-bar linkage with two prescribed angular reversal positions of the coupler – a problem not previously reported in the literature. More precisely, the mechanism under consideration is not classified as a dwell mechanism, since the motion stop is instantaneous. The application considered is a container-emptying mechanism, in which the container is mounted on the coupler, and stable discharge requires the coupler to pause at two distinct positions. In the basic case, the coupler rotates by $1/2\,\pi$ during discharge when the input link rotates through a predetermined angle. This configuration serves as the basis for generalization to coupler rotations in the range $1/2\,\pi \leq \delta < \pi$. The method guarantees the uniqueness and correctness of the solution and ensures that the Grashof conditions are satisfied. Unlike many existing graphical methods, in which arbitrary choices of selected parameters may lead to invalid results, the proposed construction systematically avoids such ambiguities. In contrast to optimization-based computer methods, where constraint violations are often detected late in the process, this graphical approach integrates all constraints from the outset.

2. Formulation of the problem

The objective is to construct graphically a four-bar linkage that guides a container so that it rotates exactly by an angle $1/2\,\pi \leq \delta < \pi$, caused by the rotation

of the driving link through a given angle $\pi + \alpha$, where $0 \leq \alpha \leq 1/2\,\pi$. To ensure an effective functionality, it is required that the coupler carrying the container operates between two extreme positions, as shown in Fig. 1:

– position (b) (container mounting),

– position (b') rotated by an angle δ (container unloading),

and that in these extreme positions the instantaneous angular velocity of the coupler ω_b is 0. Moreover the crank O_1A must complete a full revolution; therefore, crank-rocker mechanism is being designed. The instantaneous center of rotation (ICR) of the coupler lies at the intersection of the axes of the rotating links (crank and rocker). When the coupler changes its direction (ω_b is zero), the ICR lies at infinity. In these extreme positions, the crank and rocker are mutually parallel. Given the freedom of choice, it is assumed that in position (b) the coupler is perpendicular to the input link. The active link rotates through an angle of $\pi + \alpha$, and as a result, the coupler rotates counterclockwise from position (b) to position (b'). In position (b'), the instantaneous angular velocity of the coupler ω_b is zero, and a return rotation to position (b) follows while the active link completes a full rotation about O_1. In position (b), the direction of the coupler's velocity changes, meaning its instantaneous angular velocity is also zero. When the coupler is in position (b), the passive rotating link (rocker l) must be aligned parallel to O_1A. Then, the ICR of the coupler – denoted as C – lies at infinity. Similarly, when the coupler is in position (b'), the passive rotating link (l') must be aligned parallel to O_1A'. Then, the ICR of the coupler C′ also lies at infinity. Since the transition of the coupler from position (b) to position (b') is required to occur over a prescribed input crank rotation angle, the task corresponds to a time-prescribed motion synthesis problem. The schematic of the problem is shown in Fig. 1.

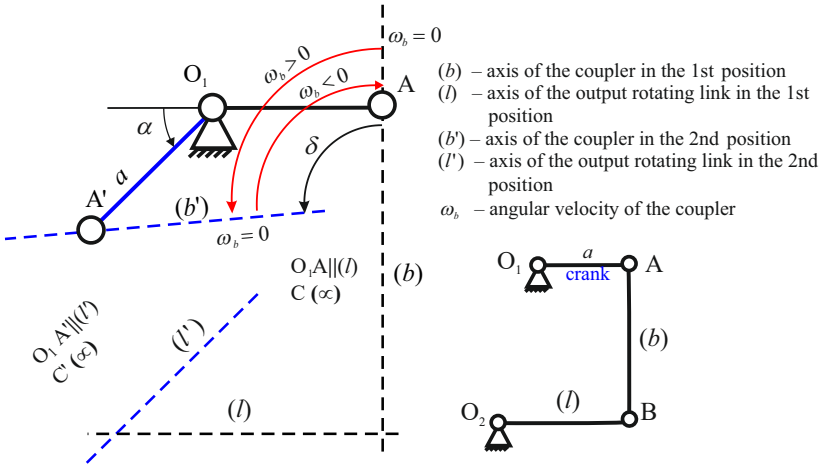

FIG. 1. Geometrical illustration of the problem.

3. Geometrical construction

3.1. Case 1: $\delta = 1/2\,\pi$

The method begins with a base case in which the coupler rotates by $1/2\,\pi$, and then generalizes to the range $1/2\,\pi \leq \delta < \pi$. In the first approach, let us take that $\delta = 1/2\,\pi$. Arbitrarily chosen quantities in a current step are labeled in green. Quantities determined in a current step are marked in blue, and quantities to be determined are in red.

1. Draw a pivotal joint O_1, choose an arbitrary length a of the driving rotating link, and sketch the link O_1A in its horizontal position O_1A and in the position O_1A', rotated by an angle $\pi + \alpha$ (Fig. 2a).
2. Draw the vertical line (2) passing through point A. Draw another line (1), rotated by the angle $\delta = 1/2\,\pi$, passing through A′. Draw arcs of radius $b = a$ centered at points A and A′ in order to find the locations of points B and B′, respectively (Fig. 2b).

The lines (3.1) and (3.2) represent the extreme positions (b) and (b') of the coupler, i.e., positions at which its instantaneous angular velocity is 0.

3. Connect points B and B′ with line (3) and measure the angle γ between line BB′ and the vertical line (Fig. 2c).

Note that always $\gamma \geq 1/2\,\alpha$ (a brief proof is provided in Sec. 4).

4. Shift point B′ to the right by Δ so that segment BB″ (4) forms an angle of $1/2\,\alpha$ with the vertical line (Fig. 2d).

As a consequence, a difference occurs between the coupler lengths |A′B″| and |AB| of Δ. The locations of points B and B″ have to be corrected in order to ensure that the coupler length is equal in both positions. For this purpose, an additional construction is required.

5. Draw a vertical segment of length Δ (Fig. 2e). From the upper end of this segment, draw a line parallel to BB″. From the lower end, draw a line at an angle of $1/4\,\pi$, extending until the two lines intersect. From the intersection point, draw a line perpendicular to Δ. The intersection of these perpendiculars divides Δ into h and y.

The shaded triangles formed are congruent, ensuring that $\Delta = h + y$.

6. Line BB″ (4) is translated parallelly (line 5) so that point B″ is shifted to the left along A′B″ by y; in consequence, B is lowered by h. The newly determined positions of the points are labeled as B^1 and B'^1.

7. To avoid introducing superfluous notation, we relabel the actual positions of points B^1 and B'^1 as B and B′, respectively. Draw the horizontal line (parallel to O_1A) passing through point B, as well as the line symmetrical to the BB′ (Fig. 2f). These two lines intersect at the rocker pivot O_2. This completes the construction.

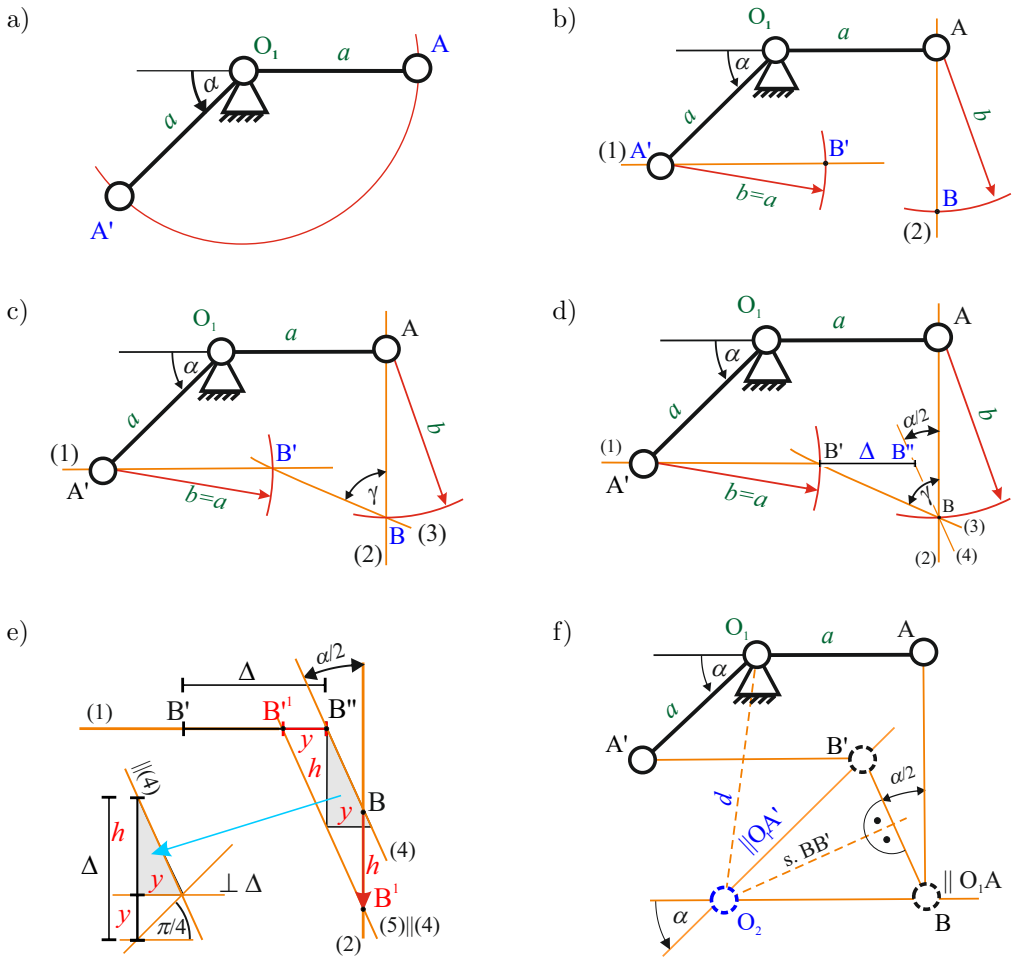

FIG. 2. Following steps of the synthesis procedure in the case when $\delta = 1/2\,\pi$; a) step 1, b) step 2, c) step 3, d) step 4, e) steps 5 and 6, f) step 7.

It is evident that $|O_2B| = |O_2B'|$. Note that BB′ must be inclined at $1/2\,\alpha$ to the vertical line (step 4) so that O_2B' is parallel to O_1A' and O_2B is parallel to O_1A, as required at the angular reversal positions. The resulting mechanism is shown in Fig. 3.

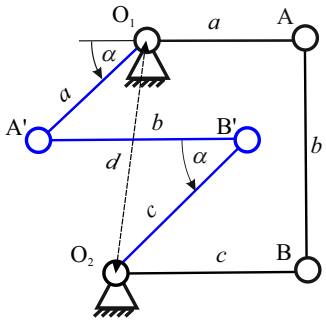

FIG. 3. Resulting mechanism for case 1.

3.2. Case 2: $\delta > 1/2\,\pi$

Let us consider the general case in which the coupler rotates by an angle $1/2\,\pi < \delta < \pi$, caused by the rotation of the driving link though a given angle $\pi + \alpha$.

1. Perform steps (1), (2), (3), and (4) as in the case of the first construction, keeping in mind that line (1) is rotated by an angle $\delta > 1/2\,\pi$ (Fig. 4a and Fig. 4b).

The difference between the coupler lengths $|A'B''|$ and $|AB|$ equals Δ. The quantities h and y are determined from additional constructions.

2. Draw a vertical segment ab of length Δ (Fig. 4c). From the upper end (a) of this segment, draw a line parallel to line (4). From the lower end (b) of the segment, draw a line at an angle $\pi - \delta$ (parallel to line (1)) until it intersects the previous line. As a result, the auxiliary quantity x is determined.

3. Then extend segment Δ by a specified value x (Fig. 4d). From the upper point (a), draw a new segment ad of length Δ at an arbitrary angle. Connect points (c) and (d), and then from point (b), draw a segment parallel to the line passing through points (c) and (d). In this way, the segment ad is divided into parts of lengths h and y.

4. In the main diagram (Fig. 4e), move line (4) in parallel so that point B is shifted along AB by a distance h. As a result, point B'' is shifted along $A'B''$ by y. This way we find the correct locations of points B $(= B^1)$ and B' $(= B'^1)$.

5. The rocker pivot O_2 lies at the intersection of the horizontal line passing through point B and the line symmetric to BB' (Fig. 4f). The resulting mechanism is shown in Fig. 5.

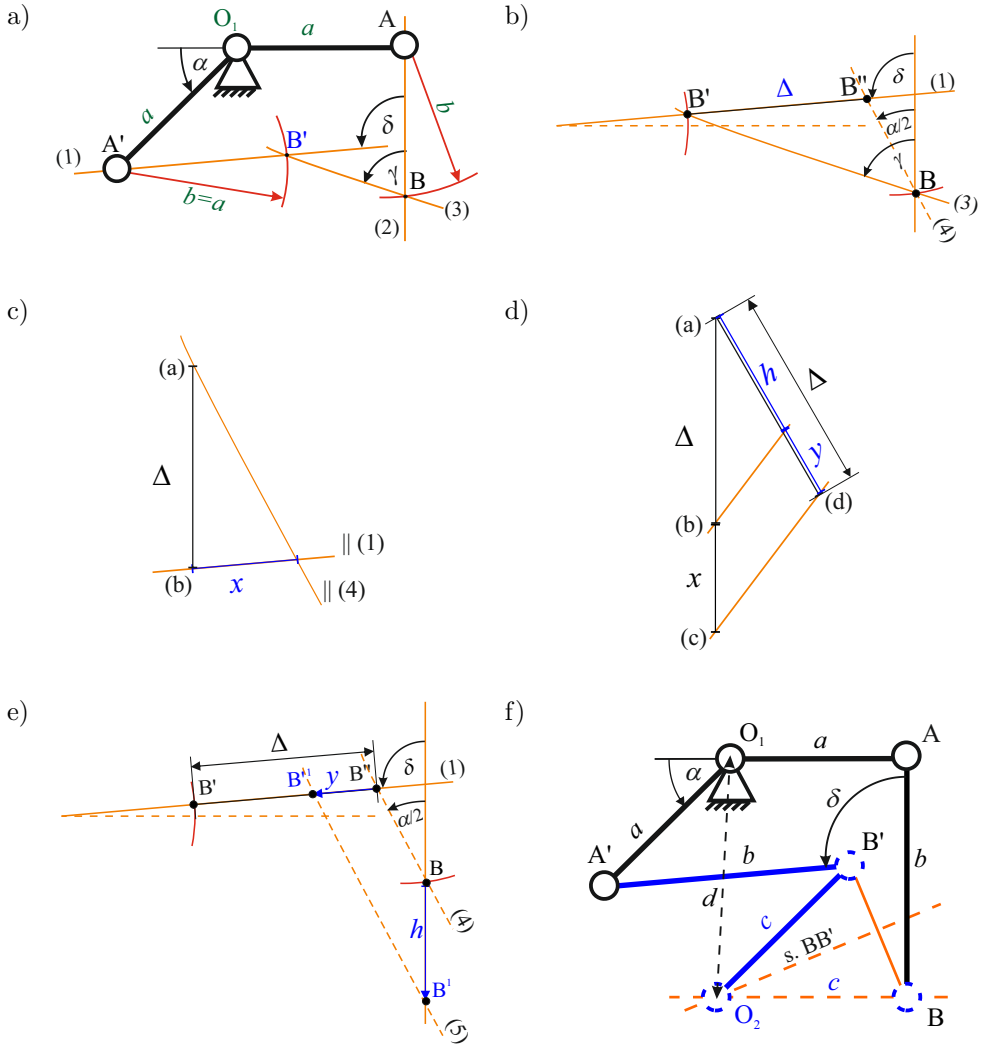

FIG. 4. Following steps of the synthesis procedure in the case when $\frac{1}{2}\pi < \delta < \pi$; a) steps 1 (1–3), b) step 1 (4), c) step 2, d) step 3, e) step 4, f) step 5.

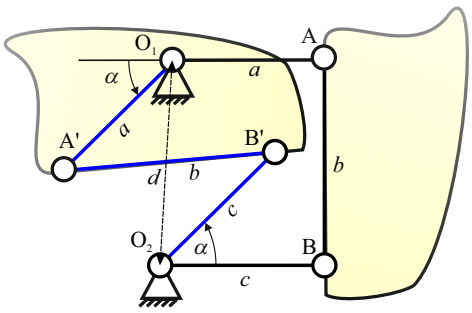

FIG. 5. Resulting mechanism for case 2: $\frac{1}{2}\pi < \delta < \pi$.

Note that, by similarity of triangles, the construction shown in Fig. 4c reflects the proportion:

$$\frac{h}{y} = \frac{\Delta}{x}. \tag{3.1}$$

By combining the equality $\Delta = h + y$ with Eq. (3.1), we obtain the following proportion:

$$\frac{\Delta + x}{\Delta} = \frac{\Delta}{h}, \tag{3.2}$$

geometrically presented in Fig. 4d. This way, using Thales' theorem, we find h and y.

4. Analysis of the solution

It should also be noted that for given values of α and δ, the only dimension selected arbitrarily is the angle between the driving link O_1A and the coupler AB in the initial position. For simplification of the solution procedure and the analysis of the solution's validity conditions, this angle is assumed to be $1/2\,\pi$, although other values are also permissible. The dimension b, initially chosen arbitrarily, is ultimately determined – similarly to dimensions c and d. A change in dimension a does not affect the mechanism's structure, as it leads to a proportional change in the remaining dimensions. This results in an affinely transformed mechanism. However, a solution does not exist for all possible values of α and δ. The solution space is constrained by the Grashof conditions, and by the requirement to avoid a defective solution due to the so-called branch defect (which is equivalent to circuit defect in the case of a crank-rocker mechanism) [35].

Let us determine the range of angles α and δ for which the construction guarantees a valid crank-rocker mechanism.

4.1. Procedure validity

We first justify that step (3), and consequently the subsequent steps of the algorithm, can be executed because γ is always greater than $1/2\,\alpha$. Let us observe that after initially assuming $b = a$ (step (2)), the angle γ is always greater than $1/4\,\pi$ (Fig. 6a). Since α lies within the interval $(0, 1/2\,\pi)$, the angle $1/2\,\alpha$ lies within $(0, 1/4\,\pi)$; therefore γ is always greater than $1/2\,\alpha$. In consequence, points B' and O_2 lie to the left of AB.

4.2. Branch defect analysis

Let us verify whether both positions of the mechanism are achieved within the same configuration of the four-bar linkage. In other words, we exclude the

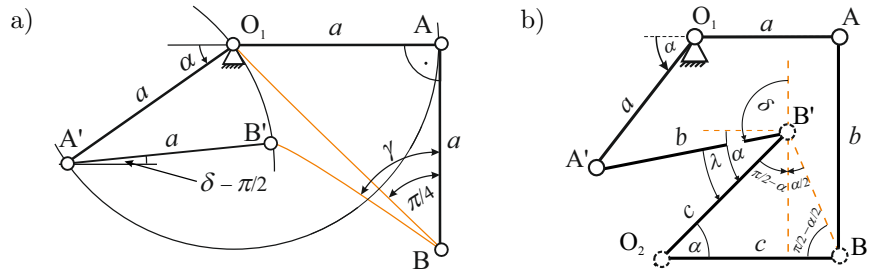

FIG. 6. a) Illustration that $\gamma > {}^1\!/_4\,\pi$ (a), b) illustration of angle λ for branch defect analysis.

so-called branch defect (or circuit defect). In the same configuration the smaller angle between links AB and BO_2 in each mechanism position is measured in the same direction – either clockwise or counterclockwise.

Since angle $\angle ABO_2$ is equal to $\pi/2$ and is measured counterclockwise, the smaller angle $\angle A'B'O_2\lambda$ must also be measured counterclockwise (Fig. 6b). Since $\delta + \lambda + \frac{\pi}{2} - \alpha = \pi$, $\lambda = \frac{\pi}{2} + \alpha - \delta$ and it must be greater than 0 and less than π, which occurs when

$$-\frac{\pi}{2} + \alpha < \delta < \frac{\pi}{2} + \alpha. \tag{4.1}$$

Let us note that when $\alpha + \frac{\pi}{2} = \delta$, the rocker coincides with the coupler, and this represents a singular configuration. If Eq. (4.1) is not satisfied, the crank-rocker mechanism would not be able to transition between the extreme positions without disassembly.

4.3. Grashof conditions

For the resulting mechanism to operate as a crank-rocker mechanism, the Grashof conditions must be satisfied. The link O_1A, with an arbitrarily chosen length a, is the shortest link.

The construction ensures that always $b > a$. Furthermore, $d^2 = b^2 + (c-a)^2$, hence $d > a$. It can be shown analytically that

$$c = a\frac{\sin\frac{\delta}{2} - \sin\left(\alpha - \frac{\delta}{2}\right)}{\sin\frac{\delta}{2} + \sin\left(\alpha - \frac{\delta}{2}\right)}. \tag{4.2}$$

Let us check when $c > a$:

$$a\frac{\sin\frac{\delta}{2} - \sin\left(\alpha - \frac{\delta}{2}\right)}{\sin\frac{\delta}{2} + \sin\left(\alpha - \frac{\delta}{2}\right)} > a, \qquad \frac{-2\sin\left(\alpha - \frac{\delta}{2}\right)}{\sin\frac{\delta}{2} + \sin\left(\alpha - \frac{\delta}{2}\right)} > 0,$$

$$2\sin\left(\alpha - \frac{\delta}{2}\right)\left(\sin\frac{\delta}{2} + \sin\left(\alpha - \frac{\delta}{2}\right)\right) < 0.$$

The dimension c is greater than a when

$$\alpha < \frac{\delta}{2}. \tag{4.3}$$

In the following proofs, we assume that Eq. (4.3) is satisfied. We now check whether the sum of the minimal and maximal link lengths is less than the sum of the remaining links:

1. Let us assume that dimension d is the largest. We proceed with an indirect proof. Assume that the sum of the minimal and maximal link lengths is greater than the sum of the remaining link lengths: $a + d > b + c$, $d > b + (c - a)$, $d^2 = b^2 + (c - a)^2 > (b + (c - a))^2$. This leads to a contradiction; therefore, the assumption is false, and it must be that the sum of the extreme link lengths is less than the sum of the remaining link lengths: $a + d < b + c$.
2. Let us assume that the dimension b is the greatest. However, $d^2 = b^2 + (c-a)^2$, so it follows that b is always less than d. Consequently, b cannot be the greatest.
3. Let us assume that c is maximal. In this case, we provide a direct proof, that the sum of the minimal and maximal link lengths is lower than the sum of the remaining link lengths. Then $a + c < d + b$, $d > (a + c) - b$, $d^2 = b^2 + (c-a)^2 > ((c + a) - b)^2$; $d^2 = b^2 + (c-a)^2 > b^2 - 2b(c+a) + (c+a)^2$, $2ac < b(c + a)$, which is always true when Eq. (4.4) is satisfied.

The Grashof conditions can be also proved geometrically. In summary, by combining Eq. (4.2) with Eq. (4.3), the following inequality guarantees obtaining a crank-rocker mechanism free of branch defect:

$$2\alpha < \delta < \frac{\pi}{2} + \alpha. \tag{4.4}$$

In summary, we observe that the construction also covers the case in which the driving link rotates through an angle of $\pi - \alpha$. In that case, it is sufficient to reverse the direction of rotation of link O_1A. In the range where dimension c is smaller than a, the link O_2B becomes the crank and O_1A becomes the rocker. It was shown that for a fixed angle $O_1AB = {}^1\!/_2\,\pi$, the problem has exactly one solution. If, for functional reasons, the angle O_1AB must differ from ${}^1\!/_2\,\pi$, the synthesis process must be carried out exactly as presented. However, a separate analysis of the Grashof conditions should be performed, and conditions must be established to ensure that a branch defect does not occur.

4.4. Uniqueness of the solution

We demonstrate that, when the angle ABO_2 is equal to ${}^1\!/_2\,\pi$, the presented configuration leads to a unique and correct solution to the synthesis problem.

Let us consider alternative potential solution paths. Note that the links AB and A′B′ can also be constructed along lines (1) and (2) in the opposite directions, i.e., to the left from point A′ and upward from point A.

We now examine the case illustrated in Fig. 7, aiming to identify a position of joint B located in the upper half-plane with respect to A. Due to space limitations, only a proof sketch is presented here, with its essential elements depicted in Fig. 7. The segment AB′1 is inclined at an angle of $\frac{1}{2}\alpha$ relative to the vertical axis. We begin with a situation where the length of the coupler in the second position is |A′B′1|, whereas in the first position the coupler length in the initial configuration is effectively zero, i.e., |AB| = |AA| = 0. However, by translating the line AB′1 parallel to itself, it becomes evident that the rate of increase in the length of link AB – denoted n_1 – is greater than that of link A′B′ – denoted n_1'. Therefore, it is guaranteed that positions B and B′ can be found such that |AB| = |A′B′|. Nevertheless, the configurations O_1ABO_2 and $O_1A'B'O_2$ belong to two distinct branches of the mechanism's configuration space (Fig. 8). The angle ABO_2 is measured in the opposite direction compared to $A'B'O_2$. This results in a solution that exhibits a branch defect – a condition where the same input motion leads to two distinct configurations. When the input link is rotated to position O_1A', the remaining links will not attain the desired position $A'B'O_2$, but instead will settle into configuration $A'B''O_2$.

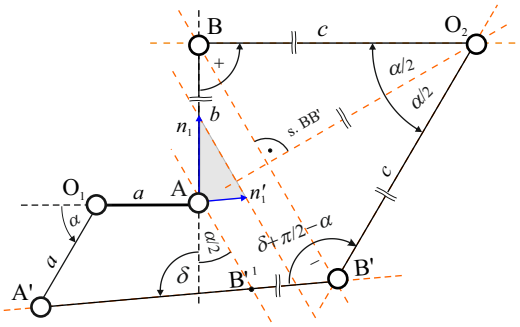

FIG. 7. Second solution of the problem (construction no. 2).

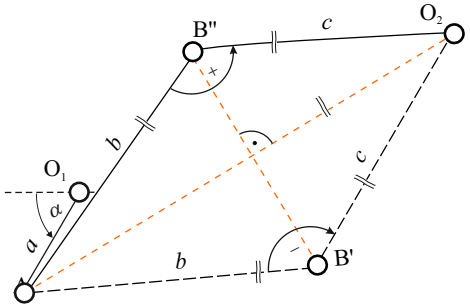

FIG. 8. Illustration for the branch defect of the second solution.

Having excluded the second construction due to branch defect, we now turn to a third possible configuration, illustrated in Fig. 9. We seek a configuration in which joint B is located in the upper half-plane with respect to A, while joint B′ lies to the left of joint A′. However, it can be readily demonstrated that, under such conditions, it is impossible to satisfy the constraint $|AB| = |A'B'|$. The only exception occurs when $\alpha = {}^1\!/_2\,\pi$. Even in this special case, however, the resulting configuration would still exhibit a branch defect, rendering it invalid for the intended mechanism behavior.

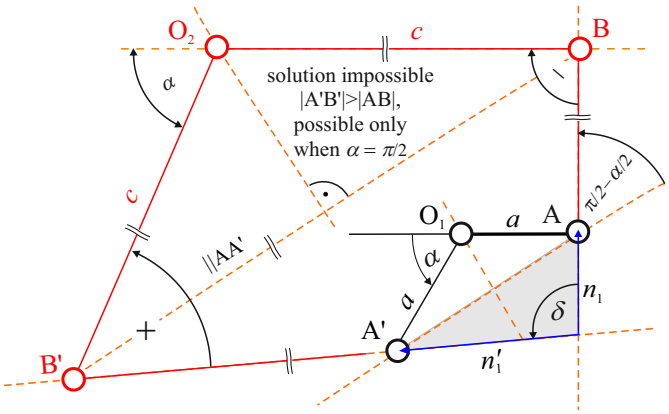

FIG. 9. Lack of a solution in the case of construction no. 3.

The configuration in which joint B lies in the lower half-plane with respect to A and joint B′ lies to the left of A′ also does not yield a valid solution, since in this case the condition $|AB| < |A'B'|$ is always satisfied.

Consequently, all geometrically feasible constructions consistent with the imposed constraints have been systematically evaluated.

5. Conclusions

This paper presented a novel graphical synthesis method for a four-bar linkage designed to achieve two prescribed angular reversal positions of the coupler – a problem not previously addressed in the literature. In contrast to many graphical methods that exhibit ambiguity related to trial-and-error selection of geometric parameters, the proposed approach guarantees solution correctness and uniqueness, while inherently satisfying the Grashof conditions from the outset. This stands in contrast to numerical methods, where constraint verification is often postponed until the final design stages.

The method is straightforward to implement and allows for clear visualization of the solution. It also enables more advanced kinematic analyses when

needed. The resulting construction combines practical relevance with theoretical novelty, thereby expanding the range of design possibilities for mechanisms involving angular coupler dwells and reaffirming the continued usefulness of graphical techniques.

Although graphical methods are generally limited to simpler design problems, they provide intuitive insight into the problem-solving process by visually expressing fundamental kinematic relationships. A notable advantage of the proposed approach is its didactic value: it leverages kinematic properties of lever mechanisms – components that are seldom applied in practice and often poorly understood by students – while making them accessible and comprehensible through graphical representation.

Fundings

This work was supported by Polish Ministry of Education and Science (Ministerstwo Edukacji i Nauki) under grant no. 0612/SBAD/3640.

Conflict of interest

The author declares that he has no known competing financial interests or personal relationships that could have appeared to influence the work reported in this paper.

Author's contribution

The author reviewed and approved the final manuscript.

References

1. Newton I., *Mathematical Principles of Natural Philosophy* [in Latin: *Philosophiæ Naturalis Principia Mathematica*], 1687.
2. Lohne A., The increasing corruption of Newton's diagrams, *History of Science*, **6**(1): 69–89, 1967, https://doi.org/10.1177/007327536700600105.
3. Monge G., *Géométrie Descriptive*, 1799.
4. Culmann K., *Graphic Statics* [in German: *Die Graphische Statik*], 1866.
5. Cremona L., *Reciprocal Figures in Graphical Statics* [in Italian: *Le Figure Reciproche Nella Statica Grafica*], 1872.
6. Mohr C.O., *Contributions to the Theory of the Strength of Structures* [in German: *Beiträge zur Theorie der Festigkeit der Bauwerke*], Springer, Berlin, 1882.
7. Chebyshev P., *On the Theory of Mechanisms*, St. Petersburg, 1854.

8. Reuleaux F., *The Kinematics of Machinery*, Macmillan, London, 1876.

9. Burmester L., *Textbook of Kinematics. Volume 1: Planar Motion* [in German: *Lehrbuch der Kinematik. Band 1: Die ebene Bewegung*], Leipzig, 1888.

10. Kennedy A.B.W., *Mechanisms, or the Development of Machines*, Macmillan, London, 1894.

11. Artobolevsky I.I., *Mechanisms in Modern Engineering Design*, Mir Publishers, Moscow, 1975.

12. Barton L.O., *Mechanism Analysis. Simplified and Graphical Techniques*, 2nd ed., CRC Press, Boca Raton, 1993, https://doi.org/10.1201/b13243.

13. McCarthy J.M., *Geometric Design of Linkages*, Springer, New York, 2000.

14. Erdman A.G., Sandor G.N., Kota S.S., *Mechanism Design: Analysis & Synthesis, Volume 1*, 4th ed., Prentice-Hall, New Jersey, 2001.

15. Freudenstein F., Approximate synthesis of four-bar linkages, *Resonance*, **15**(8): 740–767, 2010, https://doi.org/10.1007/s12045-010-0084-7.

16. Uicker J.J., Pennock G.R., Shigley J.E., *Theory of Machines and Mechanisms*, 3rd ed., Oxford University Press, New Delhi, 2012.

17. Ceccarelli M., Koetsier T., A theory and its application for mechanism design at the end of 19th century, *Journal of Mechanical Design*, **130**(7): 072301, 2008, https://doi.org/10.1115/1.2918911.

18. Lakshminarayana K., Rao L.B., Graphical synthesis of the RSSR crank-rocker mechanism, *Mechanism and Machine Theory*, **19**(3): 331–336, 1984, https://doi.org/10.1016/0094-114X(84)90067-3.

19. Wang H., Lin S., Geometric synthesis method for function generation of steering control mechanism with four positions, [in:] *Advances in Mechanism and Machine Science. IFToMM WC 2019. Mechanisms and Machine Science*, Uhl T. [Ed.], Vol. 73, Springer, Cham, pp. 1431–1440, 2019, https://doi.org/10.1007/978-3-030-20131-9_141.

20. Wang A.C., Lee T.W., Design and analysis of momentary-dwell mechanisms, *Journal of Mechanisms, Transmissions, and Automation in Design*, **107**(1): 131–140, 1985, https://doi.org/10.1115/1.3258676.

21. Chase T.R., Erdman A.G., Riley D.R., Triad synthesis for up to five design positions with application to the design of arbitrary planar mechanisms, *Journal of Mechanisms, Transmissions and Automation in Design*, **109**(4): 426–434, 1987, https://doi.org/10.1115/1.3258813.

22. Kota S., Erdman A.G., Riley D.R., Development of knowledge base for designing linkage-type dwell mechanisms: Part 1 – Theory, *Journal of Mechanisms, Transmissions and Automation in Design*, **109**(3): 308–315, 1987, https://doi.org/10.1115/1.3258795.

23. Kota S., Erdman A.G., Riley D.R., Development of knowledge base for designing linkage-type dwell mechanisms: Part 2 – Application, *Journal of Mechanisms, Transmissions and Automation in Design*, **109**(3): 316–321, 1987, https://doi.org/10.1115/1.3258796.

24. Kota S., Generic models for designing dwell mechanisms: A novel kinematic design of Stirling engines as an example, *Journal of Mechanical Design*, **113**(4): 446–450, 1991, https://doi.org/10.1115/1.2912803.

25. Subbian T., Flugrad D.R., Five position triad synthesis with applications to four- and six-bar mechanisms, *Journal of Mechanical Design*, **115**(2): 262–268, 1993, https://doi.org/10.1115/1.2919186.

26. Yu H., Wang Z., Tang D., Li J., Study on numerical comparison method for planar six-bar dwell mechanism synthesis, [in:] *Proceedings of the 11th IFToMM World Congress*, pp. 1–5, 2003.

27. Pennock G.R., Israr A., Kinematic analysis and synthesis of an adjustable six-bar linkage, *Mechanism and Machine Theory*, **44**(2): 306–323, 2009, https://doi.org/10.1016/j.mechmachtheory.2008.04.007.

28. Jagannath M., Optimisation design of six-bar double dwell mechanisms: A new approach, *Applied Mechanics and Materials*, **110–116**: 5216–5222, 2012, https://doi.org/10.4028/www.scientific.net/AMM.110-116.5216.

29. Agarwal S., Badduriy J., Bandyopadhyay S., Optimal synthesis of six-bar function generators, [in:] *The 14th IFToMM World Congress*, 2015, https://doi.org/10.6567/IFToMM.14TH.WC.OS2.031.

30. Kharzhevskyi V.O., Kinematic synthesis of linkage mechanisms using Burmester points at the given dwell duration of the output link, *Advances in Science and Technology Research Journal*, **11**(2): 139–145, 2017, https://doi.org/10.12913/22998624/68465.

31. Myszka D., Murray A., Armstrong A., Ali H., Mechanical presses driven by a geared five-bar with sliding output to produce a prolonged dwell, [in:] *Advances in Mechanism and Machine Science. IFToMM WC 2019. Mechanisms and Machine Science*, Uhl T. [Ed.], Vol. 73, Springer, Cham, pp. 309–318, 2019, https://doi.org/10.1007/978-3-030-20131-9_31.

32. Yin L., Huang L., Huang J., Xu P., Peng X., Zhang P., Synthesis theory and optimum design of four-bar linkage with given angle parameters, *Mechanics Science*, **10**(3): 545–554, 2019, https://doi.org/10.5194/ms-10-545-2019.

33. Simionescu P.A., New and revised mechanism classifications: Proposal and motivation, [in:] *Advances in Mechanism and Machine Science. IFToMM WC 2019. Mechanisms and Machine Science*, Uhl T. [Ed.], Vol. 73, Springer, Cham, 2019, https://doi.org/10.1007/978-3-030-20131-9_345.

34. Jagannath M., Bandyopadhyay S., Path generation with dwells in the optimum dimensional synthesis of Stephenson III six-bar mechanisms, *Mechanism and Machine Theory*, **144**: 103650, 2020, https://doi.org/10.1016/j.mechmachtheory.2019.103650.

35. Hernández A., Muñoyerro A., Urízar M., Amezua E., Comprehensive approach for the dimensional synthesis of a four-bar linkage based on path assessment and reformulating the error function, *Mechanism and Machine Theory*, **156**: 104126, 2021, https://doi.org/10.1016/j.mechmachtheory.2020.104126.

36. Kharzhevskyi V., Pashechko M., Tatsenko O., Marchenko M., Nosko P., The synthesis of dwell mechanisms on the basis of straight-line linkages with fivefold interpolation nodes, *Advances in Science and Technology Research Journal*, **15**(1): 18–25, 2021, https://doi.org/10.12913/22998624/128817.

37. Wang B., Du X., Ding J., Dong Y., Wang C., Li X., The synthesis of planar four-bar linkage for mixed motion and function generation, *Sensors*, **21**(10): 3504, 2021, https://doi.org/10.3390/s21103504.

38. Čavić M., Penčić M., Rackov M., Doric J., Lu Z., Graphical synthesis of 6-bar dwell linkage mechanism, *FME Transaction*, **47**(2): 226–233, 2019, https://doi.org/10.5937/fmet1902226C.

Received May 28, 2025; revised July 9, 2025; accepted August 12, 2025; available online January 20, 2026; version of record March 2, 2026; published issue March 30, 2026.

Engineering Transactions, **74**(1): 69–84, 2026, https://doi.org/10.24423/engtrans.2025.3603
Institute of Fundamental Technological Research Polish Academy of Sciences (IPPT PAN)
Université de Lorraine • Poznan University of Technology

Research Paper

A Prime-Number/Uniform Angular Distribution Criterion for Blade Vibration Reduction

Yong Li, Yaao Di, Wenzheng Dong, Fangxiang Yin, Yihao Yin, Shanling Han*

College of Mechanical and Electronic Engineering, Shandong University of Science and Technology
Qingdao, China

*Corresponding Author: 15806673969@163.com

Currently, the vibration noise of casting cleaning equipment exceeds 95 dB, which not only shortens the equipment's service life but also jeopardizes workers' health. The primary cause lies in the resonance tendency resulting from an uneven distribution of blades in the shot-blasting device. In this paper, a prime-number/uniform angular distribution criterion and a dynamic balance elimination relationship are established to minimize resonance coupling while accounting for the internal characteristics of the shot-blasting device and blade assembly. Subsequently, a shot-blasting device with seven prime-number angular front-curved blades was designed and fabricated, and the dynamic imbalance caused by uneven blade distribution was compensated for by drilling. We employed the discrete element method to evaluate projectile velocity and stability. The results indicate that the shot velocity reaches a maximum of 75 m/s, with fluctuations within 4 m/s. After reaching 0.24 s, particles accelerated by the shot-blasting device achieve relative stability. Finally, vibration data acquired at a sampling frequency of 10 Ksps demonstrates that noise levels are reduced from 97 dB (traditional structure) to 93.3 dB (new model). This new criterion for shot-blasting machine models mitigates operational vibration while enhancing working conditions and improving overall stability and system reliability.

Keywords: shot-blasting machine, vibration-induced noise, structural optimization, prime-number/uniform angular distribution criterion, shot-blasting device with seven prime-number angular front-curved blades.

1. Introduction

As a surface treatment equipment, the shot-blasting machine finds extensive application across various industries. However, operational vibration and noise issues associated with this machinery significantly impact equipment performance, personnel well-being, and environmental conditions [1]. The vibration

frequency can be decomposed into the fundamental frequency and its second harmonic using Fourier series analysis [2–5]. The fundamental frequency for uniformly distributed shot-blasting blades corresponds to the fundamental blade-passing frequency (BPF). Resonance occurs when either the fundamental frequency or the second harmonic ($2 \times$ BPF) of the blade coincides with the natural frequency of the shot-blasting device [6–9]. Due to the periodic nature of blade rotation, uniformly distributed blades are more likely to induce resonance by matching the system's natural frequency, thereby increasing the associated risk.

Using the studies from other industries, some researchers have designed blades as a means of reducing equipment noise. Luo *et al.* [10] reported that a non-uniformly arranged seven-blade fan exhibits distinctive noise characteristics during tests. In comparison with a uniformly arranged fan, the noise characteristics of a non-uniformly arranged fan display a broader harmonic distribution and a reduced disparity between discrete and broadband noise. It is evident that incorporating non-uniform blade arrangements offer certain advantages in vibration and noise reduction; however, prime-number angular designs have been applied only in one instance within other industries and lacks a general design principle. In this study, non-uniform blade design is incorporated into shot-blasting machines and a prime-number/uniform angular distribution criterion is proposed for a new type of shot blaster. Zhang *et al.* [11] analyzed the blades of shot-blasting machines and found that rectangular blades can alleviate stress concentration, providing valuable guidance for improving reliability and extending service life of these machines. Currently, although blade optimization has been employed to reduce stress concentration, blade arrangement has received little attention, and improvements in vibration-induced noise reduction for shot-blasting machines remain insufficient.

The objective of this study is to provide theoretical support for optimizing the design of a shot-blasting device through of vibration signal analysis and the establishment of blade selection criteria. The optimization design is conducted based on a prime-number/uniform angular distribution vibration reduction criterion, leading to the proposal of a shot-blasting device model incorporating seven prime-number angular front-curved blades. Subsequent analysis of object velocity and stability during the ejection process is conducted using the discrete element method [12]. By calculating parameters such as particle velocity changes, we can evaluate the ejection stability of the device. To address the imbalance caused by uneven blade distribution, perforations are introduced in the impeller disk to adjust the rotating dynamic balance of the shot-blasting device. Finally, vibration signal acquisition equipment is used to compare vibration signal characteristics between the newly designed shot blaster and traditional models, thereby verifying the performance advantages of the proposed criterion-based impeller structure.

2. Establishment of the prime-number/uniform angular distribution criterion for shot blasting

The design of a shot-blasting device not only requires blade shape improvement, but also optimization of the impeller body design to reduce resonance effects [13–17]. Vibration signal analysis reveals resonance between the motor and the impeller body, indicating the necessity for optimization of the shot-blasting device design. A key measure is to optimize the blade distribution angles and establish a prime-number/uniform angular distribution criterion for the blades. The criterion is defined through the following steps:

- calculate the desired uniform angular spacing based on the number of blades,
- select prime-number angular positions within the range of 1° to 361° to address centroid offset caused by blade arrangement,
- determine a set of angles with minimal standard deviation using Eq. (2.1).

This criterion aids in selecting blade mass angles close to the ideal uniform angle, thereby effectively enhancing the system's resonance frequency, reducing vibration and noise resulting from resonance, and improving the mechanical equipment's operational smoothness.

The prime-number/uniform angular distribution criterion relationship is derived from the standard deviation formula:

$$S = \sqrt{\frac{\sum_{i=1}^{n} \left(\operatorname{wrap}\left(\theta_i + \varphi\right) - \frac{360^\circ}{n} \cdot i \right)^2}{n}}, \tag{2.1}$$

where S is the standard deviation, θ_i is the i-th prime-number angular position (in degrees), n is the number of blades in the shot-blasting machine, φ is the phase shift, with $\varphi \in [0^\circ, 360^\circ/n)$. To account for the cyclic nature of $[0^\circ, 360^\circ)$, differences are evaluated as minimum signed circular (wrapped) errors using $\operatorname{wrap}(x) = ((x + 180^\circ) \bmod 360^\circ) - 180^\circ$. By minimizing S with respect to φ, the uniformity of the blade distribution relative to an arbitrarily shifted uniform distribution can be assessed.

In practice, the majority of existing shot-blasting devices employ either six or eight blades, and the number of shot-blasting shafts is typically four. An imbalance in blade number can adversely affect both the distribution and number of smaller shafts. An excessive number of small shafts hampers ejection efficiency, whereas an insufficient number compromises the structural strength of the shot-blasting device. Accordingly, based on the proposed prime-number/uniform angular distribution criterion of the blade, this research opts for a specific case: a shot-blasting device with seven prime-number angular blades. Let $n = 7$, and

substitute it into the prime-number/uniform angular distribution criterion, as per established academic standards.

Consequently, an impeller body for a prime-number angular blade vibration-damping shot-blasting device is established. The utilization of prime-number angular positions reduces the likelihood of resonance with other components due to their unique distribution characteristics, as they do not share common factors with other excitation frequencies in the system.

Subsequently, the impeller model of the shot-blasting device is established. Since prime numbers do not share common factors with other numbers, the angular distribution using prime-number indexing can reduce the risk of resonance with other components. According to Eq. (2.1), when $\varphi \in [0^\circ, 360^\circ/7)$, the minimum standard deviation is obtained by applying a search step size of $\Delta\varphi = 0.1^\circ$, which enhances the precision of the results, while a longer search interval ensures the robustness of the calculation. The results show that at $\varphi = 14.7^\circ$, the optimal prime-number angular positions are 37°, 89°, 139°, 191°, 241°, 293°, and 347°, yielding a standard deviation $S \approx 0.99$. This represents the smallest standard deviation, indicating that the angular distribution of the blade positions is closest to an equidistant distribution, thus ensuring greater stability and reliability of the system.

In terms of geometric uniformity, S reflects the degree of angular distribution uniformity, with smaller values of S indicating better uniformity. However, completely equidistant distributions do not necessarily result in optimal dynamic performance. A perfectly uniform distribution concentrates excitation energy at the BPF and its harmonics, which could lead to resonance if these frequencies coincide with the system's natural frequencies. Therefore, the design criterion is not solely to minimize S, but rather achieve minimal S while simultaneously ensuring that dominant frequency orders are shifted to avoid resonance with the system's natural frequencies, thereby optimizing the system's stability and operational reliability.

To further mitigate resonance risk, a resonance risk index $R(\Theta)$ is introduced to assess the relative relationship between blade frequencies and the system's natural frequencies. The resonance risk index is calculated as follows:

$$R(\Theta) = \max_{h\in\mathcal{H}} \left| \frac{1}{n} \sum_{i=1}^{n} e^{jh\theta_i} \right|, \tag{2.2}$$

where $\mathcal{H}$ represents the set of critical frequency orders corresponding to the system's natural frequencies and h denotes the frequency order. In this study, $h = 1, 2, 3, 4, 8, 9$, covering the fundamental frequency and its harmonics. Here, θ_i represents the angular position of the i-th blade.

The parameter $R(\Theta)$ represents the resonance risk index, reflecting the relationship between excitation frequency of the blades and the system's natural

frequency. The value of $R(\Theta)$ indicates the degree of difference between excitation frequency and natural frequencies. A value of $R(\Theta)$ close to 0 suggests no resonance risk, while $R(\Theta)$ approaching 1 indicates a significant risk of resonance. The value of $R(\Theta)$ ranges from 0 to 1, with 0 indicating no resonance risk and 1 corresponding to a high resonance risk. If $R(\Theta)$ is less than 0.1, it indicates low resonance risk, and the system's frequency distribution is generally well aligned. Based on the above frequency analysis, the calculated value of $R(\Theta) = 0.0736$ suggests a low resonance risk and demonstrates the system's favorable frequency alignment, thus avoiding potential resonance problems.

The generated blade angles are all prime-number angular positions, and since they share no common factors, their multiples do not coincide. Due to the distinct nature of prime numbers, their distribution is 'uniform,' thereby avoiding synchronous resonance among the blades. For the seven blade angles $\theta_1, \theta_2, \theta_3, ..., \theta_7$, their relationship is defined by Eq. (2.3). If $\Delta\theta$ is a fixed value (e.g., uniformly distributed angles), the motion periods of the blades become synchronized, leading to resonance. However, if the blade angles are selected as prime-number angular positions (such as 37°, 89°, etc.), the multiples of these angular values do not overlap within the same cycle, thereby preventing resonance:

$$\theta_i = \theta_1 + i \cdot \Delta\theta \quad (i = 1, 2, ..., 7), \tag{2.3}$$

where θ_i is the angle of the i-th blade and $\Delta\theta$ is the angular difference between adjacent blades.

In rotating machinery, the angular distribution of blades is directly related to their vibration modes and frequencies. Each blade angle can be considered a vibration source associated with the rotational period. When the angular intervals between blades follow a regular pattern, vibrations from all blades may synchronize at specific rotational frequencies, leading to resonance. In contrast, blade angles exhibit a prime-number distribution to avoid repeated angular intervals and suppress resonance effectively prevents such synchronization. Due to the inherent disparities between prime numbers – such as their lack of common factors – their multiples do not coincide within the same rotational cycle. Consequently, blades positioned at distinct prime-number angular positions exhibit differentiated rotational frequencies, thereby suppressing resonance.

As shown in Table 1, the parameters of the shot-blasting machine during operation are listed. All blades are made from high-chromium cast iron and have uniform dimensions.

The unbalanced mass of the newly designed shot-blasting machine is subsequently determined by employing Eq. (2.4) to Eq. (2.6). The blade material is high-chromium cast iron, a density is $7.8 \times 10^3\,\mathrm{kg/m^3}$, and a mass is 0.0836 kg. The static equilibrium mass of each blade is calculated to be 11.1796 g. The gov-

Table 1. Material parameters for different components.

Component	Parameter	Numerical value
Steel pellet (cast steel)	Poisson's ratio	0.3
	Density [kg/m^3]	7.8×10^3
	Shear modulus [Pa]	8×10^{10}
Impeller body, directional sleeve, shot-dividing wheel, blades (all components are made of high-chromium cast iron)	Poisson's ratio	0.3
Impeller body	Density [kg/m^3]	7.8×10^3
	Shear modulus [Pa]	7.6×10^{10}
	Impeller body speed [rpm]	3000

erning equations for calculating the unbalanced mass and its orientation are as follows, leading to a conclusive result:

$$\begin{cases} (m_b r_b)_x = -\sum_{i=1}^{n} mr \cdot \cos(\theta_i), \\ (m_b r_b)_y = -\sum_{i=1}^{n} mr \cdot \sin(\theta_i), \end{cases} \tag{2.4}$$

$$\alpha_b = \arctan \frac{(m_b r_b)_y}{(m_b r_b)_x}, \tag{2.5}$$

$$m_b r_b = \sqrt{\left[(m_b r_b)_x^2 + (m_b r_b)_y^2\right]}, \tag{2.6}$$

where m_b is the equilibrium mass, r_b is the distance from the blade center of mass to the rotor center, m is the mass of a single blade, r is the distance from the blade center of mass to the edge of the main (secondary) disk, θ_i is the i-th blade angular position on the shot-blasting machine, n is the number of blades on the shot-blasting machine, and α_b is the phase angle.

We then applied a formula to calculate the dynamic balance of the shot-blasting blade. The eccentric mass for static balance is determined, and we measure the distanced from the centroid of the shot-blasting blade to the disk edges as 68 mm for the main disk, and 52.5 mm for the secondary disk. By applying Eq. (2.7) and Eq. (2.8), we determine that dynamic balance masses were calculated as 4.890 g for the main disk, and 6.309 g for the secondary disk:

$$m_i r_i = \frac{y_1 + y_2 - y_i}{y_1 + y_2} m_b r_b, \tag{2.7}$$

$$m_{bi} = \frac{m_i r_i}{r_{bi}}, \tag{2.8}$$

where $m_i r_i$ is the blade is assigned to a mass radius product on a disk $i = 1$ for the primary disk and $i = 2$ for the secondary disk, y_i is the distance between the blade's center of mass and the edge of the main (secondary) disk, m_{bi} is dynamic balance mass, r_{bi} is the distance from the center of mass of the dynamically balancing mass to the disk center.

After assembly, the impeller body is equipped with blades and subjected to unbalance detection on a dynamic balancing machine (as depicted in Fig. 1), with the machine parameters listed in Table 2. The rotational acceleration test of the impeller body is conducted using an electrical measurement system to quantify the unbalance. The obtained test results reveal that at 288°, the main disk exhibits an unbalance of 2.924 g, while the secondary disk shows an unbalance of 4.460 g at 272°; after rotation ceases, the main disk displays an unbalance of 2.918 g while the secondary disk shows an unbalance of 4.520 g.

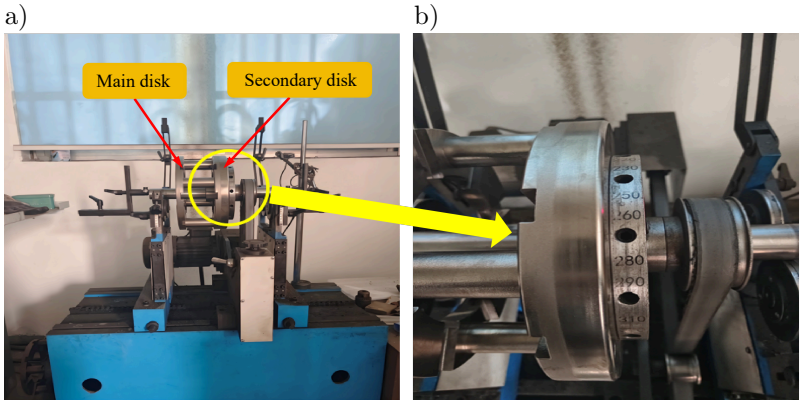

FIG. 1. Imbalance detection of the impeller body using a dynamic balancing machine (a), angle indicator on the dynamic balancing machine (b).

TABLE 2. Dynamic balancing machine parameters.

Parameter	Value
Maximum rotor weight	0.03 kg to 300 kg
Maximum rotor diameter	100 mm to 800 mm
Maximum support distance	250 mm to 2100 mm
Rotor shaft diameter range	5 mm to 120 mm
Balancing speed range	400 rpm to 3000 rpm
Drive motor power	0.05 HP to 3 HP
Minimum measurable imbalance	0.01 g to 0.1 g
Imbalance reduction rate	$\geq$95 %
Minimum achievable specific imbalance	0.2 g · mm/kg
Applicable rotor types	Motor rotors, flywheels, impeller body, etc.

Compared with the calculated results, there is a discrepancy of 1.966 g in balance mass of the main disk and 1.849 g for the secondary disk. When at rest, the main disk exhibits a difference of 1.972 g while the secondary disk shows a difference of 1.789 g.

Deviations were observed between the test results of the dynamic balancing machine (e.g., residual unbalance) and the theoretical values. Potential sources of error include installation accuracy, sensor calibration, and bearing clearance. During installation, minor deviations in the blades and disks may compromise geometric symmetry and precise alignment, thereby affecting unbalance measurement. Calibration errors in sensors and environmental factors may also alter sensitivity, leading to inaccuracies in the test results. Excessive bearing clearance might distort vibration signals, further impacting unbalance calculations. Despite these deviations, repeated tests demonstrated consistency with only minor errors, indicating a limited impact on the overall conclusions. However, to ensure reliability, further optimizations are required: improving assembly precision, enhancing sensor accuracy and stability, and strictly controlling environmental conditions. Additional error analysis and refined methodologies will further enhance result accuracy, thereby ensuring the scientific validity and effectiveness of the shot-blasting machine design optimization.

According to the JB/T 3713.2 'Technical Conditions for Double Disc Shot Blasters,' the unbalance should be less than 1.297 g; therefore, reductions were made in both the main disk and secondary disk of the impeller body. While drilling for weight reduction, caution was exercised to avoid excessive loss at specific positions so as not to compromise the structural integrity and strength of the impeller body. Fig. 2 illustrates the modified impeller body, with red circles indicating locations where weight reduction was performed. Subsequent re-testing revealed that after drilling (as depicted in Fig. 3), the main disk exhibited an unbalance of 0.294 g at 288°, while the secondary disk showed an unbalance of 0.316 g at 272°; upon rotation cessation, these values further decreased to 0.272 g and 0.376 g, respectively, all well within the controlled limit of 1.297 g.

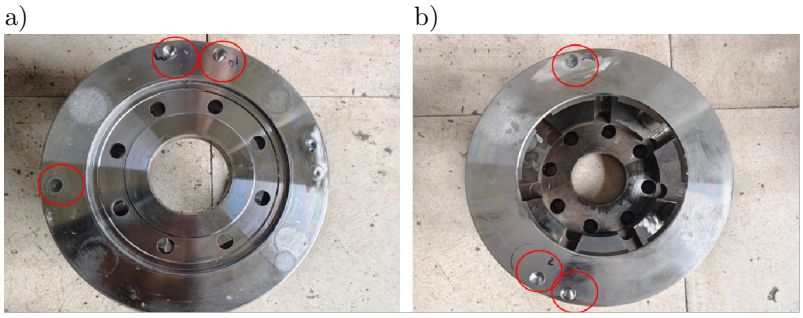

Fig. 2. Evaluation of the primary disk of the impeller body following dynamic balancing (a), examination of the auxiliary disk of the impeller body after dynamic balancing (b).

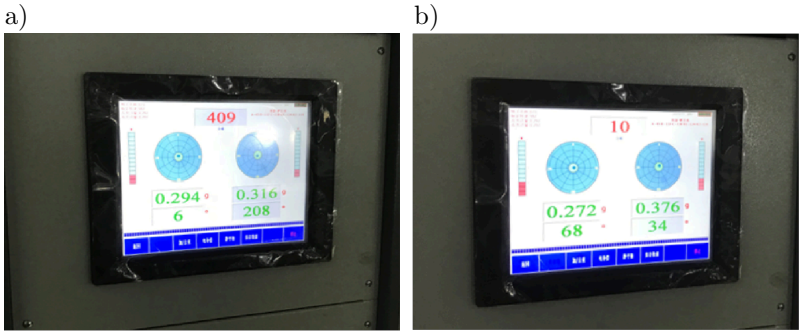

Fig. 3. Residual unbalance of the impeller body during rotation after achieving balance (a), and at rest after achieving balance (b).

The particle velocity of the shot-blasting device was subsequently analyzed using the discrete element method [18–20]. The particle velocity of the shot-blasting device with seven prime-number angular front curved blades reached a maximum value of 75 m/s, with velocity fluctuations within 4 m/s. Furthermore, particles accelerated by the shot-blasting device achieved a relatively stable state after reaching 0.24 s. Through analysis of four other shot-blasting models, it was found that the ejection speed of the eight-uniform front-curved blade is 74 m/s, while for the eight-uniformly distributed straight-blade shot blaster and seven-uniformly distributed straight-blade shot blaster, their ejection speeds were measured at 64 m/s and 69 m/s, respectively. These two types exhibited lower ejection speeds and poorer ejection stability. Similarly, although the seven-uniformly distributed forward-curved blade shot blaster demonstrated a high ejection speed, its stability was also inadequate in comparison. In terms of overall ejection stability among these devices, it can be concluded that the shot-blasting device with seven prime-number angular front-curved blades outperforms the other configurations. Therefore, it is speculated that this particular device will exhibit superior cleaning efficiency during operation.

3. Vibration signal analysis and noise detection of the shot-blasting machine

In order to evaluate the resonance improvement effect and noise optimization of the new shot-blasting device, a comparison was made between the frequency-domain and time-domain signals of the newly designed device and a traditional shot-blasting device. The Hansford's HS-150 acceleration sensor was selected for measuring vibration, with data acquired using the VK701 H model. Vibration data from both devices were collected at a sampling frequency of 10 Ksps, as shown in Fig. 4 and Fig. 5, depicting time-domain analyses before and after op-

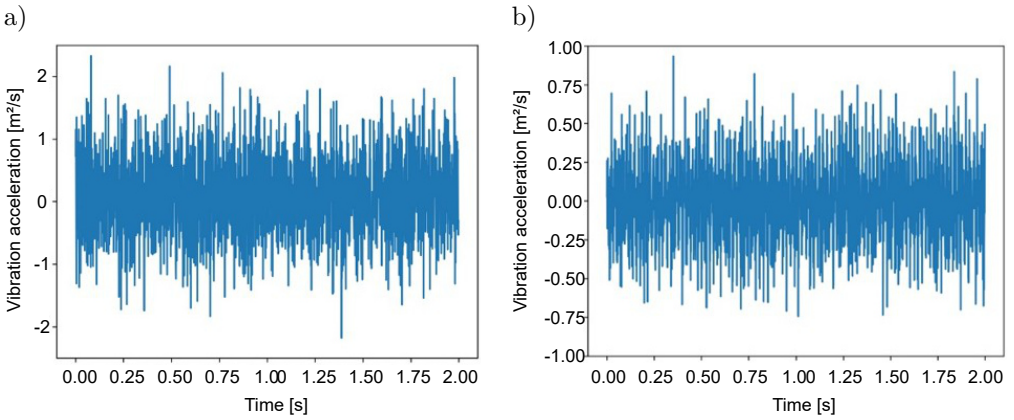

Fig. 4. Time-domain analysis: a) time-domain diagram of position 1 before optimization, b) time-domain diagram of position 2 before optimization.

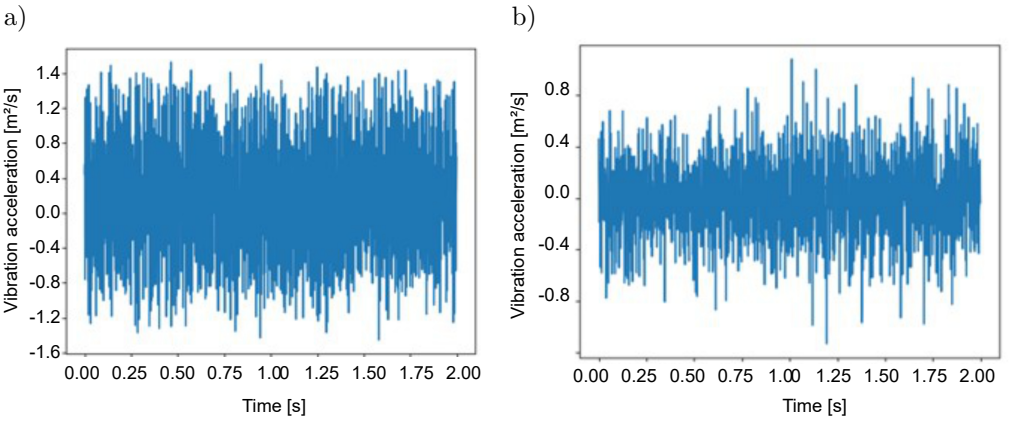

Fig. 5. Time-domain analysis: a) time-domain diagram of position 1 after optimization, b) time-domain diagram of optimized position 2.

timization. Specifically, Fig. 5 presents the vibration acceleration time-domain diagrams of the new shot-blasting device [21–24]. Analysis of the 10 Ksps vibration signal revealed significant improvement in resonance for the Q034ZZ shot blaster: disappearance of the 2nd order component, reduction of amplitude of the 9th order component decreased to approximately 50 % of the fundamental BPF, and overall low amplitude for other frequencies, effectively controlling resonance between the impeller body and motor. Both time-domain and frequency-domain analyses demonstrate a remarkable improvement in the performance of the entire machine [25, 26].

To mitigate the impact of random peaks, vibration intensity was quantified using the root-mean-square (RMS) acceleration within the same 2-seconds window. As depicted in Fig. 4 and Fig. 5, the RMS at position 1 decreased

from $0.800\,\mathrm{m/s^2}$ to $0.467\,\mathrm{m/s^2}$ ($\Delta = 0.333\,\mathrm{m/s^2}$, a reduction of 41.6 %), and at position 2 from $0.283\,\mathrm{m/s^2}$ to $0.217\,\mathrm{m/s^2}$ ($\Delta = 0.067\,\mathrm{m/s^2}$, a reduction of 23.5 %). The reductions in RMS at both measurement points indicate effective suppression of the shot-blasting device's vibration. Thus, the structure designed in accordance with the prime-number/uniform angular-distribution criterion attains a remarkable optimization effect.

In this study, the collected vibration signals are organized into groups, with each group containing 5000 data points. Considering a sampling rate of 10 Ksps, there are a total of 20 groups. Consequently, the fast Fourier transform (FFT) is employed to convert the time-domain signals into frequency-domain signals, as illustrated in Fig. 6 and Fig. 7. To preserve fidelity and comparability with the

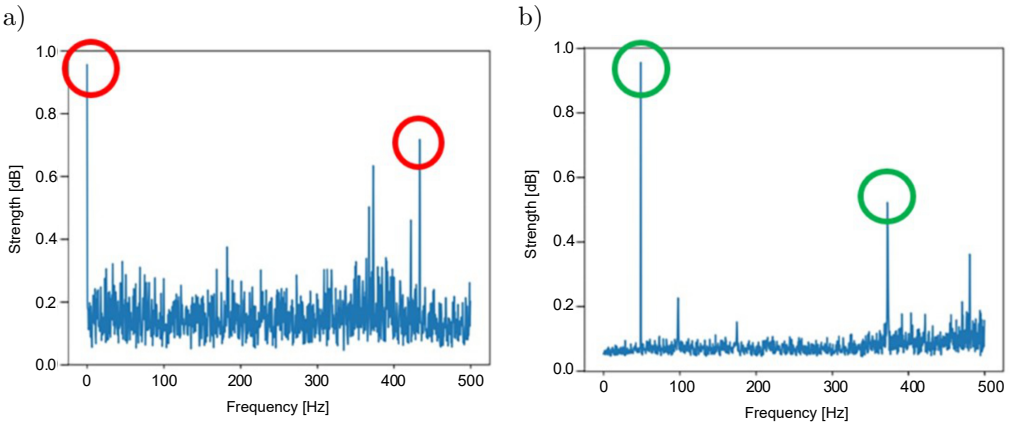

Fig. 6. Frequency domain analysis: a) frequency-domain diagram of the vibration signal at position 1 before optimization, b) frequency-domain diagram of the vibration signal at position 2 before optimization.

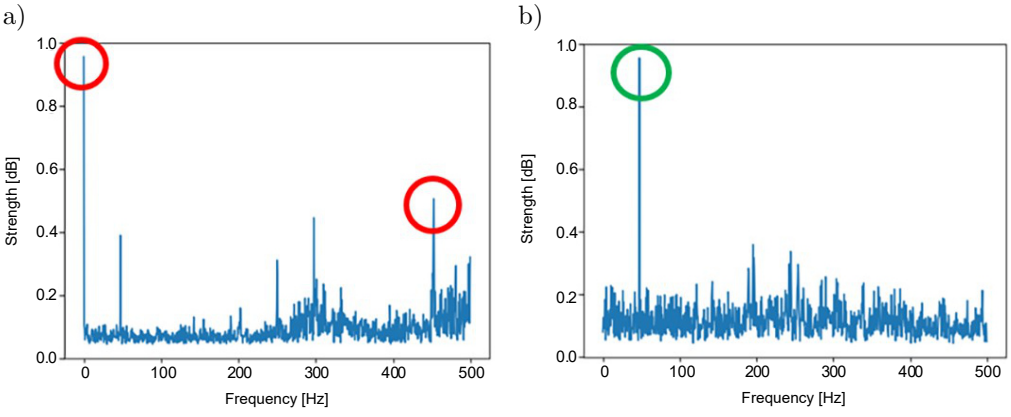

Fig. 7. Frequency-domain analysis: a) frequency-domain diagram of the vibration signal at position 1 after optimization, b) frequency-domain diagram of the vibration signal at position 2 after optimization.

raw measurements, the spectra shown are in their original form, i.e., without additional high-pass filtering or detrending; consequently, the narrow component near 0 Hz in Fig. 6a arises from acquisition-chain offset/slow drift. Moreover, numerous research findings have demonstrated that FFT effectively mitigates data errors; hence, it can be utilized for noise reduction applications in various data-related problems [27–30]. The FFT serves as the foundation for computing the discrete Fourier transform (DFT).

The frequency-domain signals before and after vibration optimization are compared and analyzed. The peaks of the frequency-domain signals before and after optimization are marked with red and green circles, respectively, as depicted in Fig. 6 and Fig. 7. Figure 6a and Fig. 7a present the frequency-domain diagrams at position 1 (radial position) before and after optimization. It can be observed from the diagrams that, under the load state of the shot-blasting machine, the intensity of each blade-passing harmonic order is reduced compared to the second-order blade-passing component. Specifically, the highest value decreases from accounting for 70 % of the fundamental frequency to 50 %, effectively suppressing resonance. On the other hand, Fig. 6b and Fig. 7b depict the frequency-domain diagrams at position 2 (axial position) before and after optimization. It can be seen that each harmonic amplitude improves following optimization with a significant reduction observed in the second-order component – decreasing from representing 50 % of their respective fundamental frequencies to approximately 20 %. Furthermore, in Fig. 7b, it is noteworthy that the other harmonics' highest values account for only 30 % of their corresponding fundamental frequencies indicating a good vibration-reduction effect. In addition, in Fig. 6a, the dominant line occurs at 375 Hz to 380 Hz. With $z = 7$ blades, this line corresponds to the BPF $= zn/60$. Back-calculating the speed gives $n \approx 60 f_{\mathrm{BPF}}/z \approx 3.23$ krpm. Given the frequency resolution used in this study ($\Delta f = 2$ Hz), the resolution-limited uncertainty is about ± 17 rpm. Hence, the peak being higher than the expected 350 Hz at the nominal 3000 rpm is explained by a slightly higher actual speed rather than an analysis artifact. The component near 50 Hz in Fig. 6b originates from mains/electromagnetic coupling and is unrelated to blade orders, whereas the line near 430 Hz in Fig. 6a is a non-integer-order response consistent with a structural or bearing-related mode of the assembly at the measured speed. Both components decrease after optimization, while the BPF-related orders exhibit the largest attenuation.

The optimized impeller structure of the shot blaster has significantly contributed to reducing resonance and minimizing the acceleration value of the vibration signal, as evidenced by the results presented in Fig. 5 and Fig. 7. These findings not only validate the effectiveness of designing the impeller structure based on prime-number/uniform angular distribution criterion for shot blaster blades, but also demonstrate its rationality. This remarkable improve-

ment can be primarily attributed to the seven prime-number angular front-curved blade design, which effectively mitigates resonance and friction between blades, thereby reducing operational vibrations in the shot-blasting machine.

The noise levels of the two shot blasters at 3000 rpm were tested, and the noise levels of the traditional Q034ZZ shot blaster and the newly designed shot blaster based on the blade prime-number/uniform angular distribution criterion were compared. A noise-level meter with a measurement range of 80 dB to 130 dB was used to detect at a distance of one meter to eliminate external interference. The results show that the noise level of the newly designed shot blaster is reduced by 3.7 dB, from 97 dB to 93.3 dB, which proves the effectiveness of the new design in noise reduction.

4. Conclusion

In this paper, a resonance-coupling-reduction-based optimization method was proposed to address the issue of increased vibration in the Q034ZZ shot-blasting machine caused by motor and blade resonance. The geometric limitations of traditional impeller bodies have resulted in scarce optimization methods. This study introduces an innovative prime-number/uniform angular distribution criterion and designs a shot-blasting device with seven prime-number angular front-curved blades based on this principle. The discrete element method was employed to analyze ejection velocity and stability, while drilling the impeller body helped reduce imbalance due to uneven blade distribution. Subsequently, projectile velocity, projectile stability, and vibration signals from the shot-blasting device were explored. It was observed that both the second-order and nine-frequency components exhibit lower amplitude values compared to other frequency multiples, which account for less than 50 % of the fundamental frequency. This represents significant improvement compared to traditional shot-blasting devices, in which such amplitudes exceed 75 %. These findings demonstrate the feasibility of using a seven prime-number angular curved-blade shot-blasting device for vibration and noise reduction purposes. In this experiment, noise measurements were conducted on both the traditional shot-blasting device and the shot-blasting device with seven prime-number angular front-curved blades resulting in a noise reduction from 97 dB (traditional) to 93.3 dB (seven prime-number angular), thus verifying the excellent noise-reduction performance achieved through the design improvements.

Despite these promising results, this study has certain limitations. The optimization method was primarily tested on a single type of shot-blasting machine, and further validation under different configurations and operating conditions is needed. Additionally, although the seven prime-number angular blade design effectively reduces vibration and noise, its impact on other factors, such as en-

ergy efficiency and service life requires further investigation. Future research will address these aspects and extend the methodology to other types of machinery. Nevertheless, the proposed design shows significant promise for applications in industries such as wind power and aerospace. As noise-reduction standards become stringent, the demand for this technology is expected to grow, presenting substantial potential for industrial machinery and environmental protection.

Fundings

This research was funded by Natural Science Foundation of Shandong Province (grant no. ZR2022ME118).

Conflict of interest

The authors declare that they have no known competing financial interests or personal relationships that could have appeared to influence the work reported in this paper.

Authors' contributions

Yong Li: conceptualization, methodology, and writing – original draft preparation. Yaao Di: methodology and writing – review and editing. Wenzheng Dong: validation, resources, and writing – review and editing. Fangxiang Yin: resources and literature survey. Yihao Yin: resources and literature survey. Shanling Han: funding acquisition, writing – review and editing, supervision, and project administration. All authors reviewed and approved the final manuscript.

References

1. Zifeng X., Yan W., Zhihai S., Study on noise reduction of Q400C shot blasting machine [in Chinese], *Modern Manufacturing Technology and Equipment*, **56**(8): 7–8, 2020.
2. Mayers R.A. [Ed.], *Encyclopedia of Physical Science and Technology*, 3rd ed., Academic Press, 2002.
3. Chen W.-K., *Mathematics for Circuits and Filters,* pp. 83–111, CRC Press, Boca Raton, eBook, 2022.
4. Sundararajan D., *Signals and Systems: A Practical Approach*, Springer, Cham, 2022.
5. Sahu O., Das P., Muni M.K., Pradhan N., Basa B., Sahu S.K., Frequency-based crack effect study on beams under free vibration using finite element analysis, *Engineering Transactions*, **72**(1): 95–114, 2024, https://doi.org/10.24423/EngTrans.3166.2024.
6. Zhang X., Yan P., Lu W., Cheng Y., Sun C., Zhu J., Guo W., Cheng X., Frequency spectrum characteristics of blast-induced vibration with electronic detonators in ground

blasting, *Journal of Building Engineering*, **74**: 106892, 2023, https://doi.org/10.1016/j.jobe.2023.106892.

7. Wang Q., Tao T.-J., Jia J., Tian X.-C., Xie C.-J., Analysis of blasting vibration duration considering frequency and energy and its application, *Heliyon*, **10**(12): e33210, 2024, https://doi.org/10.1016/j.heliyon.2024.e33210.

8. Deng Z., Meng J., Deng Y., Ni J., Ye D., Analysis of vibration signals near ground surface during blasting excavation of a tunnel in fractured rock, *Scientific Reports*, **14**: 21909, 2024, https://doi.org/10.1038/s41598-024-73089-1.

9. Guo J., Fei H., Yan Y., Research and advances in the characteristics of blast-induced vibration frequencies, *Buildings*, **15**(6): 892, 2025, https://doi.org/10.3390/buildings15060892.

10. Luo L., Wu Y., Peng Z., Ouyang H., Experimental and numerical study on the noise of uneven-spaced automobile cooling fans [in Chinese], *Noise and Vibration Control*, **41**(5): 175–181, 2021, https://doi.org/10.3969/j.issn.1006-1355.2021.05.028.

11. Zhang Y., Wang S., Pan Y., Zhang T., Jiang Z., Fu X., Research on Optimization design of shot blasting machine blade based on modal analysis [in Chinese], [in:] *2021 Global Reliability and Prognostics and Health Management (PHM-Nanjing)*, 2021, https://doi.org/10.1109/PHM-Nanjing52125.2021.9612963.

12. Wu F., Tang D., Zhao J., Wang B., Luo X., Zhang W., Guo C., Finite element analysis on forward-curve blade of shot blasting machine based on ANSYS [in Chinese], *Mechanical Research & Application*, **28**(03): 27–29, 2015, https://doi.org/10.16576/j.cnki.1007-4414.2015.03.012.

13. Choi D., Kim T., Yang C., Nam J., Park J., Discrete element method and experiments applied to a new impeller blade design for enhanced coverage and uniformity of shot blasting, *Surface and Coatings Technology*, **367**: 262–270, 2019, https://doi.org/10.1016/j.surfcoat.2019.04.008.

14. Zhang D., Liu Y., Wang Z., Analysis of noise by horizontal mobile shot blasting equipment [in Chinese], *Journal of Heilongjiang University of Science*, **2011**(4): 297–300, 2011.

15. Zhou K., Qiao B., Liu M., Gao W., Dai J., Chen X., A novel OPR-free method for blade tip timing based on adaptive variable reference blades, *Aerospace Science and Technology*, **142**(Part B): 108708, 2023, https://doi.org/10.1016/j.ast.2023.108708.

16. Zhang T., Wang S., Yousuf Y.A., Jiang Z., Fang J., Fu X., Men X., Study on the dynamic fatigue performance of shot blasting machine's blades based on modal analysis, *Journal of Physics: Conference Series*, **1948**: 012214, 2021, https://doi.org/10.1088/1742-6596/1948/1/012214.

17. Wang Y., Sun Z., Liu J., Liu M., Zhou Y., Optimization design of centrifugal impeller based on Bezier surface and FFD space grid parameterization, *PLoS ONE*, **19**(11): e0310792, 2024, https://doi.org/10.1371/journal.pone.0310792.

18. Hou L., Yang L.Y., Wang Y.Z., Wang S.R., Kinematics simulation analysis of shots in shot blasting machine based on EDEM, *Applied Mechanics and Materials*, **121–126**: 2071–2074, 2011, https://doi.org/10.4028/www.scientific.net/AMM.121-126.2071.

19. Liu Y., Li Q., Kinetic analysis of shot blasting machine with forward curve blades based on EDEM [in Chinese], *Machine Building & Automation*, **46**(06): 130–132+136, 2017, https://doi.org/10.19344/j.cnki.issn1671-5276.2017.06.036.

20. Yan X.Y., Wang S.R., Wen D.S., Wang G.Q., Kinematics simulation analysis of shot blasting projectile based on EDEM, *DEStech Transactions on Engineering and Technology Research*, 2018, https://doi.org/10.12783/dtetr/pmsms2018/24869.

21. Liss M., Martynyuk V., Vibration analysis of shot wheel in abrasive blasting, *MATEC Web Conferenes*, **375**: 02006, 2023, https://doi.org/10.1051/matecconf/202337502006.

22. Yang Z., Fault diagnosis of engine abnormal sound based on vibration analysis [in Chinese], *Special Purpose Vehicle*, **2024**(09): 109–112, 2024, https://doi.org/10.19999/j.cnki.1004-0226.2024.09.027.

23. Fu X., Huang K., Sidiropoulos N.D., Ma W.-K., Nonnegative matrix factorization for signal and data analytics: Identifiability, algorithms, and applications, *IEEE Signal Processing Magazine*, **36**(2): 59–80, 2019, https://doi.org/10.1109/MSP.2018.2877582.

24. Yang J., Shi A., Peng Y., Peng P., Liu J., Interface state-based bound states in continuum and below-continuum-resonance modes with high-Q factors in the rotational periodic system, *Chinese Physics B*, **33**(8): 084206, 2024, https://doi.org/10.1088/1674-1056/ad4630.

25. Lydakis E., Koss H., Brincker R., Amador S.D.R., Data-driven sensor fault diagnosis for vibration-based structural health monitoring under ambient excitation, *Measurement*, **237**: 115232, 2024, https://doi.org/10.1016/j.measurement.2024.115232.

26. Qiu Z., Fan S., Liang H., Liu J., Multimodal fusion fault diagnosis method under noise interference, *Applied Acoustics*, **228**: 110301, 2025, https://doi.org/10.1016/j.apacoust.2024.110301.

27. Shunxi W., Wenjin H., The characteristics and relationships of FT, ZT, DFS, DFT and FFT transformations, *Practical Electronics*, **2015**(01): 121, 2015, https://doi.org/10.16589/j.cnki.cn11-3571/tn.2015.10.240.

28. Runjie W., Wenzhong S., Xianglei L., Zhiyuan L., An adaptive cutoff frequency selection approach for fast Fourier transform method and its application into short-term traffic flow forecasting, *ISPRS International Journal of Geo-Information*, **9**(12): 731, 2020, https://doi.org/10.3390/ijgi9120731.

29. Yang P., Zhou W., Algorithmic analysis towards time-domain extended source waveform inversion, *Pure and Applied Geophysics*, **181**: 2765–2785, 2024, https://doi.org/10.1007/s00024-024-03556-3.

30. Chen Y., Hou L., Lin R., Song J., Ng T.Y., Chen Y., Corrigendum to "A harmonic balance method combined with dimension reduction and FFT for nonlinear dynamic simulation" [Mech. Syst. Signal Process. 221 (2024) 111758], *Mechanical Systems and Signal Processing*, **223**: 111848, 2025, https://doi.org/10.1016/j.ymssp.2024.111848.

Received July 3, 2025; revised September 17, 2025; accepted September 18, 2025; available online December 11, 2025; version of record March 2, 2026; published issue March 30, 2026.

Engineering Transactions, **74**(1): 85–103, 2026, https://doi.org/10.24423/engtrans.2025.3495
Institute of Fundamental Technological Research Polish Academy of Sciences (IPPT PAN)
Université de Lorraine • Poznan University of Technology

SolMech 2024

On Frequency Dependence of Stability in Materials with Fractional Viscosity

Peter B. Béda

Department of Railway Vehicles and Vehicle System Analysis,
Budapest University of Technology and Economics
Budapest, Hungary; e-mail: beda.peter@kjk.bme.hu

Material instability refers to the tendency of materials to undergo alterations in their properties in loading. The concept of instability is governed by the constitutive equation of solids. Our analysis uses the entire set of equations describing the motion of solids, including the kinematical equation and Cauchy's equations of motion. Damping, or rate-dependence, plays a crucial role in stability. A potential generalization involves the utilization of fractional-order derivatives of the strain or stress tensors. The stability analysis primarily focuses on periodic perturbations. The mechanism of loss of stability on various parts of the stability boundary is under consideration.

Keywords: applied fractional calculus, material instability, dynamical systems.

1. Introduction

When the kinematical concept of stability is adopted, a material state is identified with a solution of the basic equations, and stability properties are studied in terms the stability of solutions of differential equations (dynamical systems) [6]. Material instability (divergence or flutter) [39] occurs well beyond the elastic domain; thus, the form of the constitutive equation might remind viscoelasticity but the physical background is different. This paper does not concentrate on various plasticity theories and does not treat the formulations (or even the existence of) of flow rules or hardening models, which have various interpretations in [21]. These problems are well beyond the scope of this study. Instead, a simplified constitutive equation is used, under the assumption that, after unloading, the body does not regain its original shape.

In physical interpretation static bifurcation (or divergence instability) can be observed as necking or shear banding, which are phenomena of strain localization. Flutter is the dynamic bifurcation and is considered here as the onset of

an oscillation, being observed in plastic flow theory [28, 29], viscoplasticity [14], smeared crack models [43] or serrated flow, called the Portevin–Le Chatelier effect. This study is based on the work of Kubin and Estrin [20], which uses a semi-empirical constitutive law:

$$\sigma = h\varepsilon + \overline{F}\left(\dot{\varepsilon}\right),$$

with negative rate-dependence included in function $\overline{F}$. Here ε and $\dot{\varepsilon}$ denote strain and strain rate, respectively, while σ is the stress in the uniaxial case and h is the work hardening rate. As a phenomenon, flutter instability means the existence of propagating deformation bands. Their work cites many papers based on experimental results on serrated flow, such as [8, 15, 24, 36, 42]. One of the main observations in this studies is that serrated flow appears at negative strain-rates. In this paper, such a model is generalized to a fractional rate.

Bifurcation analysis of a solution is a well-known and widely applied field in nonlinear dynamics. The first step of it starts with a linearization of the system of basic equations at that solution, identified by the state of the material [7]. Then the critical non-trivial eigenspace of the operator is studied. As a further step, the nonlinearities should be projected onto that non-trivial eigenspace to classify the type of bifurcation and describe the post-bifurcation behavior. Two key elements should be mentioned at this point. Firstly, the loss of stability should happen by crossing the imaginary axis by either a real eigenvalue or a pair of complex eigenvalues as the load (the bifurcation parameter) changes quasi-statically [47]. Second, at the critical value of the bifurcation parameter (zero real value of the eigenvalues), the critical eigenspace should be finite-dimensional.

Generally, such studies concern ordinary differential equations with integer-order derivatives. In material instability problems, bifurcation describes the types of instability. These two phenomena are identified as static and dynamic bifurcations. In the static case the loss of (Lyapunov) stability is coupled with a change in the number of solutions [25, 27, 30] while in the dynamic bifurcation a self-sustained oscillation can be observed. In a large range of materials, damping is described by fractional-order derivatives.

The aim of this paper is to perform such an analysis for a set of fractional-order equations. A method is presented to find the material instability condition. Then, a method to calculate the critical eigenvalues leads to conditions for static and dynamic bifurcation, even for fractional dynamical systems.

While fractional calculus has produced many new results and has found more and more applications in mechanics, control, economics, and several fields of science, one might have the feeling that this topic is just a fashionable tool of recent years, with no deep physical necessity. However, its roots have already been present in solid mechanics for more than fifty years and can be tracked back

to the birth of continuum field theory in the middle of the last century. The study of creep and relaxation in Rabotnov's hereditary mechanics [34] is based on integral operators in form of convolutions with a fractional-order kernel, which are equivalent to fractional derivatives [38]. An early application was published by Caputo [9] in viscoelasticity [2, 9, 23] and then even in viscoplasticity [44], as a kind of fractional viscosity or non-local time effect. When non-locality is studied in Eringen's approach [16], similar mathematical tools can be used. Furthermore, non-locality may be extended from non-local time to spatial non-locality using fractional (non-local) derivatives [3].

The appearance of fractional calculus goes back to the origin of calculus by Leibniz and Euler, as a possible generalization. Most of the definitions were given by Liouville, Riemann, and others [22]. Fractional derivatives can be easily deduced from Cauchy's repeated integral formula and its generalization. For the n-th (integer) order, it leads to:

$$ {}_aI_t^n f(t) = \frac{1}{(n-1)!} \int_a^t f(\xi)(t-\xi)^{-n-1} \,\mathrm{d}\xi. $$

The α-th fractional-order generalization is the Riemann–Liouville integral operator ($\alpha < 1$):

$$ {}_aI_t^\alpha f(t) = \frac{1}{\Gamma(\alpha)} \int_a^t f(\xi)(t-\xi)^{\alpha-1} \,\mathrm{d}\xi = \frac{1}{\Gamma(\alpha)} \int_a^t \frac{f(\xi)}{(t-\xi)^{1-\alpha}} \,\mathrm{d}\xi. $$

By taking the derivative of the Riemann–Liouville integral operator:

$$ {}_aD_t^\alpha f(t) = \frac{\mathrm{d}}{\mathrm{d}t} {}_aI_t^\alpha f(t) = \frac{1}{\Gamma(1-\alpha)} \frac{\mathrm{d}}{\mathrm{d}t} \int_a^t f(\xi)(t-\xi)^{-\alpha} \,\mathrm{d}\xi, \tag{1.1} $$

the Riemann–Liouville derivative is obtained for the interval $[a, t]$.

By changing operators of differentiation and integration Caputo's derivative is defined:

$$ {}_a^C D_t^\alpha f(t) = {}_aI_t^\alpha \left(\frac{\mathrm{d}}{\mathrm{d}\xi} f \right)(t) = \frac{1}{\Gamma(1-\alpha)} \int_a^t \frac{\mathrm{d}f(\xi)}{\mathrm{d}\xi} (t-\xi)^{-\alpha} \,\mathrm{d}\xi, \tag{1.2} $$

for the interval $[a, t]$.

From [18], the connection between derivatives (1.1) and (1.2) is

$$ {}_aD_t^\alpha f(t) = \frac{1}{\Gamma(1-\alpha)} \frac{f(a)}{(t-a)^\alpha} + {}_a^C D_t^\alpha f(t)\,. \tag{1.3} $$

In several cases, called the full-memory assumption in applications, the starting time is zero, $a = 0$, and the notations are simply $D_t^\alpha f(t)$ and ${}^C D_t^\alpha f(t)$. At this point only the most important definitions are given; more details can be found in several monographs [10, 12, 33, 40, 46].

The method is mainly analytic, using Fourier transformation. It is restrictive compared to numerical analysis [27, 30, 47], and excludes, for example, short-memory effects [45, 48]. However, it allows deeper insight into the roots of unstable behavior, especially at dynamic bifurcation. For the same reason, only the uniaxial case is studied. In 3D problems, the orientation of shear bands is a key factor [29, 31, 39], which requires detailed investigation of the constitutive acoustic tensor, already at the level of static bifurcation analysis. Then, the 3D fractional generalization of continuum mechanics constitutes another wide field of research [13].

2. Rate dependence and material instability

This section explains why a rate-independent constitutive equation is not suitable in material instability problems. Firstly, a rate-independent material, with the constitutive equation

$$F(\sigma, \varepsilon) = 0 \tag{2.1}$$

is studied to point out its singular behavior at instability. Here, F is a general form of the constitutive function. Assume that a uniaxial problem is studied, and the linearized constitutive equation is simply in the form:

$$\sigma = C\varepsilon, \tag{2.2}$$

where

$$C := -\left(\frac{\partial F}{\partial \varepsilon}\right)\left(\frac{\partial F}{\partial \sigma}\right)^{-1}$$

denotes the tangent stiffness. Now, the equation of motion, the kinematic equation, and the so-called rate form of Eq. (2.2) are:

$$\dot{v} = \frac{1}{\rho}\frac{\partial \sigma}{\partial x}, \tag{2.3}$$

$$\dot{\varepsilon} = \frac{\partial v}{\partial x}, \tag{2.4}$$

$$\dot{\sigma} = \left(\frac{\partial F}{\partial \varepsilon}\right)\left(\frac{\partial F}{\partial \sigma}\right)^{-1}\dot{\varepsilon}, \tag{2.5}$$

where ρ denotes the mass density, and v is the velocity field.

By taking the time derivative of Eq. (2.3):

$$\ddot{v} = \frac{1}{\rho}\frac{\partial \dot{\sigma}}{\partial x}, \tag{2.6}$$

the gradient of Eq. (2.4):

$$\frac{\partial \dot{\varepsilon}}{\partial x} = \frac{\partial^2 v}{\partial x^2}, \tag{2.7}$$

and the gradient of Eq. (2.5):

$$\frac{\partial \dot{\sigma}}{\partial x} = \left(\frac{\partial F}{\partial \varepsilon}\right)\left(\frac{\partial F}{\partial \sigma}\right)^{-1}\frac{\partial \dot{\varepsilon}}{\partial x}. \tag{2.8}$$

By substituting Eq. (2.6) and Eq. (2.7) into Eq. (2.8), one obtains:

$$\rho\ddot{v} = \left(\frac{\partial F}{\partial \varepsilon}\right)\left(\frac{\partial F}{\partial \sigma}\right)^{-1}\frac{\partial^2 v}{\partial x^2}. \tag{2.9}$$

By introducing new variables:

$$y_1 = v, \tag{2.10}$$

$$y_2 = \dot{v}. \tag{2.11}$$

Equation (2.9) can be written formally as a dynamical system [7]:

$$\frac{\mathrm{d}}{\mathrm{d}t}\begin{bmatrix} y_1 \\ y_2 \end{bmatrix} = \begin{bmatrix} 0 & 1 \\ \left(\left(\dfrac{\partial F}{\partial \varepsilon}\right)\left(\dfrac{\partial F}{\partial \sigma}\right)^{-1}\dfrac{\partial^2}{\partial x^2}\right) & 0 \end{bmatrix}\begin{bmatrix} y_1 \\ y_2 \end{bmatrix}, \tag{2.12}$$

and the stability of a material state is studied, Eq. (2.12) is applied to small perturbations of the form:

$$\begin{bmatrix} \widetilde{y_1} \\ \widetilde{y_2} \end{bmatrix} = \begin{bmatrix} \widetilde{y_{10}} \\ \widetilde{y_{20}} \end{bmatrix}\exp(\omega x)\exp(\lambda t).$$

Then, Eq. (2.12) reads:

$$\lambda\begin{bmatrix} \widetilde{y_{10}} \\ \widetilde{y_{20}} \end{bmatrix}\exp(\omega x)\exp(\lambda t) = \begin{bmatrix} 0 & 1 \\ \left(\left(\dfrac{\partial F}{\partial \varepsilon}\right)\left(\dfrac{\partial F}{\partial \sigma}\right)^{-1}\omega^2\right) & 0 \end{bmatrix}\begin{bmatrix} \widetilde{y_{10}} \\ \widetilde{y_{20}} \end{bmatrix}\exp(\omega x)\exp(\lambda t).$$

Now, the characteristic equation of (2.12) has the form:

$$\begin{vmatrix} -\lambda & 1 \\ \left(\left(\frac{\partial F}{\partial \varepsilon}\right)\left(\frac{\partial F}{\partial \sigma}\right)^{-1}\omega^2\right) & -\lambda \end{vmatrix} = 0. \tag{2.13}$$

From Eq. (2.13):

$$\lambda^2 - \left(\frac{\partial F}{\partial \varepsilon}\right)\left(\frac{\partial F}{\partial \sigma}\right)^{-1}\omega^2 = 0. \tag{2.14}$$

Now, the stability condition is $\operatorname{Re}\lambda < 0$, for all solutions of Eq. (2.14). The two generic [1] instabilities are the static (at $\lambda = 0$) or the dynamic one (at $\lambda_{1,2} = \pm i\beta$), when a real eigenvalue, or a pair of imaginary eigenvalues reach the stability boundary. In non-linear studies, such cases are referred to as static and dynamic bifurcations.

In the first study, the tangent stiffness $c' := \left(\frac{\partial F}{\partial \varepsilon}\right)\left(\frac{\partial F}{\partial \sigma}\right)^{-1}$ acts as a bifurcation parameter. In the case

$$c' < 0, \tag{2.15}$$

Eq. (2.14) has a pair of pure imaginary roots:

$$\lambda_{1,2} = \pm i\omega\sqrt{-c'}.$$

When $c' > 0$, Eq. (2.14) has one positive and one negative real roots:

$$\lambda_{1,2} = \pm\omega\sqrt{c'},$$

while at $c' = 0$, a double zero eigenvalue is obtained.

Such a way of loss of stability of a dynamical system is a highly degenerate one. Firstly, at Eq. (2.15), no stability (by Lyapunov's definition) is present. In the theory of dynamical systems a situation like this is referred to as the stability boundary, or neutral state of the system. Thus, for the constitutive Eq. (2.2), no stable state can be found, which contradicts all real-life experiences. Moreover, for such a material model, a co-existent degenerate static and dynamic bifurcation can be recognized and no critical eigenvector can be defined for the critical eigenvalues [7]. Thus, the material model (Eq. (2.2)) cannot be used in material instability analysis, and rate-dependent terms should be added [28], and new variables should appear in the constitutive function F in Eq. (2.1):

$$F(\sigma, \dot{\sigma}, \varepsilon, \dot{\varepsilon}) = 0.$$

For example, a linearized form

$$\frac{\partial F}{\partial \dot{\sigma}}\dot{\sigma} + \frac{\partial F}{\partial \sigma}\sigma = \frac{\partial F}{\partial \dot{\varepsilon}}\dot{\varepsilon} + \frac{\partial F}{\partial \varepsilon}\varepsilon,$$

or simply

$$a_1\dot{\sigma} + a_2\sigma = a_3\dot{\varepsilon} + a_4\varepsilon, \tag{2.16}$$

should be used in stability analysis, where the coefficients a_1, a_2, a_3, a_4 denote the partial derivatives of the constitutive function.

3. Material model with fractional derivatives

Several studies have dealt with connecting the hereditary approach of creep and relaxation [34] to rate-dependence [19, 37] and proved the equivalence of the two. When a 'fractional-order rate,' with the Riemann–Liouville or Caputo derivative $D_t^\alpha \;\; 0 < \alpha < 1$, is used:

$$\sum_{i=0}^{n} a_i D_t^{\alpha_i}\varepsilon = \sum_{j=0}^{n} b_j D_t^{\alpha_j}\sigma \tag{3.1}$$

is obtained instead of Eq. (2.16). Remark that such form of the constitutive equation is a generalization of Bagley's viscoelastic material [4, 5]. However, it is important to note that material instability is outside of the domain of elastic deformation.

For stability analysis, Eq. (2.3) and Eq. (2.4) should be transformed into the velocity field. In view of Eq. (2.16) and Eq. (3.1), assume that the constitutive equation is

$$\sigma = E_0\varepsilon + E_1 D_t^\alpha \varepsilon, \tag{3.2}$$

where E_0 is the tangent stiffness and E_1 is the fractional-rate sensitivity parameter. After differentiation

$$\dot{\sigma} = E_0\dot{\varepsilon} + E_1 D_t^\alpha \dot{\varepsilon}. \tag{3.3}$$

By taking its 'gradient' (derive with respect to x):

$$\frac{\partial \dot{\sigma}}{\partial x} = \left(E_0 + E_1 D_t^\alpha\right)\frac{\partial \dot{\varepsilon}}{\partial x}. \tag{3.4}$$

From Eq. (2.6) and Eq. (2.7):

$$\rho\ddot{v} = \left(E_0 + E_1 D_t^\alpha\right)\frac{\partial^2 v}{\partial x^2}. \tag{3.5}$$

By using the harmonic perturbation technique:

$$\widetilde{v} = \widetilde{v}_0 v_t(t) \exp(i\omega x),$$

for Eq. (3.5), and by using the notation D_t^2 for the second time derivative, Eq. (3.5) is equivalent to:

$$D_t^2 v_t + \frac{E_1}{\rho}\omega^2 D_t^\alpha v_t + \frac{E_0}{\rho}\omega^2 v_t = 0. \tag{3.6}$$

In Eq. (3.6), homogeneous perturbations are used, thus $v_t(0) = 0$. From Eq. (1.3), the notation

$$D_t^\alpha v_t := {}_0D_t^\alpha v_t = {}_0^C D_t^\alpha v_t$$

is justified, in Eq. (3.1) and Eq. (3.2) and later.

Stability analysis can be performed as in [11, 26, 32] and in Radwan's research [35]. By performing a Laplace transformation, the characteristic equation of (3.6) reads:

$$s^2 + \frac{E_1}{\rho}\omega^2 s^\alpha + \frac{E_0}{\rho}\omega^2 = 0. \tag{3.7}$$

Then, by following the method in [35], the transformation $W = s^{\frac{1}{m}}$ is used, where $\alpha = \frac{k}{m}$ is rational. Then, Eq. (3.7) takes the form:

$$W^{2m} + \frac{E_1}{\rho}\omega^2 W^k + \frac{E_0}{\rho}\omega^2 = 0. \tag{3.8}$$

The procedure is based on the fact that the imaginary axes of the s-plane are mapped onto lines:

$$|W_\theta| = \frac{\pi}{2m}, \tag{3.9}$$

where W_θ denotes the argument of W in the complex plane ($\arg(W)$). In Fig. 1, the stability map is presented, while Fig. 2 shows the location of the static bifurcation (at the origin) and the lines of dynamic bifurcation. The system will be stable, if and only if all roots of Eq. (3.8) in the W-plane lie in the region:

$$|W_\theta| > \frac{\pi}{2m}, \tag{3.10}$$

thus, the stability condition reads:

$$\min \arg(W) > \frac{\pi}{2m}.$$

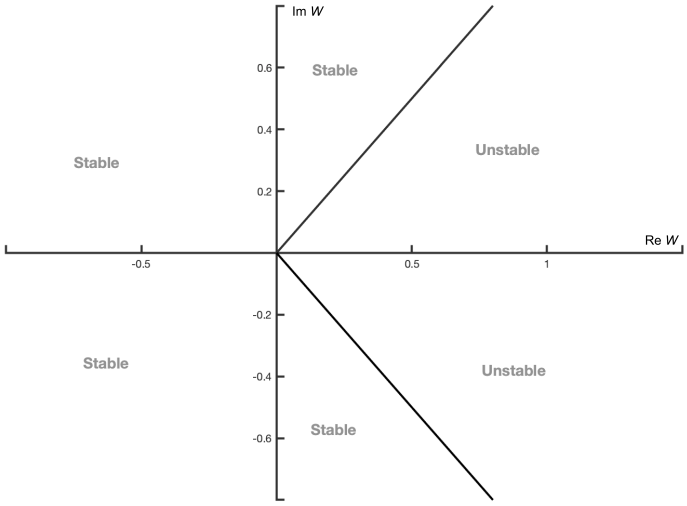

FIG. 1. Domains of stability.

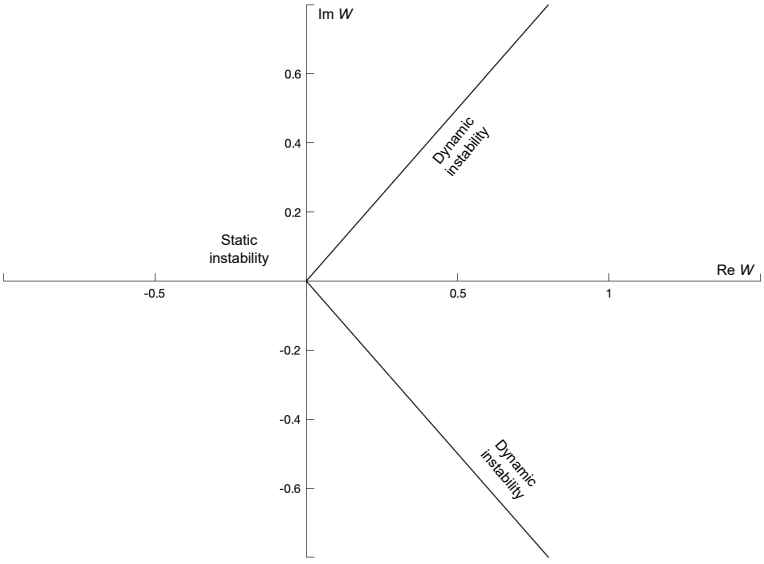

FIG. 2. Static and dynamic instability boundaries.

Now, static instability happens at $W_{cr\,s} = 0$, and its condition from Eq. (3.8) is

$$E_0 = 0. \tag{3.11}$$

Unfortunately, no critical eigenfunction can be attached to this zero eigenvalue from the periodic perturbation functions, so nonlinear analysis cannot be performed.

The dynamic instability condition can also be derived. At dynamic instability, the critical solution $W_{cr\,1,2}$ should lie on the stability boundary lines, thus Eq. (3.9) should be satisfied:

$$W(r) = r\left(\cos\left(\frac{\pi}{2\,m}\right) \pm \sin\left(\frac{\pi}{2\,m}\right) i\right), \quad r \geq 0. \tag{3.12}$$

Now, $W(r)$ from Eq. (3.12) should be substituted into the integer-order characteristic equation (Eq. (3.8)):

$$\left(r\left(\cos\left(\frac{\pi}{2\,m}\right) + \sin\left(\frac{\pi}{2\,m}\right) i\right)\right)^{2\,m} + a_0\,\omega^2 + a_1\,\omega^2\left(r\left(\cos\left(\frac{\pi}{2\,m}\right) + \sin\left(\frac{\pi}{2\,m}\right) i\right)\right)^k = 0,$$

where $a_0 = \frac{E_0}{\rho}$ and $a_1 = \frac{E_1}{\rho}$.

After proper rearrangements:

$$r^{2m}\cos\pi + a_0\,\omega^2 + a_1\,\omega^2\,r^k\left(\cos\left(\frac{\pi}{2\,m}\right) + \sin\left(\frac{\pi}{2\,m}\right) i\right)^k = 0. \tag{3.13}$$

From the imaginary part of Eq. (3.13) $a_1 = 0$ is obtained; thus, the dynamic instability condition is

$$E_1 = 0. \tag{3.14}$$

The critical radius at dynamic instability can be calculated from Eq. (3.13):

$$-r^{2m} + a_0\,\omega^2 = 0 \quad \Rightarrow r = \left(a_0\,\omega^2\right)^{\frac{1}{2m}}, \tag{3.15}$$

and is plotted in Fig. 3 (continuous line $m = 2$, dashed line $m = 4$, dotted line $m = 8$). From Eq. (3.15), we can see that by increasing the frequency ω of the perturbation, the radius of the critical eigenvalue increases. On the other hand, the results show that dynamic instability is a material instability, while condition Eq. (3.14) applies only to the material property E_1.

Moreover, dynamic instability can be treated as a generic bifurcation, which means that it is different from static instability and for the critical eigenfunction:

$$v(x) = \exp\left(i\omega x\right),$$

the critical eigenvalue is

$$W_{cr\,1,2} = \left(a_0\,\omega^2\right)^{\frac{1}{2m}}\left(\cos\left(\frac{\pi}{2\,m}\right) \pm \sin\left(\frac{\pi}{2\,m}\right) i\right).$$

In such a case, a non-linear stability analysis is possible by projecting into the non-trivial critical eigenspace. This result differs from the static instability case. We might state that the constitutive Eq. (3.2) can be used in dynamic bifurcation analysis, but not in static bifurcation analysis.

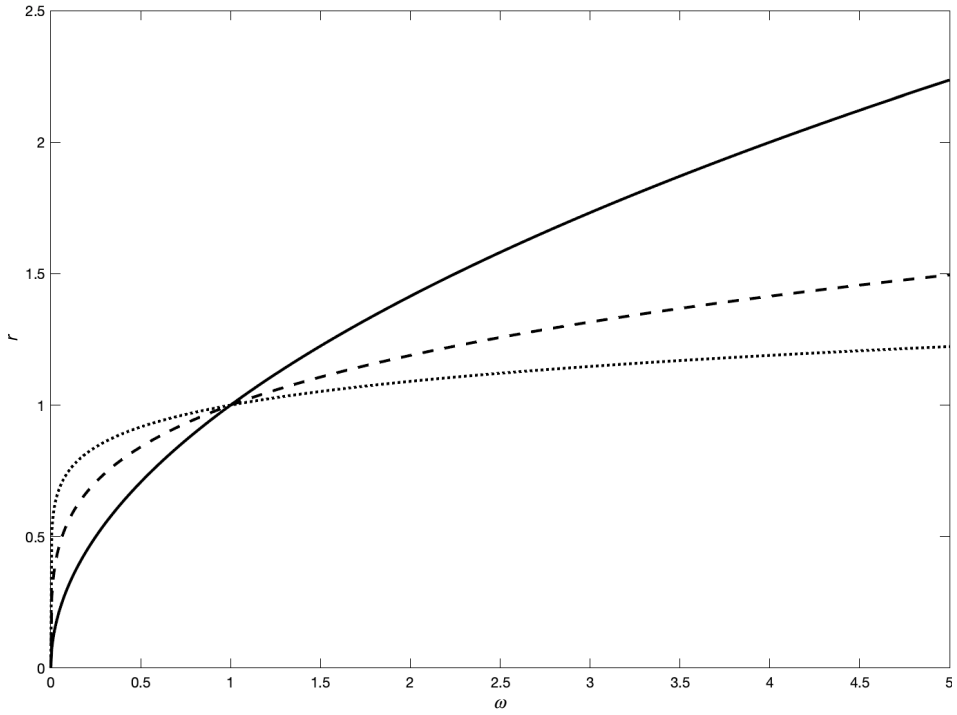

FIG. 3. Critical radius at dynamic instability for $m = 2, 4, 8$.

4. EIGENVALUE DISTRIBUTION PLOTS

To demonstrate the results, by solving Eq. (3.8) numerically for W, the solutions are plotted in Fig. 4 to Fig. 6. In all figures, 8 eigenvalues are marked with dots in the $\operatorname{Re} W$, $\operatorname{Im} W$ plane because the order of the derivative was selected as $\alpha = 0.25$. Two periodic perturbation frequencies ($\omega = 0.3$ and $\omega = 0.8$) are selected in each figures.

In Fig. 4, both parameters are positive, $a_0 > 0$, $a_1 > 0$; consequently, all eigenvalues are in the stability domain for both frequencies. Here, the radii of the eigenvalues increase as ω gets larger, but this has no significant effect on their location. The same observation holds for Fig. 5 at $a_0 > 0$, $a_1 < 0$, but here the material is in an unstable state, which can also be detected from the presence of a pair of eigenvalues in the unstable region.

In Fig. 6, the eigenvalue distributions are plotted at the loss of stability parameters. In Fig. 6a, the material parameter $a_0 = 0$, which shows static-type instability. Then, all eigenvalues are in the stable domain except one zero eigenvalue. In Fig. 6b, one pair of eigenvalues lies on the stability boundary under the $a_1 = 0$ dynamic instability condition. Figure 7 shows two types of unstable cases called static and dynamic post-bifurcations. Here, the situations 'after' the

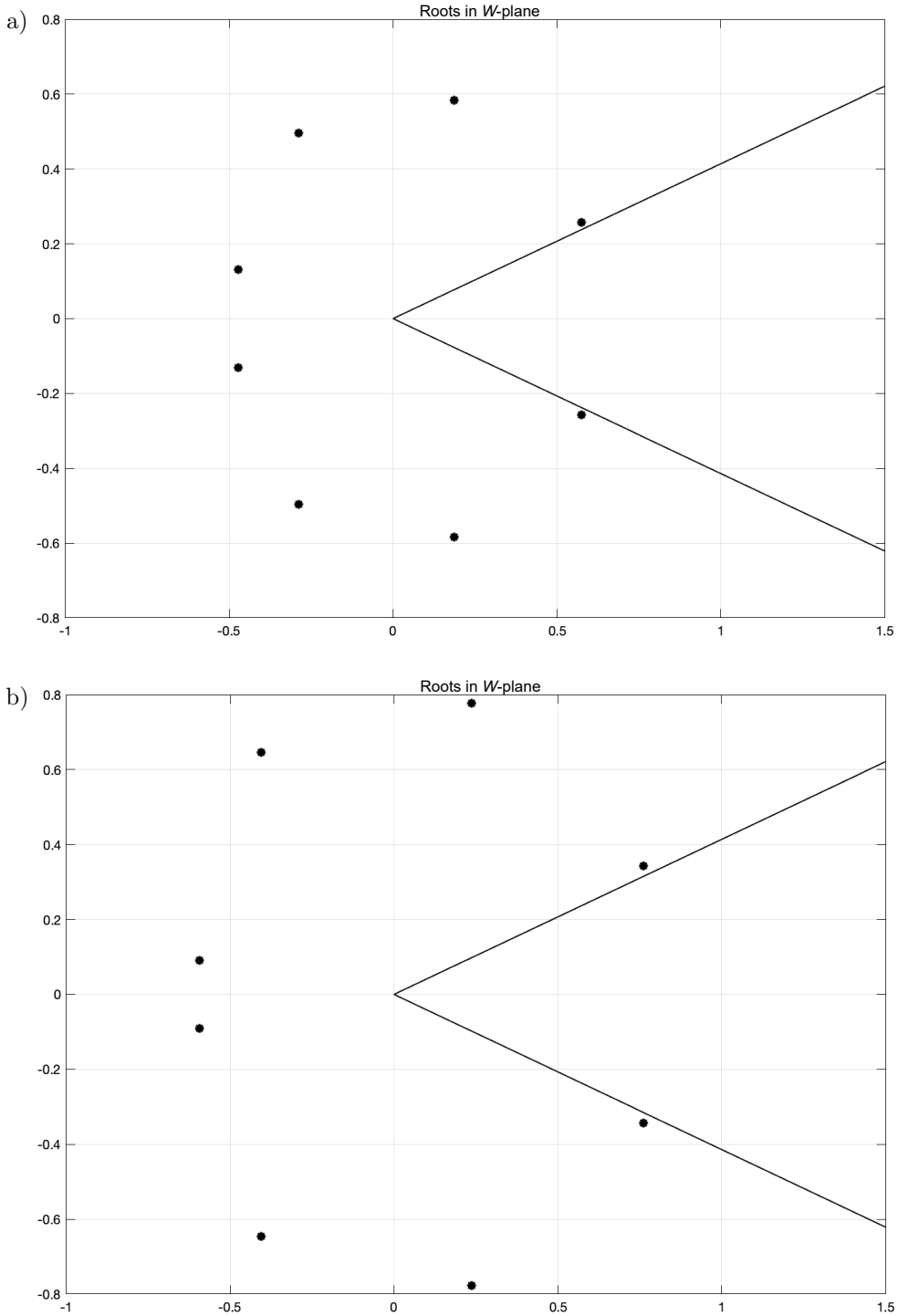

FIG. 4. Eigenvalue distribution in stable state, $E_0 > 0$, $E_1 > 0$: a) $\omega = 0.3$, b) $\omega = 0.8$.

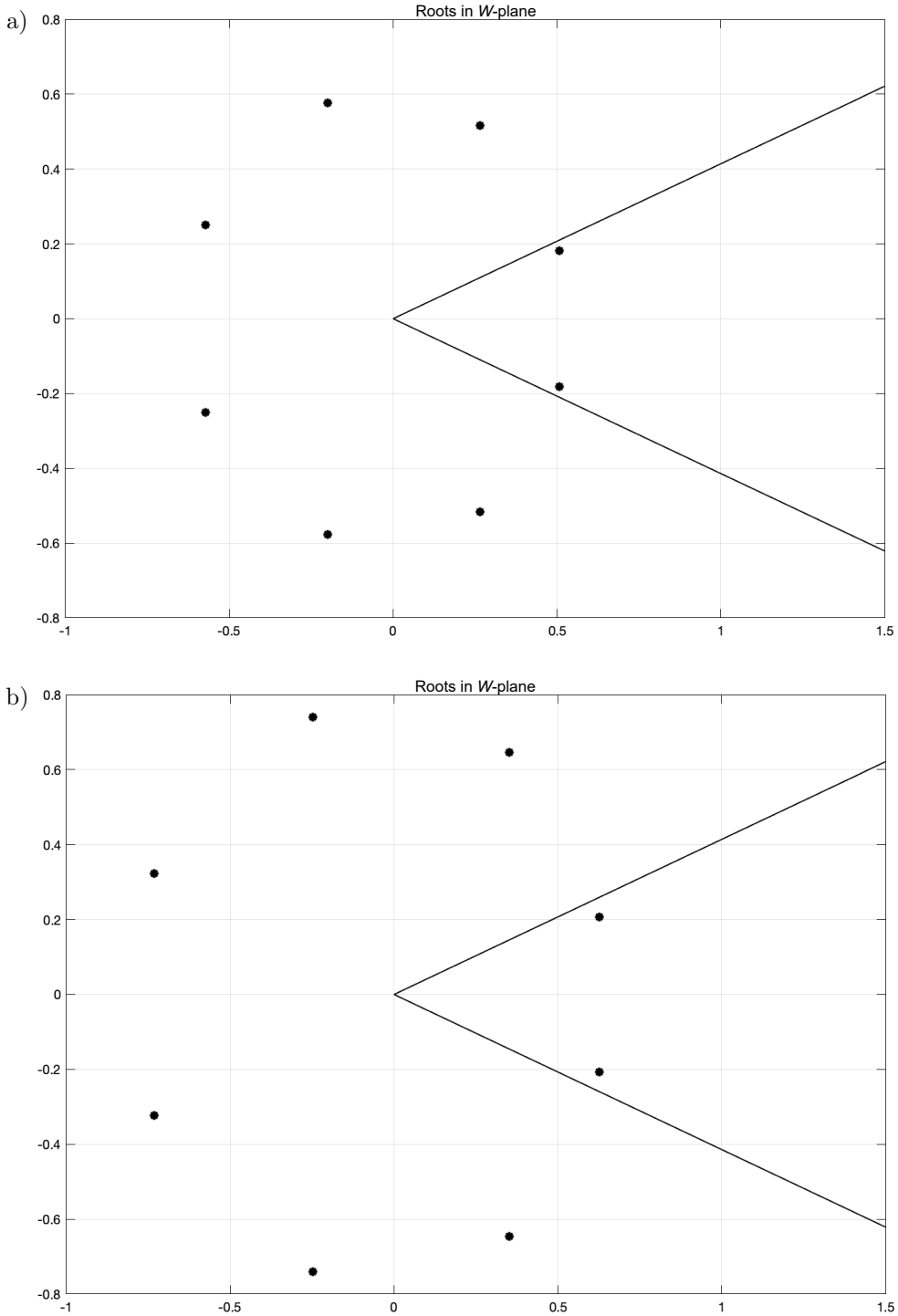

FIG. 5. Eigenvalue distribution in unstable state, $E_0 > 0$, $E_1 < 0$: a) $\omega = 0.3$, b) $\omega = 0.8$.

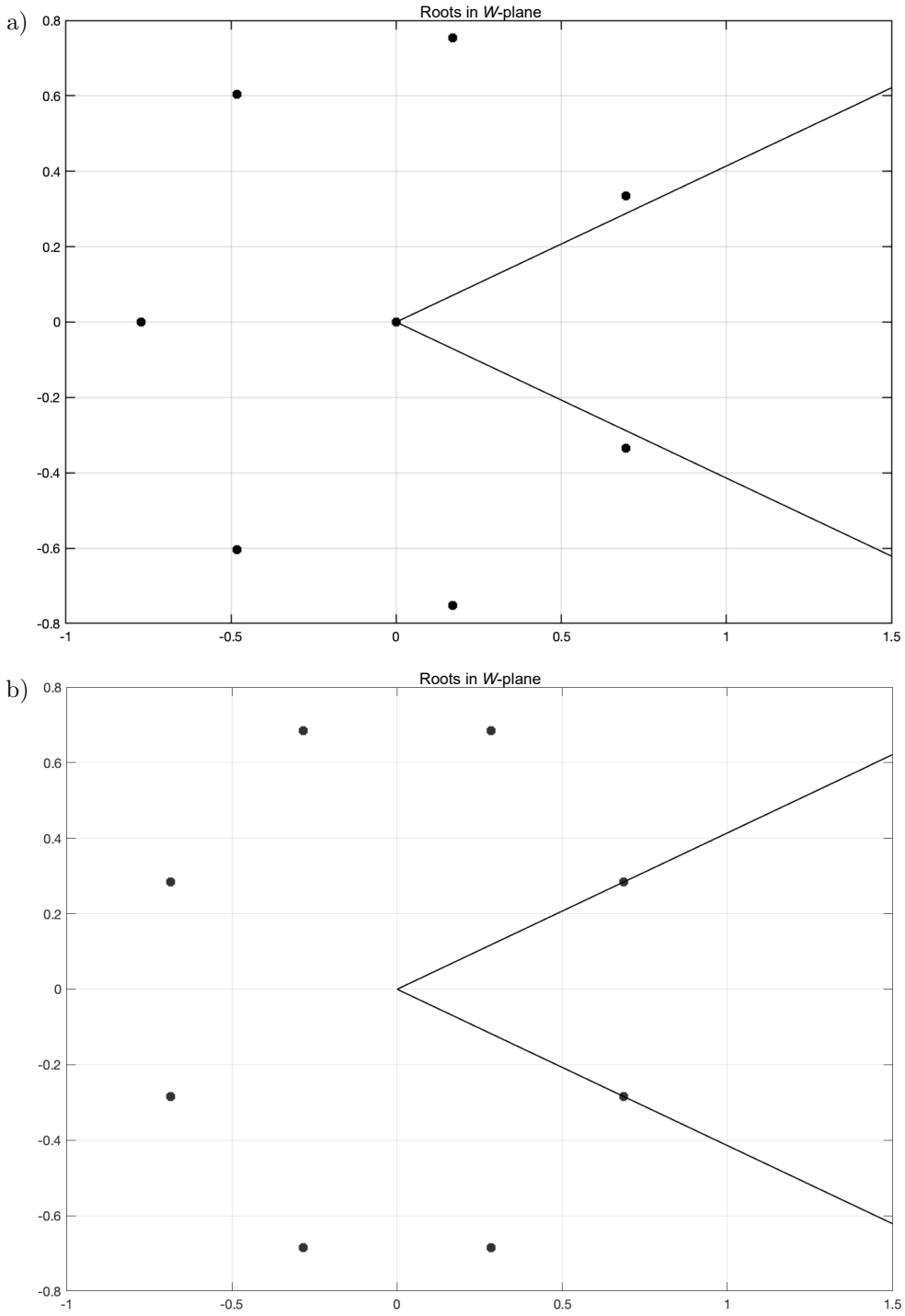

FIG. 6. Eigenvalues at loss of stability:
a) $a_0 = 0$ static bifurcation, b) $a_1 = 0$ dynamic bifurcation.

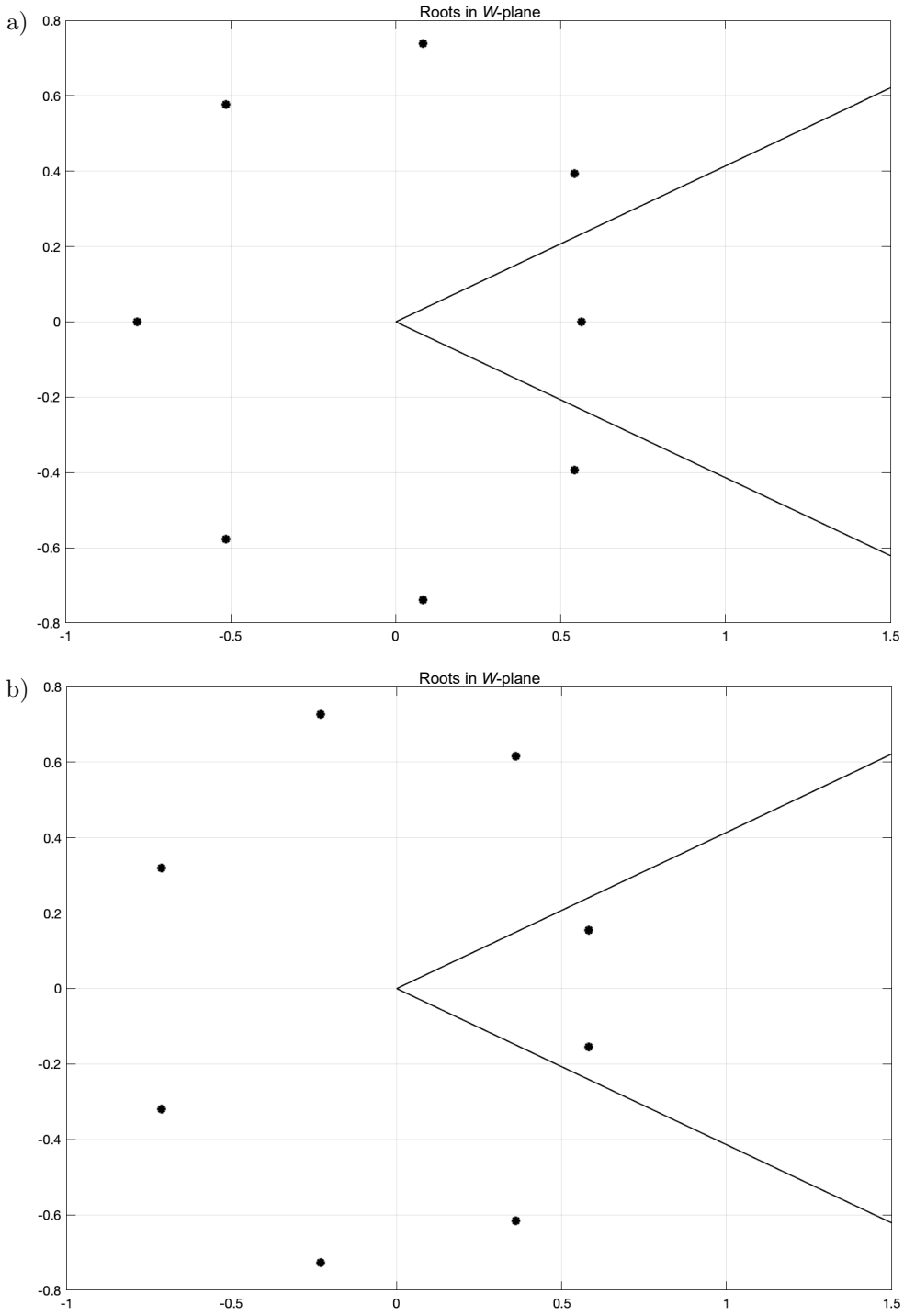

FIG. 7. Eigenvalues after loss of stability:
a) static post-bifurcation, b) dynamic post-bifurcation.

loss of stability are presented, that is, in plot (a) the material parameter a_0 is infinitesimally less than zero, while in plot (b) the material parameter a_1 is infinitesimally less than zero. In both cases, the state is unstable, but plot (a) may correspond to shear banding or necking instabilities [39], while plot (b) describes propagative material instabilities [17] as in Portevin–Le Chatelier effect [20].

5. Conclusion

Fractional derivatives can be and are already used to describe non-conventional rate dependence. When periodic perturbations are applied to stability investigations, they have no effect on stability conditions, which are determined by the material parameters only. This result is the same as in classical case. This result is in line with what is expected from classical theory, while the way of approximation should not affect the outcome of material instability investigation. Frequency acts on the absolute value of eigenvalues, which has no consequences on qualitative behavior. The most important result achieved is that at dynamic instability, the frequency defines critical eigenfunctions to the eigenvalues at the stability boundary. Thus a non-linear study can be performed by projecting the equations to the non-trivial critical null-space spanned by such critical eigenfunctions.

Fundings

This research did not receive any specific grant from funding agencies in the public, commercial, or not-for-profit sectors.

Conflict of interest

The author declares that he has no known competing financial interests or personal relationships that could have appeared to influence the work reported in this paper.

Author's contribution

The author reviewed and approved the final manuscript.

References

1. Arnold V.I., *Geometrical Methods in the Theory of Ordinary Differential Equations*, Springer, New York, 1983.

2. Atanackovic T.M., Stankovic B., Dynamics of a viscoelastic rod of fractional derivative type, *ZAMM – Journal of Applied Mathematics and Mechanics*, **82**(6): 377–386, 2002, https://doi.org/10.1002/1521-4001(200206)82:6<377::AID-ZAMM377>3.0.CO;2-M.

3. Atanackovic T.M., Stankovic B., Generalized wave equation in nonlocal elasticity, *Acta Mechanica*, **208**(1): 1–10, 2009, https://doi.org/10.1007/s00707-008-0120-9.

4. Bagley R.L., *Applications of generalized derivatives to viscoelasticity*, Ph.D. Thesis, USA Air Force Institute of Technology, 1979.

5. Torvik P.J., Bagley R.L., On the appearance of the fractional derivative in the behavior of real materials, *Journal of Applied Mechanics*, **51**(2): 294–298, 1984, https://doi.org/10.1115/1.3167615.

6. Béda P.B., Material instability in dynamical systems, *European Journal of Mechanics, A/Solids*, **16**(3): 501–513, 1997.

7. Béda P.B., Dynamic systems, rate and gradient effects in material instability, *International Journal of Mechanical Sciences*, **42**(11): 2101–2114, 2000, https://doi.org/10.1016/S0020-7403(00)00007-2.

8. Bodner S.R., The mechanics of repeated discontinuous yielding of metals, *Materials Science and Engineering*, **2**(4): 213–223, 1967, https://doi.org/10.1016/0025-5416(67)90061-4.

9. Caputo M., Linear model of dissipation whose Q is almost frequency independent – II, *Geophysical Journal International*, **13**(5): 529–539, 1967, https://doi.org/10.1111/j.1365-246X.1967.tb02303.x.

10. Chen W., Sun H.G., Li X., *Fractional Derivative Modeling in Mechanics and Engineering*, Springer, Singapore, 2022.

11. Deng W., Li Ch., Lu J., Stability analysis of linear fractional differential system with multiple time delays, *Nonlinear Dynamics*, **48**(4): 409–416, 2007, https://doi.org/10.1007/s11071-006-9094-0.

12. Diethelm K., *The Analysis of Fractional Differential Equations*, Springer, Heidelberg, 2010.

13. Drapaca C.S., Sivaloganathan S.A., Fractional model of continuum mechanics, *Journal of Elasticity*, **107**(2): 105–123, 2012, https://doi.org/10.1007/s10659-011-9346-1.

14. Dobovsek I., Adiabatic material instabilities in rate-dependent solids, *Archives of Mechanics*, **46**: 893–936, 1994.

15. Elam C.F., The influence of rate of deformation on the tensile test with special reference to the yield point in iron and steel, *Proceedings A*, **165**(923): 568–592, 1938, https://doi.org/10.1098/rspa.1938.0077.

16. Eringen A.C., Vistas of nonlocal continuum physics, *International Journal of Engineering Science*, **30**(10): 1551–1565, 1992, https://doi.org/10.1016/0020-7225(92)90165-D.

17. Estrin Y., Kubin L.P., Aifantis E.C., Introductory remarks to the viewpoint set on propagative plastic instabilities, *Scripta Metallurgica et Materialia*, **29**(9): 1147–1150, 1993, https://doi.org/10.1016/0956-716X(93)90100-7.

18. Kilbas A.A., Srivastava H.M., Trujillo J.J. [Eds], *Theory and Applications of Fractional Differential Equations*, Elsevier, Amsterdam, 2006.

19. Koeller R.C., Applications of fractional calculus to the theory of viscoelasticity, *Journal of Applied Mechanics*, **51**(2): 299–307, 1984, https://doi.org/10.1115/1.3167616.

20. Kubin L.P., Estrin Y., The Portevin–Le Chatelier effect in deformation with constant stress rate, *Acta Metallurgica*, **33**(3): 397–407, 1985, https://doi.org/10.1016/0001-6160(85)90082-3.

21. Lubliner J., *Plasticity Theory*, Macmillan Publishing Company, New York, 1990.

22. Machado J.T., Kiryakova V., Mainardi F., Recent history of fractional calculus, *Communications in Nonlinear Science and Numerical Simulation*, **16**(3): 1140–1153, 2011, http://doi.org/10.1016/j.cnsns.2010.05.027.

23. Mainardi F., *Fractional Calculus and Waves in Linear Viscoelasticity*, Imperial College Press, London, 2010, https://doi.org/10.1142/p614.

24. Manjoine M.J., Influence of rate of strain and temperature on yield stresses of mild steel, *Journal of Applied Mechanics*, **11**(4): A211–A218, 1944, https://doi.org/10.1115/1.4009394.

25. Marcinowski J., Static and stability analysis of shells with large displacements and finite rotations, *Engineering Transactions*, **48**(4): 373–393, 2000, https://doi.org/10.24423/engtrans.581.2000.

26. Matignon D., Stability properties for generalized fractional differential systems, *ESAIM: Proceedings*, **5**: 145–158, 1998, https://doi.org/10.1051/proc:1998004.

27. Mohammadi F.S., Rahimi Z., Sumelka W., Yang X.-J., Investigation of free vibration and buckling of Timoshenko nano-beam based on a general form of Eringen theory using conformable fractional derivative and Galerkin method, *Engineering Transactions*, **67**(3): 347–367, 2019, https://doi.org/10.24423/EngTrans.1001.20190426.

28. Needleman A., Material rate dependence and mesh sensitivity in localization problems, *Computer Methods in Applied Mechanics and Engineering*, **67**(1): 69–85, 1988, https://doi.org/10.1016/0045-7825(88)90069-2.

29. Needleman A., Tvergaard V., Analyses of plastic flow localization in metals, *Applied Mechanics Reviews*, **45**(3S): S3–S18, 1992, https://doi.org/10.1115/1.3121390.

30. Obrezkov L.P., Equilibrium and stability of nonlinearly elastic cylinder made of Blatz-Ko material, *Engineering Transactions*, **64**(4): 427–463, 2016, https://doi.org/10.24423/engtrans.736.2016.

31. Neilsen M.K., Schreyer H.L., Bifurcations in elastic-plastic materials, *International Journal of Solids and Structures*, **30**(4): 521–544, 1993, https://doi.org/10.1016/0020-7683(93)90185-A.

32. Petras I., Stability of fractional-order systems with rational orders: A survey, *Fractional Calculus and Applied Analysis*, **12**(3): 269–298, 2009.

33. Podlubny I., *Fractional Differential Equations*, Academic Press, San Diego, 1999.

34. Rabotnov Y.N., Equilibrium of an elastic medium with after-effect [in Russian], *Prikladnaya Matematika i Mekhanika (J. Appl. Math. Mech.)*, **12**(1): 53–62, 1948.

35. Radwan A.G., Soliman A.M., Elwakil A.S., Sedeek A., On the stability of linear systems with fractional-order elements, *Chaos, Solitons and Fractals*, **40**(5): 2317–2328, 2009, https://doi.org/10.1016/j.chaos.2007.10.033.

36. Rosen A., Bodner S.R., The influence of strain rate and strain ageing on the flow stress of commercially-pure aluminium, *Journal of the Mechanics and Physics of Solids*, **15**(1): 47–62, 1967, https://doi.org/10.1016/0022-5096(67)90005-1.

37. Rossikhin Y.A., Shitikova M.V., Comparative analysis of viscoelastic models involving fractional derivatives of different orders, *Fractional Calculus and Applied Analysis*, **10**(2): 111–121, 2007, http://hdl.handle.net/10525/1309.

38. Rossikhin Y.A., Shitikova M.V., Application of fractional calculus for dynamic problems of solid mechanics: novel trends and recent results, *Applied Mechanics Reviews*, **63**(1): 010801, 2010, https://doi.org/10.1115/1.4000563.

39. Rudnicki J.W., Rice J.R., Conditions for the localization of deformation in pressure-sensitive dilatant materials, *Journal of the Mechanics and Physics of Solids*, **23**(6): 371–394, 1976, https://doi.org/10.1016/0022-5096(75)90001-0.

40. Samko S.G., Kilbas A.A., Marichev O.I., *Fractional Integrals and Derivatives*, Gordon and Breach, Amsterdam, 1993.

41. Singh H., Kumar D., Singh J., Singh C.S., A reliable numerical algorithm for the fractional Klein-Gordon equation, *Engineering Transactions*, **67**(1): 21–34, 2019, https://doi.org/10.24423/EngTrans.910.20190214.

42. Sleeswyk A.W., Slow strain-hardening of ingot iron, *Acta Metallurgica*, **6**(9): 598–603, 1958, https://doi.org/10.1016/0001-6160(58)90101-9.

43. Sluys L.J., de Borst R., Wave propagation and localization in a rate-dependent cracked medium model – Formulation and one-dimensional examples, *International Journal of Solids Structure*, **29**(23): 2945–2958, 1992, https://doi.org/10.1016/0020-7683(92)90151-I.

44. Sumelka W., Fractional viscoplasticity, *Mechanics Research Communications*, **56**: 31–36, 2014, https://doi.org/10.1016/j.mechrescom.2013.11.005.

45. Sumelka W., Łuczak B., Gajewski T., Voyiadjis G.Z., Modelling of AAA in the framework of time-fractional damage hyperelasticity, *International Journal of Solids and Structures*, **206**: 30–42, 2020, https://doi.org/10.1016/j.ijsolstr.2020.08.015.

46. Tarasov V.E., *Fractional Dynamics. Applications of Fractional Calculus to Dynamics of Particles, Fields and Media*, Springer-Verlag, Berlin, Heidelberg, 2010, https://doi.org/10.1007/978-3-642-14003-7.

47. Troger H., Steindl A., *Nonlinear Stability and Bifurcation Theory. An Introduction for Scientists and Engineers*, Springer-Verlag, Wien, New York, 1990.

48. Zhou Y., Zhang Y., Noether symmetries for fractional generalized Birkhoffian systems in terms of classical and combined Caputo derivatives, *Acta Mechanica*, **231**(7): 3017–3029, 2020, https://doi.org/10.1007/s00707-020-02690-y.

Received December 23, 2024; revised June 16, 2025; accepted July 8, 2025; available online December 12, 2025; version of record February 25, 2026; published issue March 30, 2026.

Engineering Transactions, **74**(1): 105–120, 2026, https://doi.org/10.24423/engtrans.2025.3484
Institute of Fundamental Technological Research Polish Academy of Sciences (IPPT PAN)
Université de Lorraine • Poznan University of Technology

SiMRTRANS

Simulation of Vibro-Isolation Performance in Sensitive Cargo Transportation Platforms with Quasi-Zero-Stiffness Suspension under Impact Perturbations

Oleksiy Larin[1)*], Ksenia Potopalska[1)], Galina Timchenko[2)], Nikita Vasylchenko[1)]

[1)] *Department of Mathematical Modeling and Intelligent Computing in Engineering*
[2)] *Department of Applied Mathematics*
National Technical University "Kharkiv Polytechnic Institute"
Kharkiv, Ukraine

*Corresponding Author: oleksiy.larin@khpi.edu.ua

This work deals with the theoretical modeling of the vertical dynamics of a specialized vehicle featuring a dual suspension system. Vehicle ride quality is essential for ensuring the safety and comfort of passengers and the protection of sensitive or hazardous cargo. The study focuses on a two-axle vehicle model with a dual suspension system. The first-level comprises a traditional suspension with linear stiffness, while the second-level features nonlinear quasi-zero-stiffness (QZS) characteristics. The research employs a discrete nonlinear dynamic model that considers the vertical displacements and angular rotations of the vehicle masses. The nonlinear QZS response is modeled to optimize vibration isolation performance under varying load conditions, while damping effects are included via a Rayleigh dissipation function. The integral characteristics of the QZS element are also studied in detail using finite element (FE) computer simulations in a 3D setting. These simulations provide a comprehensive understanding of the mechanical response and stress-strain distribution within the QZS element, validating its performance under real-world conditions. The results demonstrate the influence of the nonlinear suspension characteristics on vibration isolation performance and load stability. The QZS-based suspension effectively reduces dynamic stresses, particularly under low-frequency excitations, while maintaining structural integrity and operational efficiency.

Keywords: vibro-isolation performance, nonlinear discrete model, kinematic excitations, quasi-zero stiffness, meta-structures.

1. Introduction

Vehicle ride quality constitutes a critical parameter for the secure and comfortable transportation of passengers and goods within automotive systems.

For specific cargo types – such as vibration-sensitive or hazardous materials – it is essential to attenuate dynamic loads to mitigate the risk of damage or safety incidents. These dynamic stresses, which impact cargo, are primarily induced by road surface irregularities that propagate forces through the vehicle's wheels and suspension architecture. Nonlinear suspension solutions, especially those designed with variable stiffness and damping properties [1, 2], are therefore essential in modern automotive engineering, providing an optimal balance between vibration isolation and operational efficiency under varying conditions. By reducing dynamic loads, these systems not only improve stability and comfort for passengers, but also protect sensitive or dangerous loads from potential damage. This approach is particularly important on uneven road surfaces, where the forces transmitted through the suspension could otherwise create excessive stress on both passengers and cargo.

In contemporary engineering practice, nonlinear suspension systems with adaptive stiffness or damping characteristics are extensively employed to suppress dynamic loads during transit. Among these, suspensions exhibiting quasi-zero stiffness (QZS) properties are particularly significant, as they provide effective vibration isolation while maintaining suspension effectiveness. Such systems perform optimally under certain operational conditions and are advantageous due to their compact configurations, which facilitate efficient spatial integration [3–6].

From an engineering point of view, QZS elements can be realized using different technical schemes. For example, a gas-interconnected QZS pneumatic suspension was presented in [7, 8], where an X-shaped structure was designed. Studies [9–11] examined various models of vibration isolators aimed at enhancing vibration isolation efficiency.

It was proposed in [12] to use an isolator consisting of n consecutive elements to study the mechanism of acquiring multiple QZS characteristics. Three types of equivalent mechanical models were studied to investigate the properties of the proposed isolator. It was found that, as the number of layers increased, the proposed isolator was effective in achieving low-frequency vibration isolation under different preloads, and this advantage could be further enhanced with small damping and excitation. A single-degree-of-freedom (DOF) system incorporating the proposed isolator was developed for theoretical and experimental study of its isolation characteristics in [12, 13]. A numerical method, based on the direct integration of the dynamic equation, verified the analytical results of the frequency response functions. Experiments were also carried out to verify the isolation performance of the nonlinear vibrator supported by the flexible plate.

Generally, it can be concluded that negative stiffness, which arises in unit cells through buckling or snap-through, is considered the fundamental principle

for energy absorption [5, 10–12, 14]. That is, by appropriately assembling unit cells with negative stiffness in series, metamaterials and/or metastructures can be developed with desired shock protection or energy absorption performance [10, 12]. Specially designed curved beams and inclined beams [5, 10–12, 14], placed within constrained supporting frames, can be easily fabricated using 3D printing technology.

Based on the different approaches described, one can find that recent advances in metastructures and additive technologies provide new technologically efficient and cost-effective tools to realize QZS elements and integrate them into the suspension system of modern specialized vehicles.

The current study considers the theoretical modeling of the dynamic behavior of a specialized vehicle with a dual suspension system. The first-level is a typical torsion bar suspension with linear stiffness, while the second-level has a nonlinear characteristic with QZS and serves as a third vibration isolation/damping element, in particular one with an internal elastic-damper support. The modeling is presented within the framework of numerical vibration analysis, based on a discrete nonlinear dynamic system. The dynamics of the system are analyzed under a kinematic impact load sequentially applied to the front and rear axles of the vehicle.

2. Discrete model of the specialized vehicle with nonlinear double-level suspension

A two-axle vehicle is considered, the model of which is shown in Fig. 1. It conditionally consists of three levels: the basic suspension, the platform, and the vibration isolation object. The vehicle base has a linear suspension, while the cargo platform is equipped with an additional suspension stage. This stage is connected to the first-level suspension through an additional second-level that exhibits a nonlinear elastic response with QZS (Fig. 1).

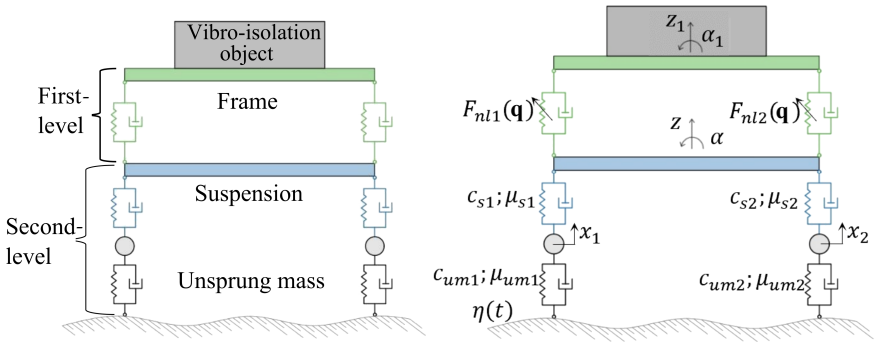

Fig. 1. General schematic of the proposed dynamic system with a double-level suspension.

Lagrange's second-order equations are used to develop a discrete nonlinear model according to the proposed vehicle design, technical scheme of which is shown in Fig. 1:

$$\frac{\mathrm{d}}{\mathrm{d}t}\left(\frac{\partial T}{\partial \dot{q}_i}\right)+\frac{\partial T}{\partial \dot{q}_i}+\frac{\partial \Pi}{\partial q_i}+\frac{\partial R}{\partial \dot{q}_i}=0, \qquad i=\overline{1,...,6}, \tag{2.1}$$

where t denotes time, T is the kinetic energy of the system, Π is the potential energy of the system, and R is the potential of the dissipative forces, q_i is the generalized coordinate, which consist of the vertical motions of the masses and the angles of the rotations (Eq. (2.2)). The dots above the variables indicate time derivatives:

$$\{\mathbf{q}\}=\{x_1,x_2,z,\alpha,z_1,\alpha_1\}^{\mathrm{T}}. \tag{2.2}$$

It is straightforward to obtain the kinetic energy:

$$T=\frac{1}{2}\sum_{i=1}^{6}m_i\dot{q}_i^2, \tag{2.3}$$

where m_1 is the total front axle mass, which consists of two wheels and the axle shaft, the same applies to the rare axle mass $m_2=m_1$. The mass m_3 designates the total suspension mass (with all installed units) of the first-level. The mass $m_4=m_{fr}+m_o$ is the total mass of the second-level of suspension, which includes the cargo frame (m_{fr}) and the mass of the vibration isolation object (m_o). The moments of inertia of the first-level frame as well as the second-level frame (generally a specific cargo platform) are denoted as $m_5=J_1$ and $m_6=J_2$, respectively.

The system potential energy consists of the potential energy of the linear elastic elements (the tires and the first-level suspension) and the potential energy of the nonlinear suspension system of the second-level:

$$\Pi=\Pi_l+\Pi_{nl}. \tag{2.4}$$

The linear part can be presented as follows:

$$\Pi_l=\frac{1}{2}\sum_{i=1}^{2}c_{umi}\left(x_i-\eta_i(t)\right)^2+\frac{1}{2}\sum_{i=1}^{2}c_{si}\left(z-x_{1i}\right)^2, \tag{2.5}$$

where the following designations are additionally used:

$$x_{11}=z-\frac{L}{2}\alpha, \qquad x_{12}=z+\frac{L}{2}\alpha. \tag{2.6}$$

The potential energy of the second-level suspension is defined as the integral of the nonlinear elastic response, i.e., $F_{nl}(y) = (\partial \Pi_{nl})/(\partial y)$. Considering that there are two nonlinear elements presented in the system (front and rear), the following equation for Π_{nl} can be written using the notations shown in Fig. 1:

$$\Pi_{nl}(z, z_1, \alpha, \alpha_1) = \Pi_{nl1}(y_1 = z_1 - x_{21}) + \Pi_{nl2}(y_2 = z_1 - x_{22}), \tag{2.7}$$

where

$$x_{21} = z_1 - z + \frac{L}{2}(\alpha - \alpha_1), \qquad x_{22} = z_1 - z + \frac{L}{2}(\alpha_1 - \alpha). \tag{2.8}$$

Considering the correspondence between local and global coordinates, the following formulations for the nonlinear forces can be proposed:

$$F_3 = \frac{\partial \Pi_{\mathrm{nl1}}}{\partial y_1}\frac{\partial y_1}{\partial z} + \frac{\partial \Pi_{\mathrm{nl2}}}{\partial y_2}\frac{\partial y_2}{\partial z} = -\left[F_{nl}(y = z_1) + F_{nl}(y = z_2)\right], \tag{2.9}$$

$$\widetilde{F}_3 = \frac{\partial \Pi_{nl1}}{\partial y_1}\frac{\partial y_1}{\partial \alpha} + \frac{\partial \Pi_{nl2}}{\partial y_2}\frac{\partial y_2}{\partial \alpha} = \frac{L}{2}\left[F_{nl}(y = z_1) - F_{nl}(y = z_2)\right], \tag{2.10}$$

$$F_4 = \frac{\partial \Pi_{\mathrm{nl1}}}{\partial y_1}\frac{\partial y_1}{\partial z_1} + \frac{\partial \Pi_{\mathrm{nl2}}}{\partial y_2}\frac{\partial y_2}{\partial z_1} = F_{nl}(y = z_1) + F_{nl}(y = z_2), \tag{2.11}$$

$$\widetilde{F}_4 = \frac{\partial \Pi_{nl1}}{\partial y_1}\frac{\partial y_1}{\partial \alpha_1} + \frac{\partial \Pi_{nl2}}{\partial y_2}\frac{\partial y_2}{\partial \alpha_1} = \frac{L}{2}\left[-F_{nl}(y = z_1) + F_{nl}(y = z_2)\right]. \tag{2.12}$$

The dissipative forces in the current study are proposed to be considered within a Rayleigh linear model, in which the damping matrix is proportional to the linear stiffness matrix. Therefore, the damping potential is a quadratic form of the generalized coordinate velocities.

Substituting Eq. (2.3) and Eq. (2.4), and considering Eq. (2.5) to Eq. (2.12), into the Lagrange Eq. (2.13), one can obtain the main system of equations:

$$\begin{cases} m_1\ddot{x}_1 + \dfrac{\partial R}{\partial \dot{x}_1} + F_{el1} = c_t\eta_1(t), \\ m_2\ddot{x}_2 + \dfrac{\partial R}{\partial \dot{x}_2} + F_{el2} = c_t\eta_2(t), \\ m_3\ddot{z} + \dfrac{\partial R}{\partial \dot{z}} + F_{el3} + F_3(z, z_1, \alpha, \alpha_1) = 0, \\ J_1\ddot{\alpha} + \dfrac{\partial R}{\partial \dot{\alpha}} + F_{el4} + \widetilde{F}_3(z, z_1, \alpha, \alpha_1) = 0, \\ m_4\ddot{z}_1 + \dfrac{\partial R}{\partial \dot{z}_1} + F_4(z, z_1, \alpha, \alpha_1) = 0, \\ J_2\ddot{\alpha}_1 + \dfrac{\partial R}{\partial \dot{\alpha}_1} + \widetilde{F}_4(z, z_1, \alpha, \alpha_1) = 0. \end{cases} \tag{2.13}$$

Thus, we have a system of differential equations describing the dynamics of a vehicle with a double-level nonlinear suspension, where the second-level is additional and exhibits nonlinear characteristic. In system (2.13), to simplify the presented form of the equations, a vector of elastic forces ($\mathbf{F}_{el}$) is introduced:

$$\{\mathbf{F}_{el}\} = [\mathbf{K}]\,\{\mathbf{q}\}\,, \tag{2.14}$$

$$[\mathbf{K}] = \begin{bmatrix} (c_{um1}+c_{s1}) & 0 & -c_{s1} & \frac{L}{2}c_{s1} & 0 & 0 \\ & (c_{um2}+c_{s2}) & -c_{s2} & -\frac{L}{2}c_{sa} & 0 & 0 \\ & & c_{ss} & -\frac{L}{2}c_{sn} & 0 & 0 \\ & & & L^2\frac{c_{ss}}{4} & 0 & 0 \\ & \text{symmetric part} & & & 4c_{fr} & 0 \\ & & & & & L^2c_{fr} \end{bmatrix}, \tag{2.15}$$

where, for simplification, we introduced additional parameters for the total stiffness of the first-level of suspension and for the difference between the front and rear axle stiffness of the first-level suspension:

$$c_{ss} = c_{sn1} + c_{sn2}, \qquad c_{sn} = c_{sn2} - c_{sn1}. \tag{2.16}$$

In the stiffness matrix, an additional parameter c_{fr} is introduced. It is artificially added as a linearized (through bisection approximation) stiffness of the second-level suspension. The derived elastic forces $\mathbf{F}_{el5}$ and $\mathbf{F}_{el6}$ are not used directly in Eq. (2.13); however, the stiffness matrix in its full size is used for the introduction of damping and for some calculations of natural frequencies and normal modes, which are used for model testing and basic preliminary dynamic analysis.

Additionally, the system of (2.13) includes some dissipative forces, which reflect the presence of viscosity in tire deformation and damping in the first-level suspension. These forces are derived from the corresponding potential of dissipative forces (2.9) and have the following analytical expressions, given in matrix form as follows:

$$\left\{\frac{\partial R}{\partial \dot{q}}\right\} = \mu\,[\mathbf{K}]\,\{\dot{q}\}. \tag{2.17}$$

The system (2.13) allows the analysis of vertical and angular vibrations of the vehicle occurring under the kinematic excitations $\eta_1(t)$ and $\eta_2(t)$, which are

applied to the wheels of the vehicle due to interaction with road surface roughness. Here, it must be underlined that a time delay must be taken into account and then the kinematic load is applied:

$$\eta_1(t) = \eta(t), \qquad \eta_2(t) = \eta\left(t + \frac{L}{v}\right), \tag{2.18}$$

where L is the distance between the wheel axles and v is the vehicle riding speed.

A simple perturbation is introducing here as a half-sinusoidal function of time:

$$\eta(t) = \begin{cases} a_0 \sin \dfrac{\pi\,(t - t_0)}{t_n - t_0}, & t \in [t_0, t_n]\,, \\ 0, & t \notin [t_0, t_n], \end{cases} \tag{2.19}$$

where a_0 is the amplitude (height) of the geometric perturbation, and t_0, t_n are, respectively, the initial and final times during which the perturbation is active. The value of t_n is calculated from the geometric size (width) of the perturbation and the vehicle riding speed.

Presented system of (2.13) is identified with the nonlinear elastic forces $F_{nl}(y)$. In the current work, we propose to use a specific element that has a QZS of its elastic response. In this study, we numerically identified such a response of the QZS element and approximated the resulting dependencies using cubic splines. Some details for this element modeling are presented further.

3. Integral nonlinear elastic response of the QZS element

Following the idea of repetitive elementary cells in metamaterials proposed in [10], in the current study, we use QZS elements, which are formed by a sinusoidal beam, a pair of semicircular arches, and stiffer wall elements.

The 3D model was build in parametric form, allowing us to determine rational geometrical parameters of the QZS element that has a QZS response region within a required range of possible displacements. Our model also ensures a practically required level of response forces, which enable the use of such an element in real applications. Finite element (FE) modeling is used for direct computer simulations, which allow us to obtain the integral elastic response of the QZS element under kinematic (displacement-controlled) loading. Figure 2 presents the geometry and FE mesh.

The final model parameters allow us to obtain the nonlinear characteristic of the QZS element, which yields an almost zero reaction to displacement perturbations in a region of 30 mm. The corresponding results of computer simulations are presented in Fig. 3.

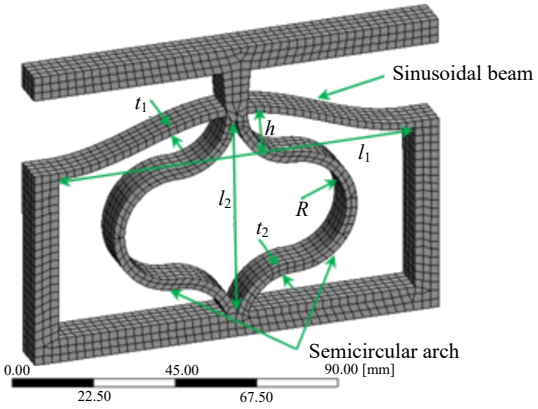

Fig. 2. QZS element FE model and geometry.

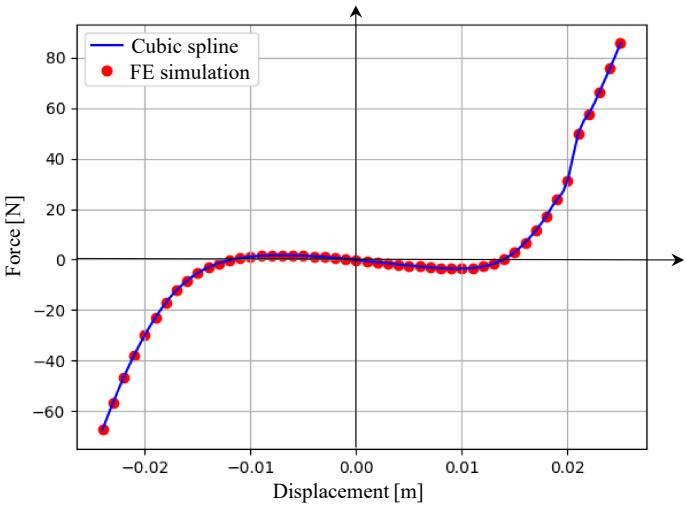

Fig. 3. Integral nonlinear elastic response of QZS element.

The main geometric parameters of the QZS element, determined from a set of FE simulations and used as the basic model in the current study, are as follows: $l_1 = 208\,\text{mm}$ (width), $l_2 = 120\,\text{mm}$ (hight), $l_3 = 14\,\text{mm}$ (thickness), $t_1 = 8.1\,\text{mm}$ (beam thickness), $t_2 = 12.4\,\text{mm}$ (arc thickness), $h = 31.5\,\text{mm}$, and $R = 30\,\text{mm}$.

It should be noted that if the potential displacements exceed the specified values, the stiffness of this system will lead to the opposite effect in terms of vibration isolation. This unit element demonstrates satisfactory results and can serve as a basis for modeling a more complex vibration isolator that can operate at higher displacement levels. Figure 3 shows these results, which are centered around zero when considering the mean static load.

FE simulations also allow us to determine and evaluate additional strength parameters of the QZS element. This is important from a practical perspective to

ensure reliability. Figure 4 demonstrates the distributions of displacements (deformation filed) and von Mises stresses at different levels of displacement-controlled loading with an amplitude of ±9 mm.

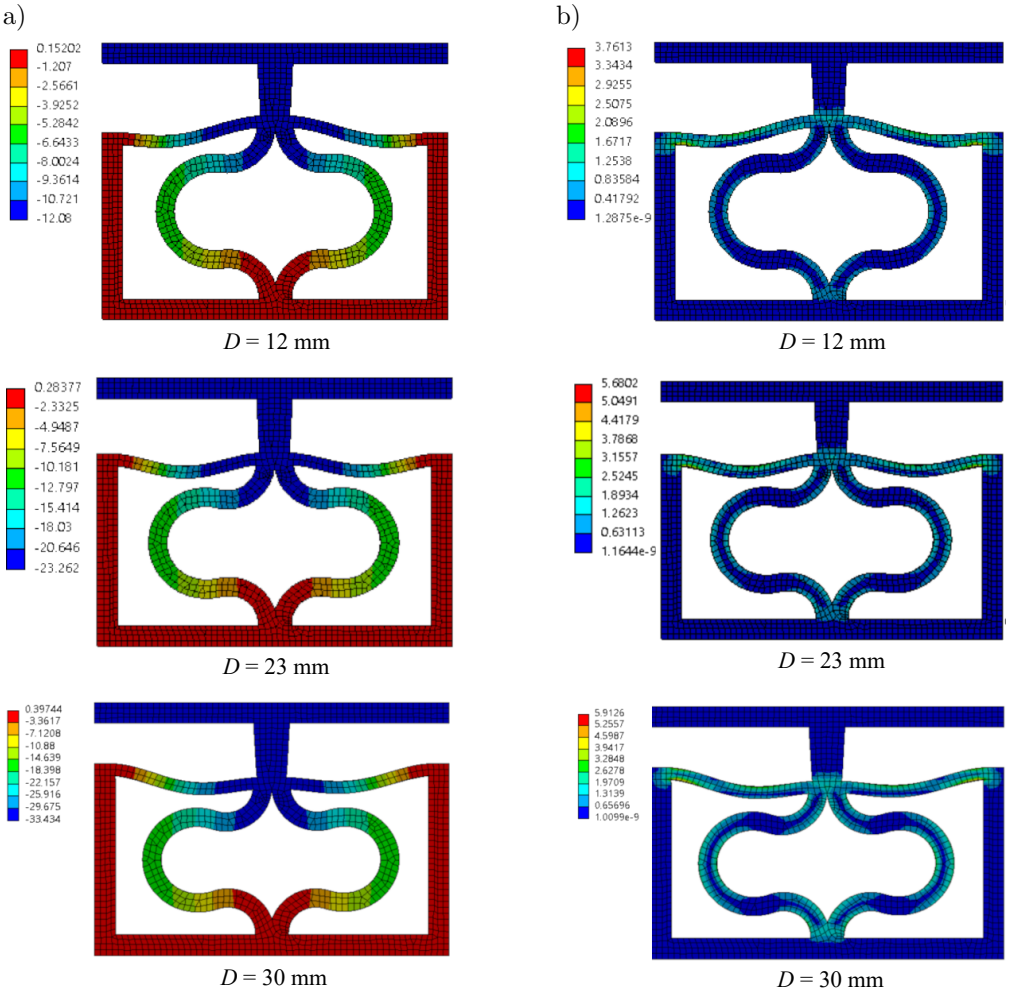

Fig. 4. a) Vertical displacements [mm], b) equivalent von Mises stresses [MPa] under different displacement-controlled load levels load.

4. Results of the numerical simulations of vibro-isolation performance for sensitive cargo transportation

Mathematical model presented in Sec. 2, with nonlinear elastic responses F_{nl} of QZS elements identified from direct FE simulations, is used for numerical computations of the dynamics of such a system. The differential Eq. (2.13) are solved numerically using an explicit integration scheme. The mechanical and

geometrical parameters used in the numerical experiments are summarized in Table 1.

Table 1. Mechanical parameters of the system.

Parameter	L	m_1, m_2	m_3	m_4	I_1	I_2	c_{sn1}, c_{sn2}	c_{um}
Units	m	kg	kg	kg	kg m^2	kg m^2	kN/m	kN/m
Value	2.2	83	168	176	252.3	344.6	240	350

As a results of the integration, we obtained the dynamics of all generalized coordinates, including displacements, velocities, and accelerations. Figure 5 and Fig. 6 present examples of the computed time histories for vertical vibrations of the front and rear axes, as well as vertical vibrations of the center of mass at

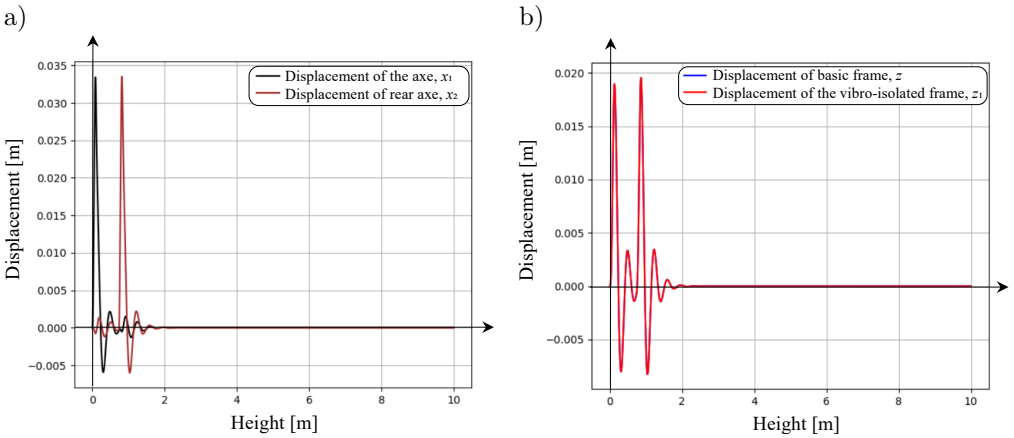

Fig. 5. Vertical vibrations of the generalized coordinates of the vehicle without the second-level of nonlinear suspension (model L).

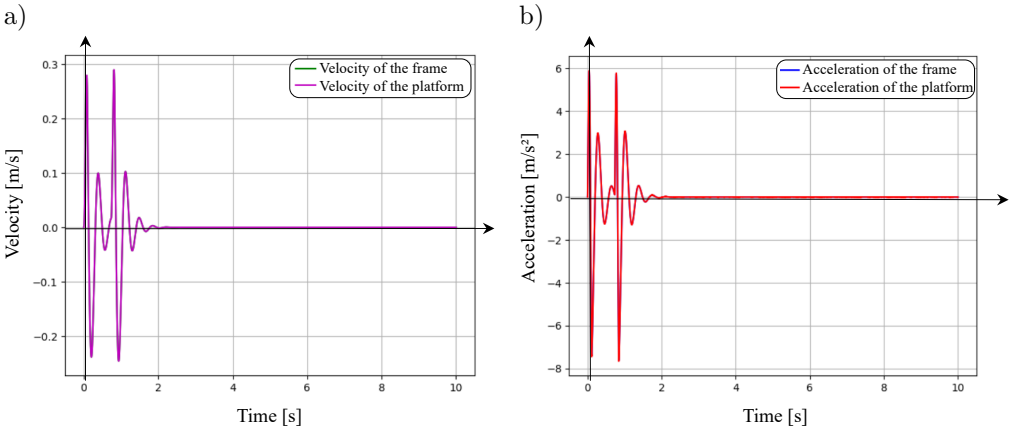

Fig. 6. Vertical velocity and acceleration of the cargo object's center of mass.

the first- and second-level suspension, i.e., z and z_1. In this example, the road roughness has a height of 50 mm and a width of 300 mm (standard road).

These results are presented for the case where second-level suspension is excluded from the model. Technically, this is realized by substituting the nonlinear forces with linear ones of extremely high stiffness (10^8 N/m), which corresponds to a rigid metal rod connection between the suspension levels. This approach allows us to maintain the same mass-inertial properties in both models: the basic linear model (model L) and the double-level nonlinear model (model NL).

Figure 6 shows the time dependencies of vibro-velocities and vibro-accelerations in the centre of mass of the cargo object (the object subject to potential vibro-isolations) for model L.

The same results were obtained for the proposed system with a second-level suspension integrating nonlinear QZS elements (model NL). Figure 7 and Fig. 8

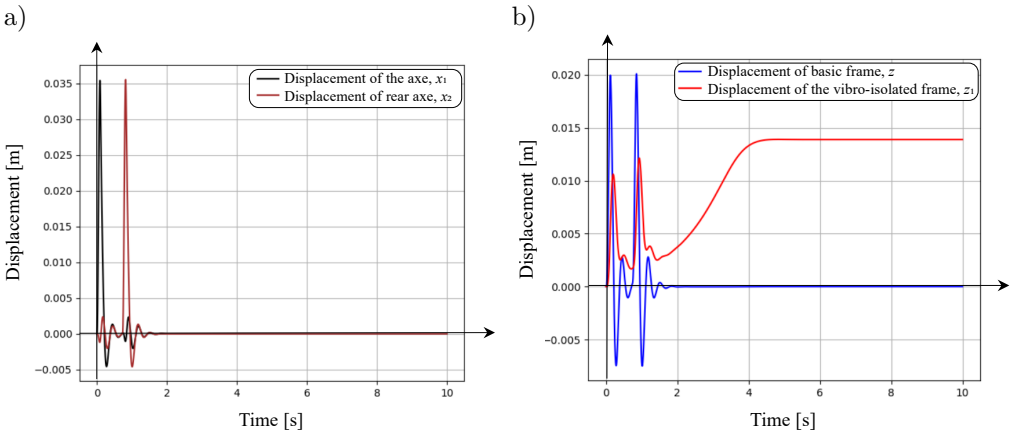

Fig. 7. Vertical vibrations of the generalized coordinates of the vehicle with the second-level of nonlinear suspension (model NL).

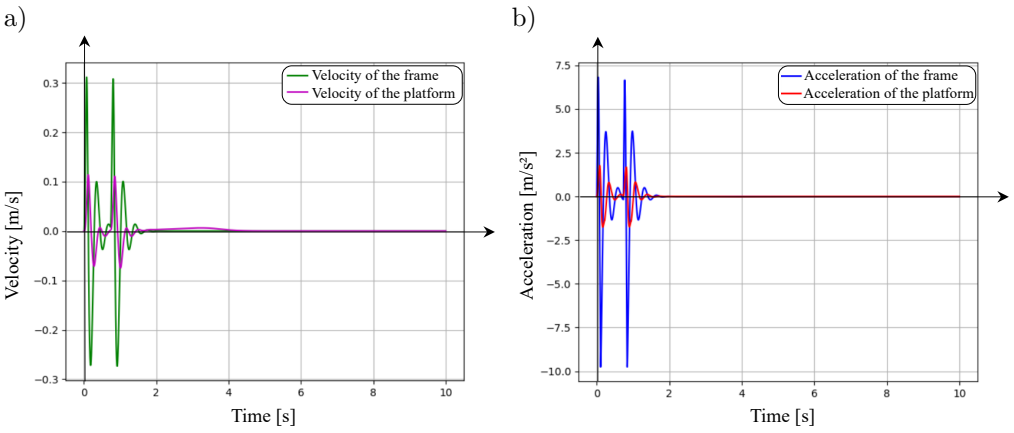

Fig. 8. Vertical vibrations of the generalized coordinates of the vehicle with the second-level of nonlinear suspension (model NL).

show the results for this case. Vertical vibrations of the front and rear axes have similar behavior and amplitudes levels as well as vertical dynamics of the center of mass as in the first-level suspension. However, the center of mass of the second-level simulation, which actually corresponds to the cargo object (the object being vibro-isolated) shows a significant reduction in vibration amplitudes at the moments of impact. An interesting phenomena is also observed: the displacement (position) of the cargo object's center of mass exhibits a smooth shifting over time following the impacts. This post-impact behavior is likely caused by inertia effects and shows a negative phenomena of some energy accumulation in the QZS elements.

Analysis of the vibro-velocity and vibro-acceleration levels shows a triple reduction in the amplitude levels, which confirms the crucial effectiveness of integrating QZS elements into the second-level suspension.

In the current study, a series of comparative computations was carried out to analyze vertical vibrations (displacements, velocities, and accelerations) under varying levels and shapes of kinematic impacts. We have varied the amplitude of the impact (height of the road roughness) in the range from 10 mm to 100 mm but with a fixed time of the impact (corresponding to a road roughness width of 300 mm). The results of these calculations are shown in Fig. 9. The proposed system of vibro-isolations shows a good efficiency in reducing vertical vibrations for impacts with amplitudes up to 70 mm, achieving a maximum reduction of nearly 100 %. In Fig. 9, phase trajectories of the vertical vibrations are also plotted for additional insight.

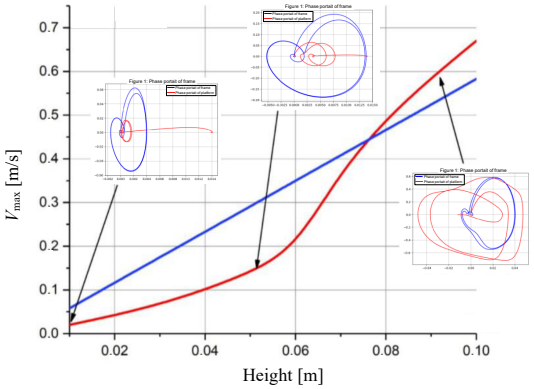

Fig. 9. Vertical vibrations of the center of mass of the vibro-isolated object (model L – blue line, model NL – red line).

Additionally, we examined the influence of the impact width on vibro-isolation performance. The results presented in Fig. 10 and Fig. 11 show that, as the road roughness width increases, the amplitudes of vibro-velocities and vibro-

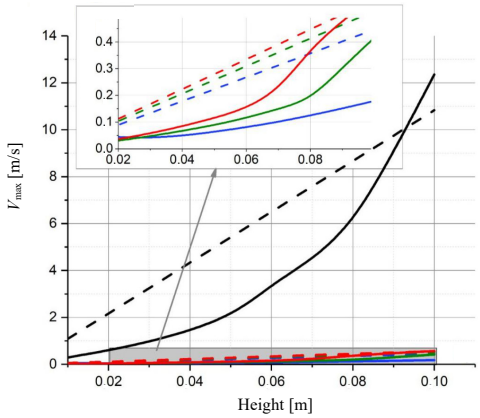

FIG. 10. Vertical vibro-velocities of the center of mass of the vibro-isolated object as a function of kinematic impact width (model L – dashed line, model NL – solid line).

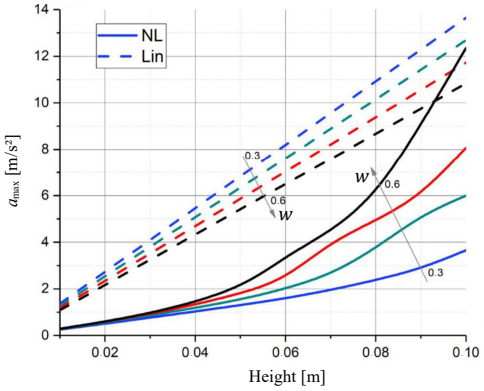

FIG. 11. Vertical accelerations of the center of mass of the vibro-isolated object as a function of kinematic impact width (model L – dashed line, model NL – solid line).

accelerations rise in the nonlinear model, whereas they increase only slightly and almost linearly in the linear model. Despite this, the nonlinear model consistently demonstrates good efficiency up to 90 mm for the road roughness height. For instance, at a 60 mm impact height and a 0.6 m width, we observed a two-fold reduction in vibro-accelerations.

5. Conclusion

The presented study highlights advancements in suspension systems for specialized vehicles, emphasizing the integration of nonlinear and QZS elements to enhance ride quality and vibration isolation. By combining linear and nonlinear suspension levels, the proposed dual-suspension system effectively minimized dynamic loads, protecting both passengers and cargo. Leveraging modern meta-

structural designs and additive manufacturing, the system achieved compact and cost-efficient configurations suitable for various operational conditions.

Numerical simulations demonstrated the significant effectiveness of the QZS-integrated suspension system. We observed a threefold reduction in vibro-velocity and vibro-acceleration amplitudes when comparing the QZS model to the basic linear model. The system effectively reduced vertical vibration amplitudes for kinematic impacts up to 70 mm in height.

An intriguing phenomenon was also observed: after impacts, the displacement (position) of the cargo object's center of mass exhibited a smooth, prolonged shift over time. This post-impact behavior, likely due to inertial effects, suggests negative phenomenon of a potential energy accumulation in the QZS elements. For improved system behavior in operational scenarios, an automatic positioning system and specific control strategy may need to be developed.

Fundings

This scientific study was supported and partially funded by National Research Foundation of Ukraine (NRFU grant no. 2023.03/0255).

Conflict of interest

The authors declare that they have no known competing financial interests or personal relationships that could have appeared to influence the work reported in this paper.

Authors' contributions

Oleksiy Larin formulated the general research problem, coordinated the overall study design, developed the Python-based computational tools used for post-processing and analysis, and interpreted the obtained results. He also prepared the final conclusions of the study. Galina Timchenko developed the mathematical model of the vehicle system, derived the governing differential equations, and performed the numerical simulations of the dynamic response. She also contributed to data processing, visualization of simulation results, and their analytical interpretation. Ksenia Potopalska designed the quasi-zero-stiffness (QZS) meta-structure concept and carried out the analysis of the integral nonlinear elastic characteristics of the QZS element. She was responsible for incorporating these characteristics into the mathematical model of the vibro-isolation system. Nikita Vasylchenko developed and verified the three-dimensional finite element model of the QZS meta-structure and conducted the finite element simulations used to evaluate deformation behavior, stress–strain states, and mechanical response of the QZS element. All authors reviewed and approved the final manuscript.

Data availability statement

Some or all of the data, models, or code that support the findings of this study are available from the corresponding author upon request.

References

1. Jin Y., Hou S., Yang T., Cascaded essential nonlinearities for enhanced vibration suppression and energy harvesting, *Nonlinear Dynamics*, **103**(2): 1427–1438, 2021, https://doi.org/10.1007/s11071-020-06165-6.
2. Fidrovska N., Slepuzhnikov E., Larin O., Varchenko I., Lipovyi V., Afanasenko K., Harbuz S., Increase of operating reliability of the travel wheel using the use of the elastic inserts EUREKA, *Physics and Engineering*, **2020**(5): 69–79, 2020, https://doi.org/10.21303/2461-4262.2020.001387.
3. Wang K., Zhou J., Chang Y., Ouyang H., Xu D., Yang Y., A nonlinear ultra-low-frequency vibration isolator with dual quasi-zero-stiffness mechanism, *Nonlinear Dynamics*, **101**(2): 755–773, 2020, https://doi.org/10.1007/s11071-020-05806-0.
4. Yan B., Yu N., Ma H., Wu C., A theory for bistable vibration isolators, *Mechanical Systems and Signal Processing*, **167**(Part A): 108507, 2022, https://doi.org/10.1016/j.ymssp.2021.108507.
5. Yan B., Wang Z., Ma H., Bao H., Wang K., Wu C., A novel lever-type vibration isolator with eddy current damping, *Journal of Sound and Vibration*, **494**: 115862, 2021, https://doi.org/10.1016/j.jsv.2020.115862.
6. Bian J., Jing X., Analysis and design of a novel and compact X-structured vibration isolation mount (X-mount) with wider quasi-zero-stiffness range, *Nonlinear Dynamics*, **101**(4): 2195–2222, 2020, https://doi.org/10.1007/s11071-020-05878-y.
7. Jiang X., Xu X., Shi T., Atindana V.A., Nonlinear characteristic analysis of gas-interconnected quasi-zero stiffness pneumatic suspension system: A theoretical and experimental study, *Chinese Journal of Mechanical Engineering*, **37**(1): 58, 2024, https://doi.org/10.1186/s10033-024-01039-z.
8. Pu H., Yuan S., Peng Y., Meng K., Zhao J., Xie R., Huang Y., Sun Y., Yang Y., Xie S., Luo J., Chen X., Multi-layer electromagnetic spring with tunable negative stiffness for semi-active vibration isolation, *Mechanical Systems and Signal Processing*, **121**: 942–960, 2019, https://doi.org/10.1016/j.ymssp.2018.12.028.
9. Lu Z.-Q., Gu D.-H., Ding H., Lacarbonara W., Chen L.-Q., Nonlinear vibration isolation via a circular ring, *Mechanical Systems and Signal Processing*, **136**: 106490, 2020, https://doi.org/10.1016/j.ymssp.2019.106490.
10. Fan H., Yang L., Tian Y., Wang Z., Design of metastructures with quasi-zero dynamic stiffness for vibration isolation, *Composite Structures*, **243**: 112244, 2020, https://doi.org/10.1016/j.compstruct.2020.112244.
11. Gholikord M., Etemadi E., Imani M., Hosseinabadi M., Hu H., Design and analysis of novel negative stiffness structures with significant energy absorption, *Thin-Walled Structures*, **181**: 110137, 2022, https://doi.org/10.1016/j.tws.2022.110137.
12. Dalela S., Balaji P.S., Leblouba M., Trivedi S., Kalam A., Nonlinear static and dynamic response of a metastructure exhibiting quasi-zero-stiffness characteristics for

vibration control: An experimental validation, *Scientific Reports*, **14**(1): 19195, 2024, https://doi.org/10.1038/s41598-024-70126-x.

13. Hao R.-B., Lu Z.-Q., Ding H., Chen L.-Q., A nonlinear vibration isolator supported on a flexible plate: analysis and experiment, *Nonlinear Dynamics*, **108**(2): 941–958, 2022, https://link.springer.com/article/10.1007/s11071-022-07243-7.

14. Debeau D.A., Seepersad C.C., Haberman M.R., Impact behavior of negative stiffness honeycomb materials, *Journal of Materials Research*, **33**: 290–299, 2018, https://doi.org/10.1557/jmr.2018.7.

Received December 13, 2024; revised June 1, 2025; accepted July 14, 2025; available online December 16, 2025; version of record March 13, 2026; published issue March 30, 2026.

Contents